

# Fabrication and characterization of Ge thin films and Ge-rich SiGe alloys for photovoltaic applications

**Author:**

Tsao, Chao-Yang

**Publication Date:**

2011

**DOI:**

<https://doi.org/10.26190/unsworks/4028>

**License:**

<https://creativecommons.org/licenses/by-nc-nd/3.0/au/>

Link to license to see what you are allowed to do with this resource.

Downloaded from <http://hdl.handle.net/1959.4/51218> in <https://unsworks.unsw.edu.au> on 2024-05-02

**FABRICATION AND CHARACTERIZATION OF  
GE THIN FILMS AND GE-RICH SiGe ALLOYS  
FOR PHOTOVOLTAIC APPLICATIONS**

**Chao-Yang Tsao**



**Centre for Photovoltaic Engineering**

**A thesis submitted to the University of New South Wales  
in fulfillment of the requirements for the degree of  
Doctor of Philosophy**

**March 2011**



PLEASE TYPE

THE UNIVERSITY OF NEW SOUTH WALES  
Thesis/Dissertation Sheet

Surname or Family name: **Tsao**

First name: **Chao-Yang**

Other name/s:

Abbreviation for degree as given in the University calendar: **PhD**

School: **Photovoltaic and Renewable Energy Engineering** Faculty: **Engineering**

Title: **Fabrication and Characterization of Ge Thin Films and Ge-rich SiGe Alloys for Photovoltaic Applications**

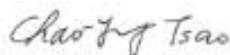
Abstract 350 words maximum: (PLEASE TYPE)

Germanium (Ge) thin films and Ge-rich silicon-germanium (SiGe) alloys have potential for lowering the manufacturing cost of photovoltaic (PV) devices especially in tandem solar cells. This thesis focuses on the fabrication and characterization of Ge thin films and Ge-rich SiGe alloys prepared by radio-frequency (RF) magnetron sputtering, an inexpensive, non-ultra high vacuum deposition technique capable of fabricating large area films. The motivation is given firstly, followed by a brief review of Ge in PV applications. Secondly, fabricating polycrystalline Ge (poly-Ge) thin films on glass by RF magnetron sputtering is investigated. In addition, *in situ* hydrogenation is applied in an attempt to further improve the properties of the Ge films. The influence of hydrogen on the deposition rate, surface morphology, and structural, optical, as well as electrical properties of poly-Ge films is explored. Moreover, to demonstrate the potential of the *in situ* hydrogenated poly-Ge (poly-Ge:H) films in PV applications, the doping of poly-Ge:H thin-films on glass is studied. P type films were deposited and *in situ* doped by co-sputtering Ge:H with boron (B) at various power levels in a mixture of argon and hydrogen at 500°C followed by a rapid thermal anneal (RTA) process. On the other hand, n type films were deposited and *ex situ* doped by firstly sputter-depositing a Ge:H layer and then a SiO<sub>2</sub>/P<sub>2</sub>O<sub>5</sub>+SiO<sub>2</sub>/SiO<sub>2</sub> sandwich structure capped with a SiN<sub>x</sub> layer, and finally followed by a thermal drive-in process with RTA. The evidence for successfully p-type and n-type doping of poly-Ge:H films is presented. Furthermore, the research scope is extended into polycrystalline Ge-rich SiGe alloys to explore the properties of the Ge alloyed with small amounts of Si by RF sputtering. Finally, a novel method for growing thin relaxed single crystalline Ge heteroepitaxial layers on Si substrates by using RF sputtering was developed. By using this method, the need of ultra-high-vacuum condition and the use of costly and extremely toxic germane gas are avoided. Therefore, thin relaxed single crystalline Ge epitaxial layers on Si substrate can be obtained at low cost, making the resultant Ge layer a potential virtual substrate for III-V material growth for tandem cell applications.

Declaration relating to disposition of project thesis/dissertation

I hereby grant to the University of New South Wales or its agents the right to archive and to make available my thesis or dissertation in whole or in part in the University libraries in all forms of media, now or here after known, subject to the provisions of the Copyright Act 1968. I retain all property rights, such as patent rights. I also retain the right to use in future works (such as articles or books) all or part of this thesis or dissertation.

I also authorise University Microfilms to use the 350 word abstract of my thesis in Dissertation Abstracts International (this is applicable to doctoral theses only).



31 /03 /2011

.....  
Signature

.....  
Witness

.....  
Date

The University recognises that there may be exceptional circumstances requiring restrictions on copying or conditions on use. Requests for restriction for a period of up to 2 years must be made in writing. Requests for a longer period of restriction may be considered in exceptional circumstances and require the approval of the Dean of Graduate Research.

FOR OFFICE USE ONLY

Date of completion of requirements for Award:

**COPYRIGHT STATEMENT**

'I hereby grant the University of New South Wales or its agents the right to archive and to make available my thesis or dissertation in whole or part in the University libraries in all forms of media, now or here after known, subject to the provisions of the Copyright Act 1968. I retain all proprietary rights, such as patent rights. I also retain the right to use in future works (such as articles or books) all or part of this thesis or dissertation.

I also authorise University Microfilms to use the 350 word abstract of my thesis in Dissertation Abstract International (this is applicable to doctoral theses only).

I have either used no substantial portions of copyright material in my thesis or I have obtained permission to use copyright material; where permission has not been granted I have applied/will apply for a partial restriction of the digital copy of my thesis or dissertation.'

Signed ..... *Chao Tsao* .....

Date ..... 30 /07 /2011 .....

**AUTHENTICITY STATEMENT**

'I certify that the Library deposit digital copy is a direct equivalent of the final officially approved version of my thesis. No emendation of content has occurred and if there are any minor variations in formatting, they are the result of the conversion to digital format.'

Signed ..... *Chao Tsao* .....

Date ..... 30 /07 /2011 .....

ORIGINALITY STATEMENT

'I hereby declare that this submission is my own work and to the best of my knowledge it contains no materials previously published or written by another person, or substantial proportions of material which have been accepted for the award of any other degree or diploma at UNSW or any other educational institution, except where due acknowledgement is made in the thesis. Any contribution made to the research by others, with whom I have worked at UNSW or elsewhere, is explicitly acknowledged in the thesis. I also declare that the intellectual content of this thesis is the product of my own work, except to the extent that assistance from others in the project's design and conception or in style, presentation and linguistic expression is acknowledged.'

Signed ..... 

Date ..... 31 /03 /2011



# DEDICATION

*To*

*My Father Wan-Shun Tsao*

*and*

*My Mother Li-Chi Tsai*

*“Few things are impossible in themselves; and it is often for want of will, rather than of means, that man fails to succeed.”*

La Rocheforcauld

---

---

## ABSTRACT

---

Ge thin films and Ge-rich SiGe alloys have potential for lowering the manufacturing cost of PV devices especially in tandem solar cells. This thesis focuses on the fabrication and characterization of Ge thin films and Ge-rich SiGe alloys prepared by RF magnetron sputtering, an inexpensive, non-ultra high vacuum deposition technique capable of fabricating large area films. The motivation is given firstly, followed by a brief review of Ge in PV applications, a brief survey of fabrication techniques for Ge thin films and an introductory discussion of the role of deposition temperature during thin film growth by PVD.

Secondly, the fabrication of polycrystalline Ge (poly-Ge) thin films on glass by RF magnetron sputtering is investigated. The crystallinity of sputter-deposited Ge thin films on glass prepared by *in situ* growth and *ex situ* solid-phase crystallization (SPC) is comparatively investigated to determine a suitable approach for growing high quality films. The influence of *in situ* deposition substrate temperature and SPC temperature ( $T_{spc}$ ) on the structural evolution of the Ge films is demonstrated. Optical properties of the *in situ* grown films are subsequently examined as it is found that poly-Ge films *in situ* crystallized at 450°C exhibit significantly better crystal qualities than those formed by SPC at 600°C.

In an attempt to further improve the properties of the Ge films, *in situ* hydrogenated Ge (Ge:H) thin films are deposited on silicon nitride ( $\text{SiN}_x$ ) coated glass at low  $T_s$  and are

characterized. The structural, optical, and electrical properties of the Ge:H films are investigated. Moreover, to demonstrate the potential of the *in situ* hydrogenated poly-Ge (poly-Ge:H) films in PV applications, the doping of poly-Ge:H thin-films on glass is studied. *In situ* p-type and *ex situ* n-type doping techniques for poly-Ge:H films sputter-deposited on glass are developed. The evidence for controlled p-type and n-type doping of poly-Ge:H films sputter-deposited on glass is presented.

The research scope is subsequently extended into polycrystalline Ge-rich SiGe alloy material to explore the properties of the Ge alloyed with small amounts of Si by RF sputtering. The *in situ* hydrogenation is employed to improve the structural and electrical properties of the films. Films with a thickness of ~300 nm are as deposited at 500°C. The influence of varying Si fraction on the structural evolution, band gap shift and resistivity variation of the films is presented. The correlation between the roughness, structural, optical and electrical properties is explored and discussed.

Finally, the development of a novel method for growing thin relaxed single crystalline Ge hetero-epitaxial layers on Si substrates by using RF magnetron sputtering is described. By using this method, the need for ultra-high-vacuum condition and the use of costly and extremely toxic germane gas (the precursor of Ge) are avoided. In this way, thin relaxed single crystalline Ge epitaxial layers on Si substrate can be obtained at low cost, making the resultant Ge layer a potential virtual substrate for III-V material growth for tandem cell applications.

---

---

## ACKNOWLEDGEMENTS

---

First and foremost, I would like to thank my supervisor, **Prof. Martin A. Green**, for accepting me as his student. It was truly a wonderful honour and great pleasure to be supervised by him and to interact with him. His guidance and direction helped me immensely. Without his supervision, this work would not have been possible. I would also like to thank my co-supervisors **Dr. Dengyuan Song**, **Dr. Jeana Xiaojing Hao**, and **Dr. Patrick Campbell**. **Dengyuan** kindly passed on his scientific skills and expertise to me, particularly the skills for preparing and submitting papers. **Jeana** subsequently co-supervised me after **Song's** return to China and offered valuable suggestions and discussion for my experiments, especially for the boron doping of Ge films. **Patrick** offered me help with the RF magnetron sputtering system, ensuring the smooth progress of my experimental work of various depositions. Special thanks belong to **Jürgen Weber**, who played an important role, like an unofficial co-supervisor, in my thesis. **Jürgen** kindly assisted me to design my first series of sputter-deposition when I was a beginner in using a sputtering system. He was so enthusiastic to offer fruitful discussion and suggestions all the way in my work.

Next, I would like to thank all the people who made contributions to my work during my time at UNSW. I would like to thank my former supervisor **Prof. Armin Aberle** for his guidance at the initial stage of my study. I also thank **A/Prof. Gavin Conibeer** for his support. In addition, I thank **Dr. Daniel Inns**, **Dr. Ivan Perez-Wurfl**, **Dr Shujuan Huang**, and **Dr. Per Widenborg** for their help as well as **Dr. Tom Puzzer**, **Dr. Oliver Kunz**, **Michael Wolf**, and **Mark Griffin** for devoting time and effort to helping me with various technical issues met in sputtering deposition and other equipment. I am grateful to **Yidan Haung** for taking nice TEM images presented in Chapter 2 and 6. I am also grateful to my fellow students **Johnson Wong** for Hall measurements, **Jialiang Huang** for Hall measurements and TEM measurements, **Yuguo Tao** for SEM measurements, **Zi Ouyang** for preparing cut SiN<sub>x</sub> coated glass panes, **Ziv Hameiri** and **Stanley Wang** for spin-on-dopant trainings, **Bai Xue** and **Doris Pei Husan Lu** for n<sup>+</sup> diffusing n-type Si wafers, **Doris** also for laser-scribing Ge/Si samples, **Lei Shi** for metallization and I-V

curve measurements. Thanks also go to **Yong Heng So, Adeline Sugianto, Dawei Di, Hongtao Cui, Bo Zhang, Pasquale Aliberti, Andy Hsieh, Zhenyu Wan, Henner Kampwerth, Dong Dong Shen** for being good friends. Further special thanks belong to **Guangyao Jin** and **Ziheng Liu**. **Guangyao** trained me with piranha cleaning, RTA and changed targets and determined the depth profile of resistivity of the phosphorous-doped Ge films by plasma etching for me. **Guangyao** also encouraged me when I felt frustrated with Mantis e-beam evaporator at Bay Street at the early study stage. **Ziheng** helped me to carry out a lot of characterization and proofread my thesis.

In addition to people from our research Centre, I would like to thank those who assisted or helped me during my work. Many thanks belong to **Dr. Yu Wang** and **Dr. Anne Rich** from UNSW Analytical Centre for their trainings with XRD and Raman spectroscopy measurements, respectively. I am grateful to **Dr. Bill Bin Gong** also from Analytical Centre for helping me with XPS analysis of Ge films. I am also thankful to **Dr. Yun Lin, Sean Lim** from UNSW EMU for their training with SEM and AFM, respectively. I am also grateful to **Dr. Quadir Md Zakaria** from EMU for EBSD measurements. Special thanks go to **A/Prof. Hsi-Lien Hsiao** from Tunghai University in Taiwan for helpful discussions about some XTEM images, and **Dr. James N. Hilfiker** from J. A. Woollam Co., Inc. for the spectroscopic ellipsometry measurements and data analysis.

I would like to thank my family and friends for their support and love. Without their support and love, this work would not have been possible.

I gratefully acknowledge a 2-year sponsorship from Taiwan Power Company and an additional financial support, paying the tuition fee for my 5<sup>th</sup> semester, from ARC Photovoltaics Centre of Excellence, UNSW.

Last but not least, I would like to express my deepest thanks to my wife **Meilin Liu**, my sons **Ting-Kuei Tsao** and **Sheng-Ming Tsao** for their love, understanding and support during my entire Ph.D period.

---

---

# TABLE OF CONTENTS

---

<b>ABSTRACT.....</b>	<b>VI</b>
<b>ACKNOWLEDGEMENTS.....</b>	<b>VIII</b>
<b>TABLE OF CONTENTS.....</b>	<b>X</b>
<b>LIST OF FIGURES.....</b>	<b>XIII</b>
<b>LIST OF TABLES.....</b>	<b>XXII</b>
<b>1 INTRODUCTION.....</b>	<b>1</b>
1.1 MOTIVATION.....	1
1.2 BRIEF HISTORICAL REVIEW OF GERMANIUM.....	4
1.3 FABRICATION TECHNIQUES FOR Ge THIN FILMS.....	4
1.3.1 RF magnetron sputtering.....	7
1.3.2 General guidelines in selecting deposition conditions.....	10
1.4 THESIS OUTLINE.....	13
<b>2 POLY-Ge THIN FILMS ON GLASS .....</b>	<b>18</b>
2.1 OVERVIEW .....	18
2.2 LITERATURE REVIEW.....	18
2.3 EXPERIMENT.....	20
2.4 RESULTS AND DISCUSSION.....	24
2.4.1 Structural properties of in situ and ex situ grown poly-Ge thin films.....	24
2.4.2 Optical properties of in situ grown poly-Ge thin films.....	44
2.5 SUMMARY.....	51

---

<b>3</b>	<b><i>IN SITU</i> HYDROGENATION OF POLY-GE THIN FILMS ON GLASS BY RF SPUTTERING .....</b>	<b>53</b>
3.1	OVERVIEW.....	53
3.2	LITERATURE REVIEW.....	54
3.3	EXPERIMENT.....	56
3.4	RESULTS AND DISCUSSION .....	57
3.4.1	Deposition rate and infrared absorption measurement.....	57
3.4.2	Structural properties and morphology.....	61
3.4.3	Optical properties.....	71
3.4.4	Structural dependence of electrical properties.....	78
3.5	SUMMARY.....	88
<b>4</b>	<b>CONTROLLED DOPING OF POLY-GE THIN FILMS.....</b>	<b>91</b>
4.1	OVERVIEW.....	91
4.2	LITERATURE REVIEW.....	92
4.3	EXPERIMENT.....	95
4.3.1	Boron-doping of poly-Ge:H thin films.....	95
4.3.2	Phosphorous-doping of poly-Ge:H thin films.....	98
4.4	RESULTS AND DISCUSSION .....	100
4.4.1	Boron-doping of Poly-Ge Thin-Films.....	100
4.4.2	Phosphorus-doping of Poly-Ge Thin-Films.....	110
4.5	SUMMARY.....	118
<b>5</b>	<b><i>IN SITU</i> GROWTH OF GE-RICH POLY-SiGe:H THIN FILMS ON GLASS.....</b>	<b>120</b>
5.1	OVERVIEW.....	120
5.2	LITERATURE REVIEW.....	122
5.3	EXPERIMENT.....	123
5.4	RESULTS AND DISCUSSION.....	124
5.4.1	Surface morphology.....	124
5.4.2	Structural properties.....	127
5.4.3	Optical properties.....	133
5.4.4	Electrical properties.....	138
5.5	SUMMARY.....	139

---

<b>6</b>	<b>HETERO-EPITAXIAL GROWTH OF THIN RELAXED GE LAYERS ON SI SUBSTRAT.</b>	<b>141</b>
6.1	OVERVIEW.....	141
6.2	LITERATURE REVIEW.....	142
6.3	EXPERIMENT.....	146
6.3.1	The growth of hetero-epitaxial Ge films on Si.....	147
6.3.2	The fabrication of Ge/ Si hetero-junctions.....	148
6.4	RESULTS AND DISCUSSION.....	149
6.4.1	The hetero-epitaxial Ge films on Si .....	149
6.4.2	The Ge/Si hetero-junctions.....	158
6.5	SUMMARY.....	163
<b>7</b>	<b>CONCLUSIONS, ORIGINAL CONTRIBUTIONS AND FURTHER WORK.....</b>	<b>166</b>
7.1	CONCLUSIONS.....	166
7.1.1	Poly-Ge and poly-Ge:H thin-films on glass by RF sputtering.....	166
7.1.2	Controlled doping of poly-Ge:H thin-films on glass by RF sputtering..	169
7.1.3	Ge-rich Poly-SiGe:H thin-films on glass by RF sputtering .....	170
7.1.4	Hetero-epitaxial Growth of Thin Relaxed Ge Layers on Si Substrates	171
7.2	ORIGINAL CONTRIBUTIONS.....	171
7.2.1	Poly-Ge and poly-Ge:H thin-films on glass by RF sputtering.....	171
7.2.2	Controlled doping of poly-Ge:H thin-films on glass by RF sputtering..	172
7.2.3	Ge-rich Poly-SiGe:H thin-films on glass by RF sputtering .....	173
7.2.4	Hetero-epitaxial Growth of Thin Relaxed Ge Layers on Si Substrates	173
7.3	FURTHER WORK.....	173
7.3.1	Controlled doping of poly-Ge:H thin-films on glass by RF sputtering...	174
7.3.2	Ge-rich Poly-SiGe:H thin-films on glass by RF sputtering.....	174
7.3.3	Hetero-epitaxial growth of thin relaxed Ge layers on Si substrates.....	174
	<b>PUBLICATIONS ARISING FROM THIS THESIS.....</b>	<b>176</b>
	<b>LIST OF SYMBOLS AND ACRONYMS.....</b>	<b>178</b>
	<b>REFERENCES.....</b>	<b>183</b>

---

---

## LIST OF FIGURES

---

<b>Figure 1.1</b>	Historical development of world cumulative PV power installed from 2000 to 2009 in main geographies (Despotou et al. May 2010) .....	2
<b>Figure 1.2</b>	Comparison of the absorption coefficients of Ge, Si, and GaAs extracted from Reference (Sze and Ng 2007).....	6
<b>Figure 1.3</b>	The ATC 2200 RF magnetron sputtering system, manufactured by AJA International, employed in this thesis.....	8
<b>Figure 1.4</b>	The schematic diagram extracted from Reference (Jun et al. 2005) of the AJA ATC2200 RF magnetron sputtering system employed in this thesis.....	9
<b>Figure 1.5</b>	Temperature offset between indirect temperature (i.e. the temperature displayed on the temperature controller) and the actual temperature supplied by AJA International .....	9
<b>Figure 1.6</b>	Overview of grain structure evolution during deposition of polycrystalline thin-films (Thompson 2000).....	11
<b>Figure 1.7</b>	Microstructure zone diagram for metal films deposited by magnetron sputtering. $T_s$ is the substrate temperature and $T_m$ is the coating material melting point (Thornton 1974).....	12
<b>Figure 1.8</b>	SZM schematically representing microstructural evolution of pure elemental films as a function of the reduced temperature $T_s/T_m$ , where $T_s$ is the deposition temperature and $T_m$ is the melting point of the material, after Ref. (Petrov et al. 2003).....	13

- Figure 2.1** Raman spectra of Ge thin films on SiN<sub>x</sub>-coated glass: (a) as sputter-deposited at various temperatures, (b) sputter-deposited at RT followed by SPC for 20 hours at 400°C, 500°C, and 600°C, and (c) sputter-deposited at 255°C followed by SPC for 20 hours at 400°C, 500°C, and 600°C. Raman spectrum measured from a Ge wafer is shown as a reference..... 25
- Figure 2.2** XRD spectra of Ge thin films on SiN<sub>x</sub>-coated glass: (a) as sputter-deposited at various temperatures, (b) sputter-deposited at RT followed by SPC for 20 hours at 400°C, 500°C, and 600°C and, (c) sputter-deposited at 255°C followed by SPC for 20 hours at 400°C, 500°C, and 600°C. The bottom curves in (b) and (c) show the background contributed by the bare glass substrate..... 28
- Figure 2.3** XRD patterns of Ge thin films evaporated on glass (Corning 7059) substrate at various temperatures (Inoue and Yasuoka 1988)..... 30
- Figure 2.4** XRD patterns of Ge thin films evaporated on SiN<sub>4</sub> CVD-coated Si substrate at various temperatures (Kobayashi et al. 1997)..... 30
- Figure 2.5** Cross-sectional TEM image of the Ge film sputter-deposited at 450 °C: (a) bright-field, and (b) dark-field. Surface roughness is visible..... 32
- Figure 2.6** XRD spectra of RF sputter-deposited Si<sub>0.87</sub>Ge<sub>0.13</sub> thin films annealed for 24 h at temperature range 600 -900 °C (Choi et al. 2002)..... 34
- Figure 2.7** XRD spectra of RF sputter-deposited Si thin films annealed for 20 h at temperature range 600 -900 °C (Jun et al. 2006)..... 35
- Figure 2.8** Depth profile of the Ge film sputter-deposited at 255 °C showing various element contents. The high oxygen and Si content at surface result from the SiO<sub>2</sub> cap layer..... 35

<b>Figure 2.9</b>	UV-VIS reflectance spectra of Ge thin films on SiN <sub>x</sub> -coated glass: (a) as sputter-deposited at various temperatures, (b) sputter-deposited at RT followed by SPC for 20 hours at 400°C, 500°C, and 600°C and, (c) sputter-deposited at 255°C followed by SPC for 20 hours at 400°C, 500°C, and 600°C. A spectrum measured from a Ge wafer is shown as a reference.....	36
<b>Figure 2.10</b>	AFM images of Ge thin films on SiN <sub>x</sub> -coated glass with increasing $T_s$ : (a) RT, (b) 255°C, (c) 280°C, (d) 370°C, (e) 450°C.....	40
<b>Figure 2.11</b>	RMS roughness of the Ge thin films as a function of $T_s$ .....	42
<b>Figure 2.12</b>	SEM images of Ge thin films on SiN <sub>x</sub> -coated glass with increasing $T_s$ : (a) RT, (b) 450°C.....	44
<b>Figure 2.13</b>	The reflectance (R) and the transmission (T) spectra of Ge films sputter-deposited at various substrate temperatures: (a) R, and (b) T. Arrows across the curves indicate the increasing substrate temperature.....	46
<b>Figure 2.14</b>	Tauc plot of $(\alpha h\nu)^{1/2}$ versus photon energy $h\nu$ of Ge films sputter-deposited at various substrate temperatures based on the $\alpha$ values obtained from $R$ & $T$ .....	48
<b>Figure 2.15</b>	Refractive index $n$ and extinction coefficient $k$ spectra of Ge films sputter-deposited at various substrate temperatures: (a) $n$ (b) $k$ . Arrows across the curves indicate the trend with increasing $T_s$ . The black solid line indicates these data for c-Ge from literature (Aspnnes and Studna 1983) for reference.....	49
<b>Figure 2.16</b>	Tauc plot of $(\alpha h\nu)^{1/2}$ versus photon energy $h\nu$ of Ge films sputter-deposited at various substrate temperatures based on the $\alpha$ values obtained from SE.....	50
<b>Figure 3.1</b>	(a) Deposition rate of Ge films as a function of RF power at 1mTorr. Inset: Deposition rate as a function of flux ratio of H <sub>2</sub> , H <sub>2</sub> /(Ar + H <sub>2</sub> ), at 1.5mTorr. (b) Infrared absorption spectra of Ge:H films sputtered at various $T_s$ . An arrow across the curves indicates the increasing $T_s$ . The slight shift of the peak centres is due to the baseline tilt.....	58

<b>Figure 3.2</b>	Raman spectra of (a) Ge films presented in Chapter 2 and (b) Ge:H films on SiN <sub>x</sub> -coated glass sputtered at various $T_s$ . The peak position of a Ge wafer is depicted for reference.....	62
<b>Figure 3.3</b>	(a) The peak locations and (b) FWHM values by curve fitting for the corresponding to the Raman spectra. The peak position and FWHM of a Ge wafer are depicted for reference.....	63
<b>Figure 3.4</b>	XRD spectra of (a) Ge films presented in Chapter 2 and (b) Ge:H films on SiN <sub>x</sub> -coated glass sputtered at various $T_s$ .....	66
<b>Figure 3.5</b>	Variation of the estimated grain sizes of the Ge films and Ge:H films as a function of $T_s$ .....	67
<b>Figure 3.6</b>	Variation of RMS roughness of Ge films and Ge:H films as a function of $T_s$ . The asterisks indicate the onset crystallization temperatures.....	69
<b>Figure 3.7</b>	Typical AFM images (2 $\mu\text{m}\times 2\ \mu\text{m}$ ) of Ge films and Ge:H films on SiN <sub>x</sub> -coated glass sputtered at various $T_s$ : (a) 3D 450°C (Ge film), (b) 2D 450°C (Ge film), (c) 3D 450°C (Ge:H film), (d) 2D 450°C (Ge:H film).....	70
<b>Figure 3.8</b>	The general model used for fitting the optical properties of Ge films and Ge:H films.....	72
<b>Figure 3.9</b>	The worst case of the fitted results for the optical properties among all the samples presented in this paper: (a) $\psi$ (b) $\Delta$ from an internal Woollam report (Hilfiker 2009).....	72
<b>Figure 3.10</b>	Refractive index $n$ spectra and extinction coefficient $k$ spectra of Ge films in Chapter 2 sputtered at various $T_s$ : (a) $n$ for Ge films (b) $k$ for Ge films. The black solid line indicates the corresponding data for c-Ge from ref. (Aspnes and Studna 1983) for reference.....	74
<b>Figure 3.11</b>	Refractive index $n$ spectra and extinction coefficient $k$ spectra of Ge:H films sputtered at various $T_s$ : (a) $n$ for Ge:H films (b) $k$ for Ge:H films. The black solid line indicates the corresponding data for c-Ge from ref. (Aspnes and Studna 1983) for reference.....	75

<b>Figure 3.12</b>	Tauc plot of $(\alpha h\nu)^{1/2}$ versus photon energy $h\nu$ of (a) Ge films and (b) Ge:H films sputtered at various $T_s$ based on the $\alpha$ values obtained from SE .....	76
<b>Figure 3.13</b>	Raman spectra of (a) Ge films and (b) Ge:H films sputtered at various $T_s$ . Dotted lines at $300\text{ cm}^{-1}$ indicate the measured Raman peak position of a Ge wafer for reference.....	81
<b>Figure 3.14</b>	The Raman peak position of both series of films as a function of $T_s$ . Dotted lines at $300\text{ cm}^{-1}$ indicate the measured Raman peak position of a Ge wafer for reference.....	82
<b>Figure 3.15</b>	XRD spectra of (a) Ge films and (b) Ge:H films sputtered at various $T_s$ . A hump at around $2\theta = 22^\circ$ is attributed to the glass substrate.....	83
<b>Figure 3.16</b>	Corrected intensities of the XRD characteristic peaks as a function of substrate temperature (a) Ge films (b) Ge:H films.....	84
<b>Figure 3.17</b>	Variation of room temperature dark resistivity and conduction type of Ge films and Ge:H films on $\text{SiN}_x$ -coated glass as a function of substrate temperature. The asterisks indicate the onset crystallization temperatures.....	86
<b>Figure 3.18</b>	(a) The concentration and (b) mobility of Ge films and Ge:H films on $\text{SiN}_x$ -coated glass as a function of substrate temperature. The absence of the concentration and mobility data of the amorphous films, i.e. Ge film sputtered at $255^\circ\text{C}$ and Ge:H films sputtered at $255$ and $280^\circ\text{C}$ , is due to the lack of reliable results from Hall measurements.....	87
<b>Figure 4.1</b>	A typical results of contacts check of Ge:H film.....	98
<b>Figure 4.2</b>	The structure of the Ge:H films with <i>in situ</i> capped multi-layers designed in this work for <i>ex situ</i> phosphorous doping by RTA.....	100
<b>Figure 4.3</b>	(a) Comparison of the Raman spectra of Ge:H films as deposited at $500^\circ\text{C}$ at various power levels ( $P_B$ ) applied to the boron target. (b) Peak locations and (c) FWHM values of as deposited, $550^\circ\text{C}$ , and $600^\circ\text{C}$ annealed films as a function of power level ( $P_B$ ) applied to the boron target.....	101

<b>Figure 4.4</b>	(a) Comparison of the XRD spectra of Ge:H films as deposited at 500°C with various power levels ( $P_B$ ) (b) Calculated orientation factors of as deposited, 550°C, and 600°C annealed films as a function of power level ( $P_B$ ) applied to the boron target.....	103
<b>Figure 4.5</b>	Cross-sectional TEM micrographs of a 300 nm thick Ge film deposited at 500°C: (a) Diffraction pattern at [011] beam direction (b) Bright field image.....	105
<b>Figure 4.6</b>	Variation of (a) room temperature dark resistivity, (b) mobility, and (c) concentration of as deposited and annealed Ge:H films on $SiN_x$ -coated glass as a function of input power for sputtering boron.....	107
<b>Figure 4.7</b>	Comparison of the XRD spectra of Ge:H films as deposited at 500°C, RTA-ed at 650°C for 180 seconds, 700°C for 60 seconds, and 800°C for 20 seconds.....	111
<b>Figure 4.8</b>	Variation of room temperature sheet resistance of as deposited and annealed Ge:H films on $SiN_x$ -coated glass.....	113
<b>Figure 4.9</b>	Variation of room temperature dark resistivity of as deposited and annealed Ge:H films on $SiN_x$ -coated glass.....	114
<b>Figure 4.10</b>	Variation of room temperature mobility of as deposited and annealed Ge:H films on $SiN_x$ -coated glass.....	115
<b>Figure 4.11</b>	Variation of room temperature electrical concentration of as deposited and annealed Ge:H films on $SiN_x$ -coated glass.....	115
<b>Figure 4.12</b>	The depth profile of the sheet resistance and conduction type of the Ge:H films, annealed at (a) 650°C (b) 700°C (c) 800°C, as a function of depth below the original surface.....	118
<b>Figure 5.1</b>	2 $\mu m \times 2\mu m$ three dimensional AFM images of $Si_xGe_{1-x}:H$ films with various Si fraction: (a) $x=0.246$ , (b) $x=0.137$ , (c) $x=0.099$ , (d) $x=0.048$ .....	125
<b>Figure 5.2</b>	RMS roughness of the $Si_xGe_{1-x}:H$ films as a function of Si fraction.....	126

<b>Figure 5.3</b>	XRD spectra of the $\text{Si}_x\text{Ge}_{1-x}$ films with various Si fraction $x \leq 0.246$ sputter-deposited at $500^\circ\text{C}$ .....	128
<b>Figure 5.4</b>	Estimated grain size of the $\text{Si}_x\text{Ge}_{1-x}$ films with various Si fraction $x \leq 0.246$ sputter-deposited at $500^\circ\text{C}$ .....	129
<b>Figure 5.5</b>	Diffraction peak angles of the (111), (220), and (311) orientations of the $\text{Si}_x\text{Ge}_{1-x}$ films with various Si fraction $x \leq 0.246$ sputter-deposited at $500^\circ\text{C}$ .....	129
<b>Figure 5.6</b>	Interplanar spacings in the $\text{Si}_x\text{Ge}_{1-x}:\text{H}$ films as a function of the Si fraction.....	130
<b>Figure 5.7</b>	Raman spectra of the $\text{Si}_x\text{Ge}_{1-x}:\text{H}$ films with various Si fraction $x \leq 0.246$ sputter-deposited at $500^\circ\text{C}$ .....	132
<b>Figure 5.8</b>	The peak locations of the Ge-Ge and Si-Ge bands by Gaussian curve fitting as a function of Si fraction.....	133
<b>Figure 5.9</b>	The reflectance ( $R$ ) and the transmittance ( $T$ ) spectra of $\text{Si}_x\text{Ge}_{1-x}:\text{H}$ films sputtered with various Si fraction: (a) $R$ and (b) $T$ . Arrows across the curves indicate the decreasing Si fraction.....	135
<b>Figure 5.10</b>	A Tauc plot of $(\alpha h\nu)^{1/2}$ versus photon energy $h\nu$ of $\text{Si}_x\text{Ge}_{1-x}:\text{H}$ films sputtered at various Si fraction based on the $\alpha$ values obtained from $R$ & $T$ .....	138
<b>Figure 5.11</b>	The resistivity of the $\text{Si}_x\text{Ge}_{1-x}:\text{H}$ films as a function of Si fraction.....	139
<b>Figure 6.1</b>	Optical microscopy images of epitaxially grown Ge films on (100) Si substrate sputtered in a mixture of Ar and $\text{H}_2$ .....	150
<b>Figure 6.2</b>	Typical atomic force microscope (AFM) images ( $2\ \mu\text{m} \times 2\ \mu\text{m}$ ) of an epitaxial Ge layer on Si (100) sputter-deposited at $400^\circ\text{C}$ (a) 3 dimension (D), (b) 2D. The root-mean-square (RMS) roughness value is 0.564 nm.....	151

- Figure 6.3** Cross-sectional high resolution transmission electronic microscope (XTEM) micrographs of a typical sample, having a total thickness of about 300 nm of the Ge epitaxial layer, *in situ* capped by a ~70 nm thick SiO<sub>2</sub> layer. (a) A dislocation loop near the interface and gradually reduced threading dislocation density towards the Ge surface are visible. (b) The take-up of the lattice mismatch in a very narrow defected region near the interface with clear, but differently spaced and relaxed, lattice planes apparent in both Si and Ge materials away from the interface..... 152
- Figure 6.4** X-ray diffraction (XRD) pattern of an epitaxial Ge layer on Si (100) sputter-deposited at 400°C and a reference Ge (100) wafer..... 154
- Figure 6.5** (a) A typical electron back-scattered diffraction (EBSD) pattern at the sample (b) Miller indices of the EBSD pattern. The pattern indicates the epitaxial Ge layer is single crystal with (001) orientation..... 155
- Figure 6.6** (a) An image of a 4.4 mm×4.6 mm area from the sample measured by SEM for reference. Note only the area confined by the green square is scanned. (b) A color coded map of a 4.4 mm×4.6 mm measured area from the sample. Note the colorful area at top edge and black area at bottom edge are the areas out of the sample. (c) Orientation distribution measured from 10 different locations (distance among each is 1 mm) all over the sample. All the spots in green are located at [001] (d) An inverse pole figure of Ge [001] is provided for reference..... 156
- Figure 6.7** XRD spectra of the heavily boron-doped epitaxially grown Ge films on (100) Si substrate wafers prepared in various deposition conditions..... 159
- Figure 6.8** V<sub>OC</sub> of the epitaxially grown Ge films on Si substrate sputtered at various conditions illuminated on the Ge as well as Si side..... 160

---

<b>Figure 6.9</b>	Hetero-junction structure, which is a natural mesa structure due the partial coverage of the substrate holder on the edges of the Si wafer substrates: 0.3 $\mu\text{m}$ heavily boron-doped epitaxially grown Ge on 500 $\mu\text{m}$ Si wafer substrate. Note: the thickness 0.3 $\mu\text{m}$ of Ge layer is exaggerated.....	160
<b>Figure 6.10</b>	Optical absorption coefficients for various photo-detector materials (Sze and Ng 2007).....	161

---

---

## LIST OF TABLES

---

<b>Table 1.1</b>	Summary of some properties of Ge, Si, and GaAs. at 300K (Claeys and Simoen 2007).....	5
<b>Table 2.1</b>	The peak locations and FWHM values by curve fitting for the Raman spectra of the Ge thin films on SiN <sub>x</sub> -coated glass and of the Ge wafer shown in Figure 2.1: (a) as sputter-deposited at various temperatures, (b) sputter-deposited at RT followed by SPC for 20 hours at 400°C, 500°C, and 600°C, and (c) sputter-deposited at 255°C followed by SPC for 20 hours at 400°C, 500°C, and 600°C.....	27
<b>Table 2.2</b>	Summary of the band gaps of the films obtained by Tauc plots from two different optical measurements as a function of substrate temperature.....	51
<b>Table 3.1</b>	Summary of the estimated band gaps of the Ge films and Ge:H films obtained by Tauc plots as a function of $T_s$ .....	78
<b>Table 4.1</b>	Summary of the resistivity, mobility, and carrier concentration of the Ge:H films.....	110
<b>Table 4.2</b>	Summary of conduction types of poly-Ge:H films prepared at different conditions.....	112
<b>Table 4.3</b>	The details of the layer removal steps as well as the obtained sheet resistance and conduction type of the Ge:H films, annealed at (a) 650°C (b) 700°C (c) 800°C, as a function of depth below the original surface.....	117
<b>Table 6.1</b>	Summary of the details of wet chemical treatment procedure.....	146
<b>Table 6.2</b>	Representative patent literature about hetero-epitaxial growth of Ge on Si.....	163

# CHAPTER

# 1

## Introduction

---

- *Motivation*
- *Brief historical review of germanium*
- *Fabrication techniques for Ge thin films*
- *Thesis outline*

### 1.1 Motivation

Increased use of renewable forms of energy in place of fossil energy sources is well known to be one of the solutions to alleviate global warming. Among renewable energy technologies, photovoltaics (PV) electricity generation has been the fastest growing in the past years. Figure 1 shows the historical development of world cumulative PV power installed from 2000 to 2009 in main geographies (Despotou et al. May 2010). Most of these PV systems are based on ‘first generation’ PV devices, namely based on crystalline or multicrystalline silicon (Si) wafers. Despite the trend of the production cost dropping, mainly driven by employing thinner wafers and by increasing energy conversion efficiencies, the most significant factor in determining the cost of module production is still the Si wafer used for the fabrication of solar cells.

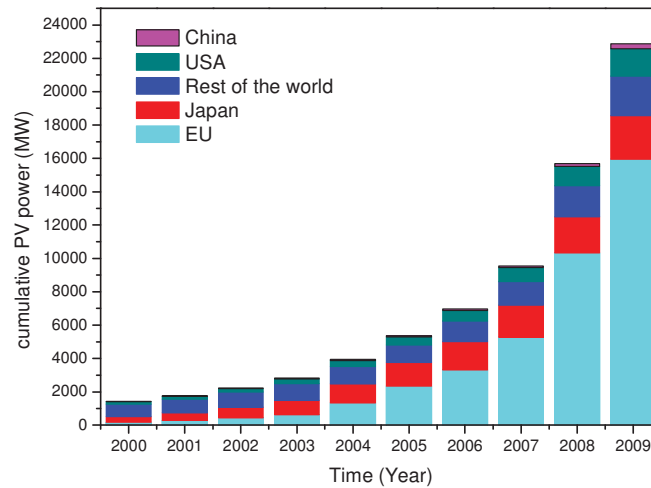


**Figure 1.1:** Historical development of world cumulative PV power installed from 2000 to 2009 in main geographies (Despotou et al. May 2010)

‘Second generation’ solar cells, based on thin-film technologies, have great potential in enhancing their share of the PV market and hence are highly attractive to researchers and investors. This is stemming from their advantages of reduced material consumption, cheaper substrates (the support material holding solar cells), and monolithic large area processing, leading to significantly lower fabrication cost. These thin-film technologies can be grouped by the semiconductor material used into amorphous silicon, copper indium diselenide/disulfide, cadmium telluride, copper-indium-gallium-diselenide (CIGS), organic dyes, and polycrystalline silicon (poly-Si) thin-films. The technology of poly-Si thin-film solar cells is promising due to its potential to combine the strengths of crystalline silicon solar cells with the aforementioned advantages of thin-film devices. Like any other single junction solar cells, nevertheless, the efficiency of poly-Si thin-film solar cells is theoretically limited by the inherent energy band gap (1.12 eV) of Si material. As a result, only light with photon energy higher than this band gap could be absorbed and thus converted into electricity. In other words, the long wavelength light will be

wasted as it just transmits through the Si material without absorption. To increase the amount of energy that can be harvested from the sunlight, a combination of semiconductor materials with different bandgap can be used. One possibility is the development of silicon (Si)/silicon germanium (SiGe)/germanium (Ge) multi-junction cells, enabling a broader wavelength band of absorbed light and thus potentially raising the cell efficiency.

Crystalline germanium (c-Ge), with a narrow band gap of 0.66 eV, has been successfully used in photovoltaic applications, such as thermophotovoltaics (Heide et al. 2009; Nagashima et al. 2003) and as the bottom cells of tandem and multijunction cells (King et al. 2007) to convert near infrared radiation into electrical energy. Despite the high cell performance achieved, these approaches require using expensive germanium (Ge) wafers, resulting in very high cell fabrication costs. Substrate cost is also presently holding back the use of SiGe alloy material in these structures, while all devices are restricted to wafer size only.

This thesis firstly focuses on the investigation of fabricating polycrystalline Ge (poly-Ge) thin films on glass to avoid the aforementioned problems and with the aim to develop a material for the bottom cells of low-cost monolithic tandem solar cells with upper cells made of SiGe alloy materials. Poly-Ge material is chosen for its inherent advantages over amorphous and intermediate phases such as its low sheet resistance, which avoids the need for using transparent conductive oxide as a back contact layer, and its long term stability. Additionally, Ge-rich SiGe alloy materials on glass by alloying the Ge with small amounts of Si are also investigated in an attempt to increase the band gap of the films. Finally, the fabrication and characterization of thin relaxed crystal Ge layers

hetero-epitaxially grown on Si substrates are studied to explore their potential in PV applications.

## 1.2 Brief historical review of germanium

Ge was found and named in 1886 by a German chemist, Clemens Alexander Winkler (Haller 2006). Around sixty years later, the first transistor, the pioneer of microelectronic devices, was fabricated using Ge in 1948 by Shockley, Bardeen, and Brattain from AT&T Bell Labs (Claeys and Simoen 2007; Haller 2006). At that time, Ge was the semiconductor material with the best crystalline quality achievable. Ge dominated the development of bipolar transistor in the following decade; however, it has been taken over by Si as a microelectronics material since early 1960s (Claeys and Simoen 2007). This mainly results from the following reasons. Firstly, the inherent narrow band gap of 0.66 eV leads to the Ge based devices suffering from high leakage current at high operating temperature (Sze 1986). Secondly, unfavorable surface properties lead Ge to be not promising for field-effect device application (Claeys and Simoen 2007). It is difficult to grow stable germanium oxide ( $\text{GeO}_2$ ) as  $\text{GeO}_2$  is unstable and soluble in water (Sze 1986). Additionally, the surface state densities at the  $\text{GeO}_2$ -Ge interface are too large for metal-oxide-semiconductor field effect transistors (MOSFET) (Haller 2006).

In contrast, Si has dominated in the world of electronic circuits and devices ever since (Haller 2006) with three unique properties including (1) a bandgap of 1.12 eV allowing operation at temperatures several hundred degrees higher than for Ge, (2) a stable oxide,

SiO<sub>2</sub>, capable of protecting device surfaces and acting as an effective mask in device fabricating, and (3) an extremely low surface state density at the SiO<sub>2</sub>-Si interface.

Recently, Ge has re-attracted research interest because of: (1) The difficulty in growing stable germanium oxide becomes insignificant when high-k materials are employed instead of SiO<sub>2</sub> (Koike et al. 2008); (2) The superior low-field hole mobility of Ge offers potential in the application of high-mobility nano-devices (Satta et al. 2005); (3) Ge is a viable candidate for integration of optical detectors and modulators on complementary-metal-oxide semiconductor (CMOS) circuits for optical interconnection due to the higher absorption coefficient in the wavelength range 800–1550 nm, combined with the higher carrier mobilities of Ge, compared to those of silicon (Claeys and Simoen 2007) ; (4) The narrower band gap of Ge capable of converting near infrared radiation into electrical energy offers opportunities in the applications of thermophotovoltaics (Nagashima et al. 2003); (5) High-quality epitaxial GaAs can be grown directly on Ge because of the similar lattice constant, enabling successful application as bottom cells of tandem and multijunction cells (King et al. 2007). Table 1.1 summarizes some properties of Ge, Si, and GaAs at 300K while Figure 1.2 compares the absorption coefficients of Ge, Si, and GaAs (Sze and Ng 2007).

Table 1.1 Summary of some properties of Ge, Si, and GaAs. at 300K (Claeys and Simoen 2007)

Property	Unit	Ge	Si	GaAs
Electron mobility	cm <sup>2</sup> /V-s	3900	1400	8500
Hole mobility	cm <sup>2</sup> /V-s	1900	450	400
Bandgap	eV	0.66	1.12	1.42
Lattice constant	Å	5.658	5.431	5.653
Dielectric constant		16.2	11.7	12.9

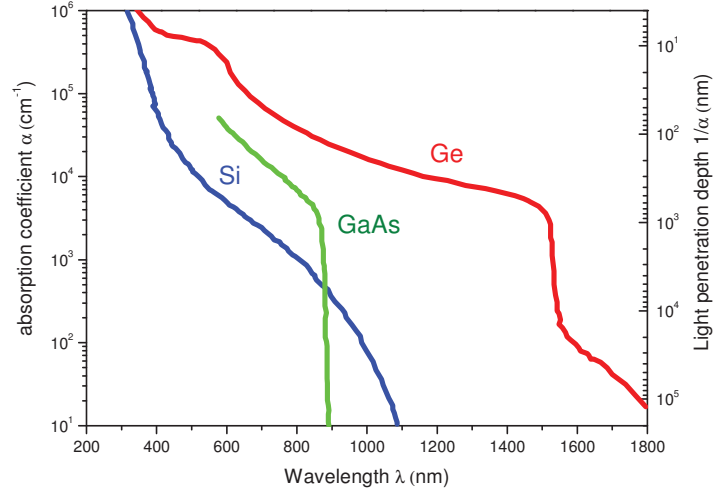


**Figure 1.2:** Comparison of the absorption coefficients of Ge, Si, and GaAs (Sze and Ng 2007).

For PV applications, theoretically, single junction Ge solar cells would suffer from their inherent low open circuit voltage  $V_{oc}$  due to the relatively high saturation current  $I_S$  stemming from the low bandgap,  $E_g$ .  $V_{oc}$  and  $I_S$  obey equations (2.1) and (2.2), respectively (Sze and Ng 2007).

$$V_{oc} = \frac{kT}{q} \ln \left( \frac{I_L}{I_S} + 1 \right) \quad (2.1)$$

where  $I_L$  is the light-generated current.

$$I_S = AqN_C N_V \left[ \frac{1}{N_A} \sqrt{\frac{D_n}{\tau_n}} + \frac{1}{N_D} \sqrt{\frac{D_p}{\tau_p}} \right] \exp \left( \frac{-E_g}{kT} \right) \quad (2.2)$$

where  $A$  is the cross-sectional area of diode,  $N_C$  and  $N_V$  the effective density of states in the conduction band and valence band,  $\tau_n$  and  $\tau_p$  the life time for electrons or holes, and  $D_e$  and  $D_h$  the diffusivity of electron or holes, respectively.

Despite the drawback in terms of the large saturation current, this narrow band gap, implying the capability of absorbing long wavelength light, makes Ge a suitable material to be used in thermophotovoltaic applications (Heide et al. 2009). In addition, the lattice constant of Ge is very close to that of GaAs, leading to the success of over 40% efficiency for triple-junction GaInP/GaInAs/Ge concentrator solar cells (King et al. 2007).

## **1.3 Fabrication techniques for Ge thin films**

### **1.3.1 RF magnetron sputtering**

To obtain poly-Ge films, both chemical vapour deposition (CVD) and physical vapour deposition (PVD) methods can be used. For CVD methods, however, the requirement for using germane, a very expensive and extremely toxic gas, is a concern. This requirement led to the exclusion of CVD methods. Accordingly, RF magnetron sputtering was chosen among PVD methods in this thesis as it is an environment-friendly, economical, non-ultra high vacuum deposition technique capable of fabricating large area films uniformly in an in-line production.

An AJA ATC2200 radio-frequency (RF) magnetron sputtering system, shown in Figure 1.3, equipped with a substrate holder heated by a quartz halogen lamp heater had been utilized to deposit thin films throughout the thesis. The schematic diagram (Jun et al. 2005) shown in Figure 1.4 illustrates the configuration of the AJA system. The system was equipped with a rotating sample stage and confocally oriented guns, capable of operating with three 4" targets as well as two 2" targets. The system was also equipped with a load-lock, via which substrates were introduced into the chamber to eliminate the need for baking the system out prior to each film deposition. Substrate temperature was controlled by a proportional–integral–derivative controller equipped with a thermocouple

as a temperature detector. Since the thermocouple was installed near the substrate holder but could not directly contact the substrate, the substrate temperatures mentioned throughout this thesis were all calibrated according to temperature calibration data using a thermocouple-probed Si wafer supplied by the manufacturer. Figure 1.5 shows the temperature calibration data, the temperature offset between indirect temperature (i.e. the temperature displayed on the temperature controller) and the actual temperature supplied by AJA International.



**Figure 1.3:** The ATC 2200 RF magnetron sputtering system, manufactured by AJA International, employed in this thesis.

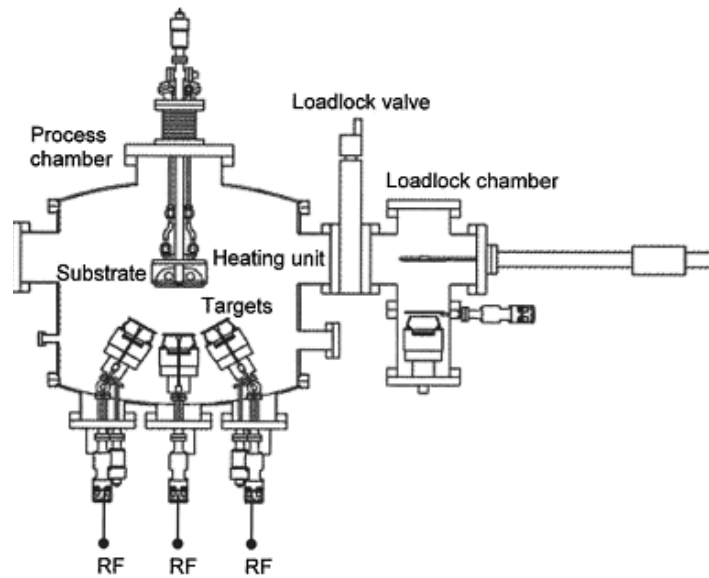


**Figure 1.4:** The schematic diagram (Jun et al. 2005) of the AJA ATC2200 RF magnetron sputtering system employed in this thesis.

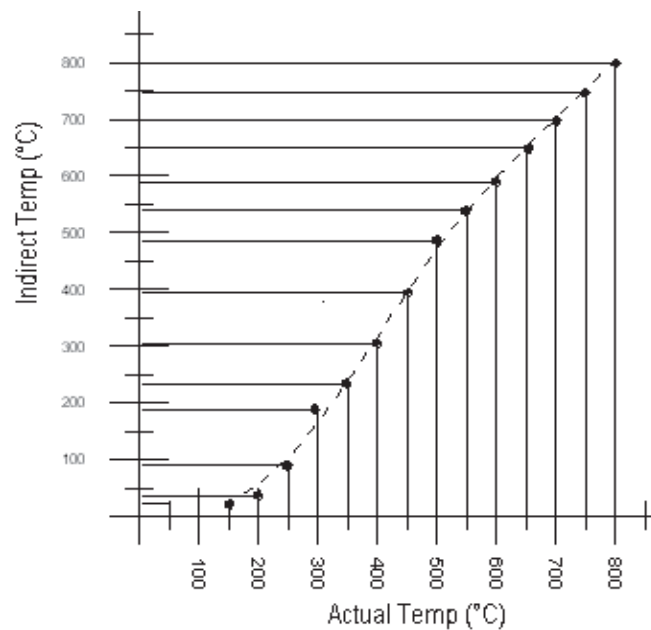


**Figure 1.5:** Temperature offset between indirect temperature (i.e. the temperature displayed on the temperature controller) and the actual temperature supplied by AJA International.

### 1.3.2 General guidelines in selecting deposition conditions

The structure of sputter-deposited films is determined mainly by deposition temperature and energetic particle bombardment, which affect the adatom mobility and hence surface diffusion of the films during growth (Thornton 1986). Appropriate low energy ion bombardment may result in denser films with improved quality. The low energy ion bombardment may be controlled by: (1) An unbalanced magnetron gun (Kelly and Arnell 2000; Shao et al. 1996); (2) Substrate DC bias (Jun et al. 2005); (3) Introduced external magnetic field (Gerbi and Abelson 2007; Gerbi et al. 2003). To narrow down the very large parameter-space, the main focus regarding deposition conditions for the experiments in this thesis was laid on the deposition temperature.

For polycrystalline thin film materials, microstructural characteristics including grain shape, grain sizes, the distribution of grain sizes and the distribution of grain orientations affect their performance in a variety of applications (Thompson 2000). To fabricate high quality polycrystalline thin films, knowledge and control of microstructural characteristics are essential. Microstructural characteristics of thin films highly depend on their growth techniques and conditions. The fundamental process through which the grain structure of polycrystalline thin films develops during film formation, outlined in Figure 1.6 (Thompson 2000), indicates high quality polycrystalline thin films may be achieved by either an *in situ* high temperature growth or a low temperature deposition followed by an *ex situ* thermal annealing process.

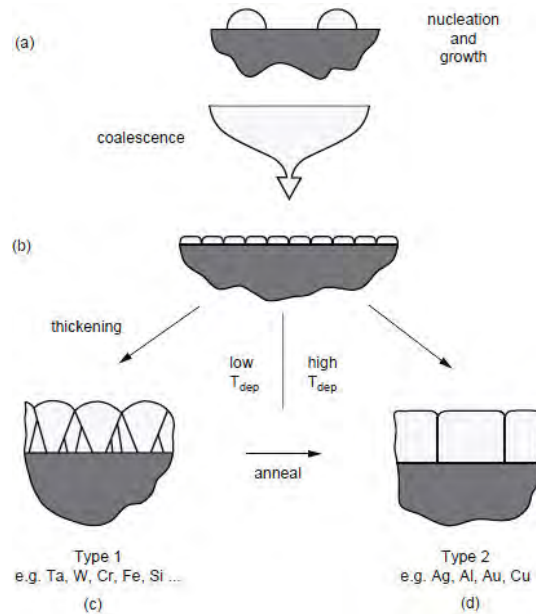


**Figure 1.6:** Overview of grain structure evolution during deposition of polycrystalline thin-films (Thompson 2000).

For the *ex situ* growth, one example is solid-phase-crystallization (SPC) of amorphous Si thin films applied in the fabrication of poly-Si thin film solar cells on glass by the author's institute and commercialized by CSG Solar (Aberle 2006). The SPC process results in a transformation of Si from amorphous to polycrystalline phase, requiring a typical temperature of around 600°C and a typical duration of about 20 hours. The resultant poly-Si films are of high quality and the roughness values of the film surfaces are insignificant, consistent with the literature (Thornton 1986). Since the melting point of Ge (937°C) is considerably lower than that of Si (1414°C), it is reasonable to expect the required SPC temperature and duration for achieving poly-Ge films would be much lower and shorter.

For *in situ* growth, Movchan and Demchishin (Movchan and Demchishin 1969) published a structure-zone model (SZM), providing an overview of the relationship

between the microstructure of evaporated coatings and homologous temperature,  $T_s / T_m$  ( $T_m$ , the melting point in degree K). Thornton extended the SZM model shown in Figure 1.7 by adding the sputtering gas pressure as an additional parameter since he observed that in sputter deposition of metal coatings, affected by the pressure, the energy, with which the atoms arrived at the film surface, could affect effective adatom mobility (Thornton 1974). The general trend in this model is that a more compact and denser film structure requires increasing the substrate temperature and reducing the sputter pressure. As the substrate temperature was used as the main controlled process parameter of the experiments in this thesis, the sputtering gas pressure of argon (or a mixture of argon and hydrogen) was set as low as possible while still maintaining stable plasma.

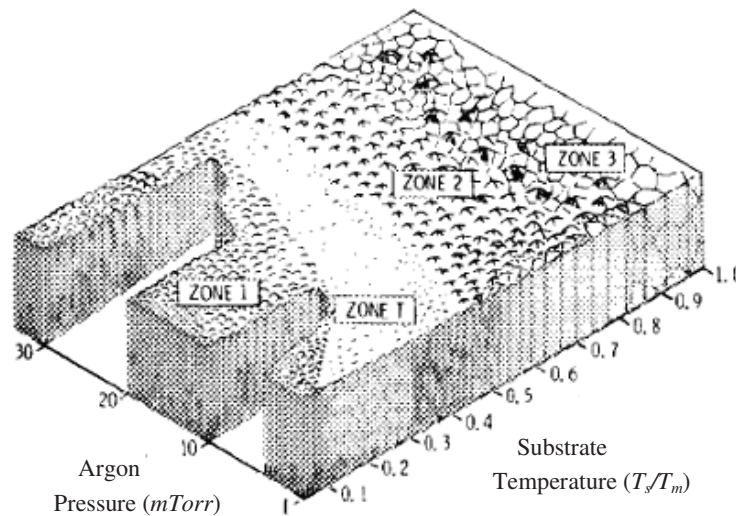


**Figure 1.7:** Microstructure zone diagram for metal films deposited by magnetron sputtering.  $T_s$  is the substrate temperature and  $T_m$  is the coating material melting point (Thornton 1974).

Figure 1.8 shows a simplified SZM model focusing on low temperature deposition, which is crucial for a broad range of industrial applications (Petrov et al. 2003). The SZM model

characterizes microstructure evolution in pure elemental films, consists of three regions, Zone I (where adatom diffusion is negligible due to very low deposition temperatures), zone T (where surface diffusion becomes significant), and zone II (where both surface and bulk diffusion are operative due to relatively high deposition temperatures). Although all the models discussed above can not be used in a detailed quantitative way, they provide general guidelines in selecting deposition conditions for the experiments in this thesis.

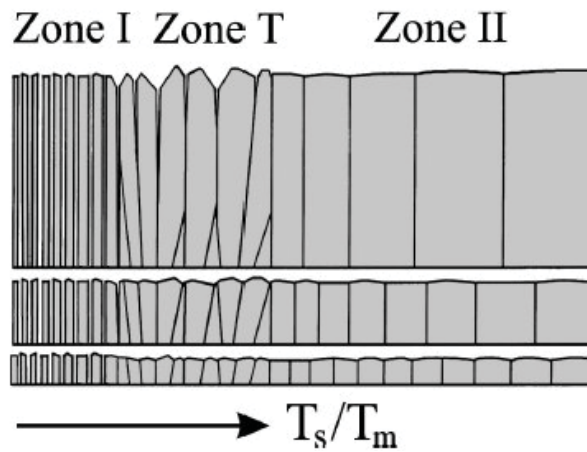


**Figure 1.8:** SZM schematically representing microstructural evolution of pure elemental films as a function of the reduced temperature  $T_s/T_m$ , where  $T_s$  is the deposition temperature and  $T_m$  is the melting point of the material (Petrov et al. 2003).

## 1.4 Thesis outline

Ge thin films and Ge-rich SiGe alloys have potential for lowering the manufacturing cost of PV devices especially in tandem solar cells. This thesis focuses on the fabrication and characterization of Ge thin films and Ge-rich SiGe alloys prepared by RF magnetron

sputtering, an inexpensive, non-ultra high vacuum deposition technique capable of fabricating large area films. The thesis consists of seven chapters.

**Chapter 1** gives the introduction to the thesis, where the motivation is given firstly, followed by a brief review of Ge in PV applications, a brief survey of fabrication techniques for Ge thin films and an introductory discussion of the role of deposition temperature during thin film growth by PVD.

**Chapter 2** investigates the fabrication of polycrystalline Ge (poly-Ge) thin films on glass by RF magnetron sputtering. The crystallinity of sputter-deposited Ge thin films on glass prepared by *in situ* growth and *ex situ* solid-phase crystallization (SPC) is firstly comparatively investigated to determine a suitable approach for growing high quality films. The influence of *in situ* deposition substrate temperature and SPC temperature ( $T_{spc}$ ) on the structural evolution of the Ge films is demonstrated. Optical properties of the *in situ* grown films are subsequently examined as it is found that poly-Ge films *in situ* crystallized at 450 °C exhibit significantly better crystal quality than those formed by SPC at 600 °C. The results from different characterization methods are discussed and compared. The change in optical properties of the *in situ* grown films from varying the substrate temperature is studied and correlated with the structural properties of the poly-Ge films.

**Chapter 3** shifts the focus of the research to the hydrogenation of the Ge films. In an attempt to further improve the properties of the Ge films, *in situ* hydrogenated Ge (Ge:H) thin films are deposited on silicon nitride ( $\text{SiN}_x$ ) coated glass at low  $T_s$  and are characterized. The structural, optical, and electrical properties of the Ge:H films are

investigated. Structural properties are examined by Raman spectroscopy and X-ray diffraction (XRD) measurements. The surface morphology of the films is analysed by atomic force microscopy (AFM). Optical constants including refractive index ( $n$ ) and extinction coefficient ( $k$ ) are derived from spectroscopic ellipsometry (SE) measurements. Using the absorption coefficient  $\alpha(k)$ , band gaps are estimated by the Tauc method (J. Tauc et al. 1966). To elucidate the structural dependence of films on the electrical properties, room temperature dark resistivity measurements are carried out by the four-point probe technique, and the conduction type of each film is identified by hot-probe measurements. The resistivity and conduction type are furthered verified by Hall-effect measurements.

**Chapter 4** studies the doping of poly-Ge:H thin-films on glass in order to demonstrate the potential of the *in situ* hydrogenated poly-Ge (poly-Ge:H) films in PV applications. P-type and n-type doping techniques for poly-Ge:H films sputter-deposited on glass are developed. P-type films are deposited and *in situ* doped by co-sputtering Ge:H with boron (B) at various power levels in a mixture of argon and hydrogen at 500°C followed by a rapid thermal anneal (RTA) process for dopant activation. On the other hand, n type films are deposited and *ex situ* doped by firstly sputter-depositing a Ge:H layer and then a SiO<sub>2</sub>/P<sub>2</sub>O<sub>5</sub>+SiO<sub>2</sub>/SiO<sub>2</sub> sandwich structure capped with a SiN layer, finally followed by a thermal drive-in process with RTA. The evidence for controlled p-type and n-type doping of poly-Ge:H films sputter-deposited on glass is presented.

**Chapter 5** extends the research scope into polycrystalline Ge-rich SiGe alloy material to explore the properties of the Ge alloyed with small amounts of Si by RF sputtering. For Si<sub>x</sub>Ge<sub>1-x</sub> alloys, in the Ge-rich region the band gap may rapidly increase with increasing

Si fraction, and then slowly increase when  $x > 0.15$ . The *in situ* hydrogenation is employed to improve the structural and electrical properties of the films. Films with a thickness of ~300 nm are as deposited at 500°C. Si and Ge atomic percentage of the films was determined by X-ray photoelectron spectroscopy (XPS). To compare the microstructure of the films grown with different Ge content, the surface morphology is analyzed by AFM while structural properties were determined by Raman and XRD measurements. For optical properties, reflectance and transmittance spectra are used to determine the absorption coefficient, from which optical band gaps are derived by using the Tauc method. The conduction type and resistivity of the films are identified and determined by hot-probe and four point-probe technique, respectively. The influence of varying Si fraction on the structural evolution, band gap shift and resistivity variation of the films is presented. The correlation between the roughness, structural, optical and electrical properties is explored and discussed.

**Chapter 6** describes the development of a novel method for growing thin relaxed single crystalline Ge hetero-epitaxial layers on Si substrates by using RF magnetron sputtering. By using this method, the need for ultra-high-vacuum condition and the use of costly and extremely toxic germane gas (the precursor of Ge) are avoided. In this way, thin relaxed single crystalline Ge epitaxial layers on Si substrate can be obtained at low cost, making the resultant Ge layer a potential virtual substrate for III-V material growth for tandem cell applications.

**Chapter 7** summaries the overall research project, with emphasis on the major results obtained throughout the thesis. The conclusions drawn from the previous chapters are presented. With regard to obtaining poly-Ge thin films, the results from this work indicate

---

clearly that the *in situ* growth method is superior to *ex situ* solid-phase crystallization. In addition, the results in terms of structural, optical, and electrical properties all consistently confirm that *in situ* hydrogenation benefits the properties of the poly-Ge films. The approaches for boron doping and phosphorus doping of sputter-deposited poly-Ge:H thin films are pursued. Moreover, the properties of Ge-rich SiGe alloy by sputtering are elucidated. Furthermore, the growth of hetero-epitaxial thin relaxed Ge layers on Si substrates by sputtering, developed in this thesis, is demonstrated to be promising for III-V material growth for tandem cell applications. Finally, the original contributions made in the course of this work are briefly summarized followed by some suggestions for further research.

# CHAPTER

# 2

## Poly-Ge Thin Films on Glass

---

---

- *Overview*
- *Literature view*
- *Experiment*
- *Results and discussion*
- *Summary*

### 2.1 Overview

This chapter explores the structural and optical properties of Ge thin films sputter-deposited on silicon nitride coated glass with the aim of developing a material for the bottom cells of low cost monolithic tandem solar cells. A literature review in Section 2.2 is given, pointing out the significance of developing a low temperature approach with low cost for obtaining high quality poly-Ge thin films on glass. Section 2.3 provides the experimental details of the work described in this chapter. The crystallinity of sputter-deposited Ge thin films on glass prepared by *in situ* growth and *ex situ* solid-phase crystallization (SPC) is comparatively investigated to determine a suitable approach for

growing high quality films. Optical properties of the *in situ* grown films are subsequently investigated as it is found *in situ* crystallized poly-Ge films at 450 °C exhibit significantly better crystalline quality than those formed by SPC at 600 °C. Section 2.4 presents the results and discussion. The influence of *in situ* deposition substrate temperature and SPC temperature ( $T_{spc}$ ) on the structural evolution of the Ge films is demonstrated. The results from different characterization methods are discussed and compared. The optical properties of the *in situ* grown films upon substrate temperature are studied and correlated with the structural properties of Ge films. Section 2.5 summarizes the findings in this chapter.

## 2.2 Literature review

Ge has been successfully used in photovoltaic applications, such as in thermo photovoltaics (Nagashima et al. 2003) and as bottom cells of tandem cells, where Ge bottom cells having a low band gap of 0.66 eV can absorb long wavelength light, resulting in an enhancement of the optical absorption capability over a wider wavelength range (King et al. 2007). Despite the high cell performance obtained, these approaches are based on expensive bulk Ge materials. To reduce the cost of the material required, poly-Ge thin films have attracted research interest in recent years. A number of techniques based on physical vapor deposition (PVD) including evaporation (Ahrenkiel et al. 1997; Inoue and Yasuoka 1988; Kobayashi et al. 1997), radio-frequency (RF) sputtering (Hoshi et al. 2005), sputtering combined with aluminium-induced crystallization (Chambouleyron et al. 2001), sputtering combined with laser crystallization (Kuo 2008; Mulato et al. 1997), and others have been investigated.

However, with most of these approaches the film quality reported was poor unless either high substrate temperature ( $T_s$ ) or an *ex situ* crystallization process was used.

The high  $T_s$  excludes the use of low cost substrates such as glass, while the extra crystallization process required increases the fabrication cost. Therefore, the development of a low-temperature approach with low cost for obtaining high quality poly-Ge thin films on glass is essential.

## 2.3 Experiment

~300 nm poly-Ge thin films on silicon nitride ( $\text{SiN}_x$ ) coated glass were grown at low  $T_s \leq 450$  °C by RF magnetron sputtering, an inexpensive, non-ultra high vacuum deposition technique capable of fabricating large area films. An AJA ATC2200 RF magnetron sputtering system equipped with a substrate holder heated by a quartz halogen lamp heater was used for Ge deposition. Films were sputtered onto glass using a 4" Ge target (99.999% purity) with an Ar process pressure of 1 mTorr and a deposition rate of ~4.86 nm/min. The Ge deposition rate was monitored by a quartz crystal deposition rate monitor and was calibrated by a stylus surface roughness detector (Dektak IIA).  $\text{SiN}_x$ -coated borosilicate glass panes (Borofloat33,  $5 \times 5$  cm<sup>2</sup>, 3 mm thick) were used as substrates.  $\text{SiN}_x$  films were deposited by plasma-enhanced chemical vapour deposition and acted as a barrier layer between the glass and the film so that diffusion of contaminants from the glass into the Ge film during subsequent thermal treatments, such as solid phase crystallization and rapid thermal annealing, of the possible devices was minimized. The  $\text{SiN}_x$ -coated glass panes were cleaned with de-ionized water in an

ultrasonic bath and were then heated at 200°C in a furnace in nitrogen ambient for 10 minutes to remove any residual moisture prior to deposition. The films were deposited by applying 150 W RF power for 3700 seconds to obtain ~300 nm thickness at different  $T_s$  of RT, 255 °C, 280 °C, 370 °C, and 450 °C, respectively. Substrates were rotated at 30 revolutions per minute during deposition to ensure the uniformity of the films. The temperature calibration data were supplied by the manufacturer of the sputter system and measured with a Si wafer as shown in Section 1.3.2. The samples deposited at RT and 255 °C were subsequently covered by a sputtered ~50 nm-thick SiO<sub>2</sub> cap layer to prevent the loss of Ge films during SPC process due to the sublimation of GeO, which is volatile and formed by the solid phase reaction between a-Ge and a-GeO<sub>2</sub> films (i.e.  $\text{Ge} + \text{GeO}_2 = 2 \text{GeO} \uparrow$ ) at about 450°C (Jishiashvili et al. 2002; Johnson et al. 2000). SPC of the as deposited films was then performed in a muffle furnace in nitrogen ambient for 20 hours at 400°C, 500°C, 600°C, respectively. The samples were then dipped in diluted hydrofluoric acid (HF) to remove the SiO<sub>2</sub> cap layers prior to characterization.

The structural properties of the films were characterised by Raman, XRD, and UV-VIS reflectance measurements. Raman spectra of both *in situ* grown and SPC-ed samples were measured at RT with a micro-Raman spectroscope (Renishaw inVia Raman Microscope) in backscattering configuration, with a 50× optical microscope objective and using an Ar<sup>+</sup> laser with wavelength of 514.5 nm as the excitation source. The penetration depth of this excitation beam is only several tens of nanometers in Ge films, leading to only a top layer less than one fifth of the total film thickness being probed (Poulsen et al. 1998). To prevent locally laser induced crystallization of amorphous Ge films during measurement, the samples were excited with the beam power limited to 4 mW. The measurement mode was static while 20 times accumulation was used to

improve the signal to noise ratio. Before measurement of the Ge films, a single crystal FZ-Si wafer, which had a narrow peak at around  $520\text{ cm}^{-1}$ , was used to calibrate the Raman system regarding wavenumber. A single crystal Ge wafer was measured as a reference.

XRD measurements of both *in situ* and *ex situ* grown samples were performed (PANalytical's X'Pert Pro materials research diffraction system) at a voltage of 45 kV and a current of 40 mA, using Cu K $\alpha$  radiation ( $\lambda = 1.5418\text{ \AA}$ ). Unlike the green laser beam used in Raman, the X ray in XRD measurement can penetrate the entire film with only about 1 % attenuation, resulting in a signal obtained by probing the whole film thickness (Poulsen et al. 1998). Cross-sectional transmission electron microscopy (XTEM, JEOL-3000F operated at 300 kV) was performed to confirm the crystallinity of grown Ge thin films. The sample cross-sections were cut with a diamond saw, glued, and then thinned with a standard mechanical polishing technique followed by argon ion milling at 3 kV.

UV-VIS reflectance measurements were performed (Cary 5G, double beam spectrophotometer with an integrating sphere) in a wavelength range of 210-600 nm. At these wavelengths, reflected light arises only from the near surface region (a few nanometers of depth). In contrast to Raman and XRD measurements, these measurements probe a much larger area of samples and hence evaluate the spatially averaged sample crystalline quality (Aberle 2006). For crystalline Ge, there are two main optical transition peaks related to an indirect transition ( $E1$ ) at 2.22 eV and a direct transition ( $E2$ ) at 4.49 eV (Yu and Cardona 2003), with the measurement range chosen to cover both peaks.

To compare the microstructure of the films grown at different temperatures, the surface morphology was analyzed by atomic force microscopy (AFM) and scanning electron microscopy (SEM). The AFM measurements were performed using the tapping mode (Digital Instruments 3000). The scan area was  $2\ \mu\text{m} \times 2\ \mu\text{m}$  while the scan rate was 0.37 Hz. The SEM measurements were performed using an acceleration voltage in the 10-20 kV range (Hitachi S4500).

The research scope was further extended into the optical properties of the films to assist in solar cell design. Reflectance and transmittance spectra are used to determine the absorption coefficient, from which optical band gaps were derived using the Tauc method. These results were checked against spectroscopic ellipsometry (SE) derived values. A double-beam UV/visible/IR spectrophotometer (Varian Cary 5G) and an attached integrating sphere (Labsphere, RSA-CA-50) were used to measure transmission and reflection spectra in the wavelength range of 210 - 2300 nm. SE measurements (Woollam Co. M-2000 variable angle spectroscopic ellipsometer equipped with WVASE32® and CompleteEASE® software) were *ex situ* performed over 190 to 1690 nm (0.73 to 6.5 eV) at 65°, 70°, and 75° incidence. To remove the light reflected from the rear surface, all the rear surfaces of the glass sample substrates were abraded, to scatter most light away from the detector. Optical properties of each material were determined by employing various fitting models- Cauchy (glass), Cody-Lorentz oscillator ( $\text{SiN}_x$ ) and a Kramers-Kronig consistent B-Spline line (Ge) (Hilfiker 2009). In addition, to model both the roughness and oxidation effects on the surface, a surface roughness layer was added and for very high roughness a separate effective medium approximation (EMA) layer was used (Hilfiker 2009).

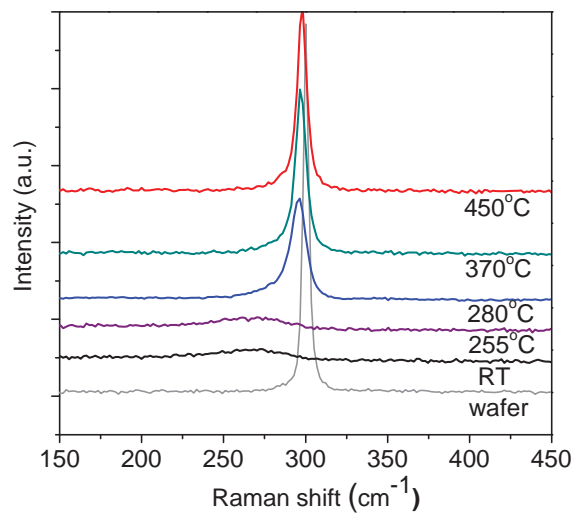
## 2.4 Results and discussion

### 2.4.1 Structural properties of *in situ* and *ex situ* grown poly-Ge thin films

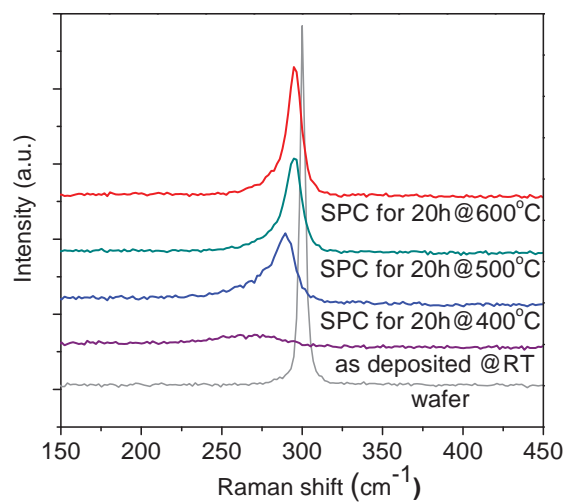
- **Raman measurements**

The structural properties of *in situ* and *ex situ* grown Ge thin films are firstly examined by Raman measurements. Figure 2.1 shows the  $T_s$  and  $T_{spc}$  dependence of Raman spectra of the *in situ* and *ex situ* grown samples: (a) as-sputter-deposited at various  $T_s$ , (b) sputter-deposited at RT followed by SPC for 20 hrs at 400°C, 500°C, and 600°C, and (c) sputter-deposited at 255°C followed by SPC for 20 hours again at 400°C, 500°C, and 600°C. A shift of the broad amorphous Ge transverse optical (TO)-phonon band ( $\sim 270$   $\text{cm}^{-1}$ ) toward the sharp mode at  $\sim 300$   $\text{cm}^{-1}$  (attributed to crystalline Ge) reveals the occurrence of the amorphous-polycrystalline transition (Evangelisti et al. 1982). Figure 2.1(a) shows the Raman spectra of as-sputter-deposited samples at different  $T_s$  compared to that of a reference Ge wafer. The peak locations and the full width at half maximum (FWHM) values determined by fitting Gaussian peaks of the samples are shown in Table 2.1(a). It can be seen that the reference Ge wafer exhibits a sharp TO peak at  $300.2$   $\text{cm}^{-1}$  while those samples deposited at RT and 255°C exhibit relatively broad TO peaks centered at about  $270$   $\text{cm}^{-1}$  corresponding to amorphous Ge (Mulato et al. 1997; Wakaki et al. 1996). These broad and less intense peaks may result from the vibration density of states modified by random ordering of atoms of amorphous Ge. The coexistence of two phases occurs at  $T_s = 280^\circ\text{C}$  as the Raman spectrum shows a main peak at  $295.2$   $\text{cm}^{-1}$  corresponding to crystalline Ge, with an appearance of amorphous portion leading to a shoulder on the lower wavenumber side. As the substrate temperature is increased to  $370^\circ\text{C}$ , the amorphous phase vanishes and a sharper symmetrical peak centered at  $297.0$   $\text{cm}^{-1}$  with the  $\text{FWHM} = 9.5$   $\text{cm}^{-1}$  appears, suggesting the film was crystallized. Once the

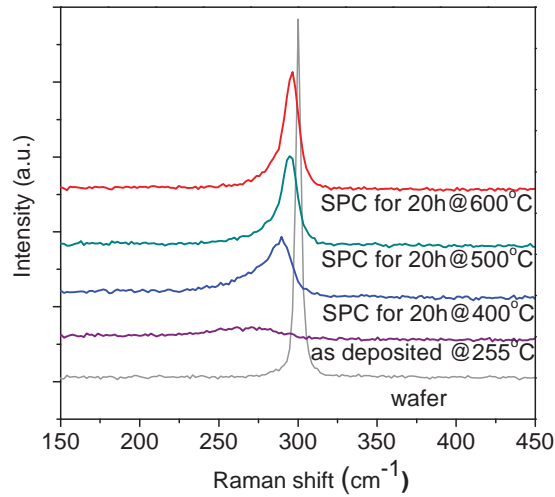
$T_s$  is further increased to 450°C, the resultant spectrum exhibits a sharp peak centered at 297.8  $\text{cm}^{-1}$  and the FWHM is further reduced to 8.3  $\text{cm}^{-1}$ . Although a shift in peak position can also be due to stress in the film, these results clearly indicate a trend that the peaks shift toward 300  $\text{cm}^{-1}$  with increasing  $T_s$  and the transition between amorphous and poly-Ge occurs at  $T_s = 255^\circ - 280^\circ\text{C}$ . The beginning of this transition temperature is similar to that reported in the literature (E. A. Stern 1983).



(a)



(b)



(c)

**Figure 2.1:** Raman spectra of Ge thin films on  $\text{SiN}_x$ -coated glass: (a) as sputter-deposited at various temperatures, (b) sputter-deposited at RT followed by SPC for 20 hours at 400°C, 500°C, and 600°C, and (c) sputter-deposited at 255°C followed by SPC for 20 hours at 400°C, 500°C, and 600°C. Raman spectrum measured from a Ge wafer is shown as a reference.

On the other hand, Figure 2.1(b) and (c) show the Raman spectra of the samples sputter-deposited at room temperature and 255°C followed by SPC for 20 hours at 400°C, 500°C, and 600°C, respectively. Table 2.1(b) and (c) show the corresponding peak locations and FWHM values. It can be seen that those samples annealed at 400°C exhibits broad asymmetrical peaks centered at 283.3  $\text{cm}^{-1}$  and 285.3  $\text{cm}^{-1}$  showing little crystallized but mainly amorphous features. In contrast, those annealed at 500°C and 600°C exhibit sharper peaks moving toward 300  $\text{cm}^{-1}$  with a narrower FWHM, indicating less amorphous tissue exists. As expected, the crystalline quality was improved with increasing  $T_{spc}$ . Interestingly, however, even SPC was performed at high  $T_s = 600^\circ\text{C}$ , the quality of the samples judged by the FWHM is still poorer than that of the sample as sputter-deposited and *in situ* crystallized at 450°C and 380°C. Also interesting is that no

obvious difference in the results is apparent between the SPC annealed samples sputter-deposited at RT and 255°C, respectively.

**Table 2.1:** The peak locations and FWHM values by curve fitting for the Raman spectra of the Ge thin films on SiN<sub>x</sub>-coated glass and of the Ge wafer shown in Figure 2.1: (a) as sputter-deposited at various temperatures, (b) sputter-deposited at RT followed by SPC for 20 hours at 400°C, 500°C, and 600°C, and (c) sputter-deposited at 255°C followed by SPC for 20 hours at 400°C, 500°C, and 600°C.

(a)

Samples as deposited at	Peak (cm <sup>-1</sup> )	FWHM (cm <sup>-1</sup> )
450°C	297.8	8.3
370°C	297.0	9.5
280°C	295.2	14.0
255°C	~270	-
RT	~270	-
wafer	300.2	4.6

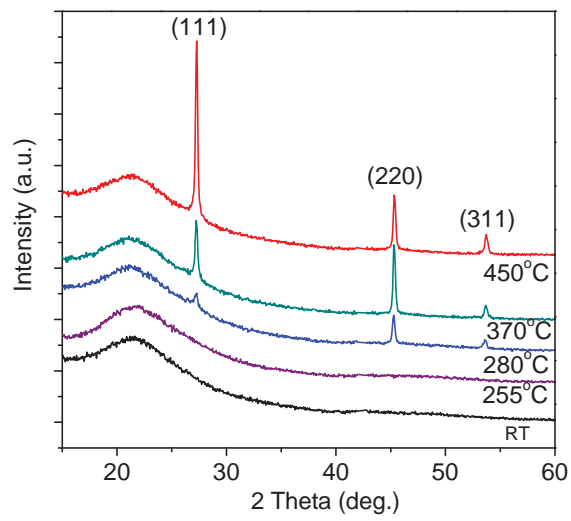
(b)

Samples	Peak (cm <sup>-1</sup> )	FWHM (cm <sup>-1</sup> )
600°C	294.8	13.3
500°C	293.9	16.1
400°C	285.3	30.8
as deposited	~270	-
wafer	300.2	4.6

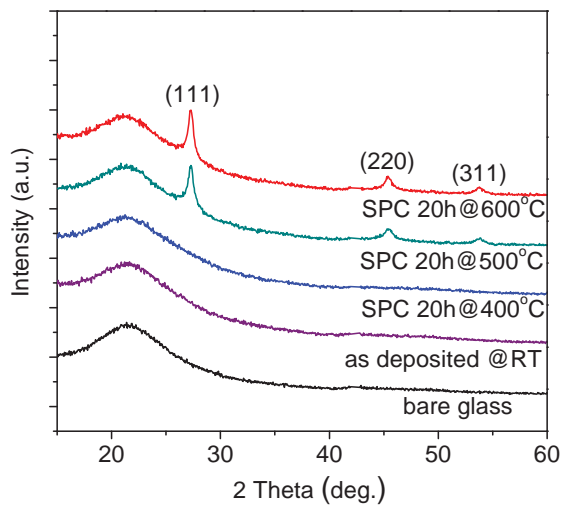
(c)

Samples	Peak (cm <sup>-1</sup> )	FWHM (cm <sup>-1</sup> )
600°C	295.3	14.4
500°C	293.8	16.2
400°C	283.3	36.7
as deposited	~270	-
wafer	300.2	4.6

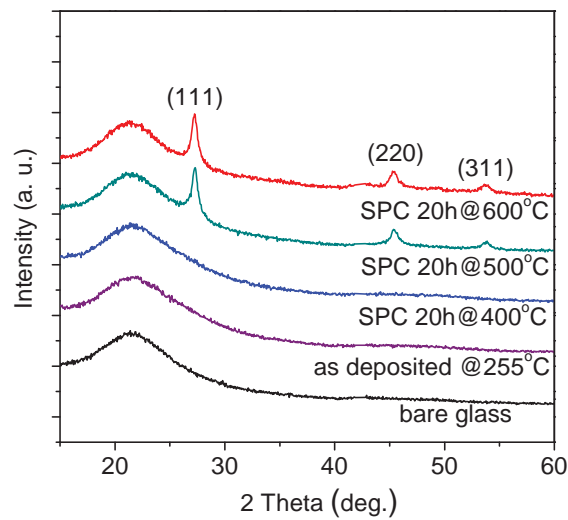
- XRD measurements



(a)



(b)



(c)

**Figure 2.2:** XRD spectra of Ge thin films on  $\text{SiN}_x$ -coated glass: (a) as sputter-deposited at various temperatures, (b) sputter-deposited at RT followed by SPC for 20 hours at 400°C, 500°C, and 600°C and, (c) sputter-deposited at 255°C followed by SPC for 20 hours at 400°C, 500°C, and 600°C. The bottom curves in (b) and (c) show the background contributed by the bare glass substrate.

The structural properties of the Ge thin films are also examined by XRD measurements. Figure 2.2 shows XRD spectra of the *in situ* crystallized and solid phase crystallized films: (a) as sputter-deposited at various  $T_s$ , (b) sputter-deposited at RT followed by SPC for 20 hours at 400°C, 500°C, and 600°C and, (c) sputter-deposited at 255°C followed by SPC for 20 hours at 400°C, 500°C, and 600°C. A hump at around 22° is attributed to the glass substrate. From Figure 2.2(a), the film deposited at RT and 255°C revealed amorphous behavior as no characteristic peaks appeared. However, when the  $T_s$  increased to 280°C, it was found that diffraction peaks appeared at around  $2\theta = 27.3^\circ$ ,  $45.3^\circ$ , and  $53.7^\circ$ , assigned to the Ge (111), Ge (220), and Ge (311) planes with (220) preferential orientation. It shows a phase transition from amorphous to crystalline phase, consistent with the Raman results above. As the  $T_s$  is increased to 370°C, the intensity of both the (111)- and (220)-oriented diffraction peaks increased significantly. In addition, the intensity of the

(111) orientation becomes gradually stronger with the increase of the  $T_s$ . Finally, the preferential orientation changes from (220) to (111) with the further increase of  $T_s$  to 450°C. The trend was in good agreement with the results reported in reference (Inoue and Yasuoka 1988; Kobayashi et al. 1997) where the XRD patterns of Ge thin films are provided in Figure 2.3 and 2.4 respectively for comparison.

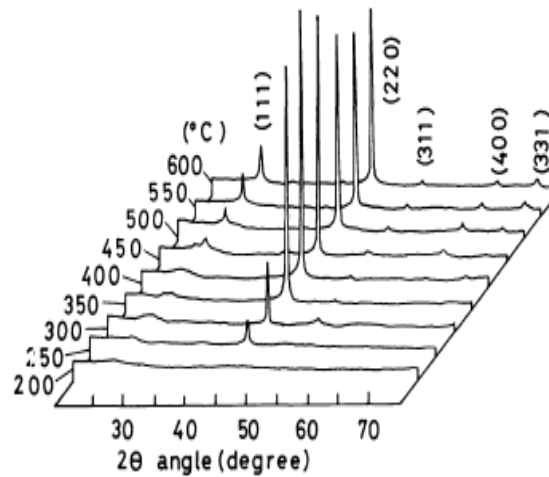


**Figure 2.3:** XRD patterns of Ge thin films evaporated on glass (Corning 7059) substrate at various temperatures (Inoue and Yasuoka 1988).

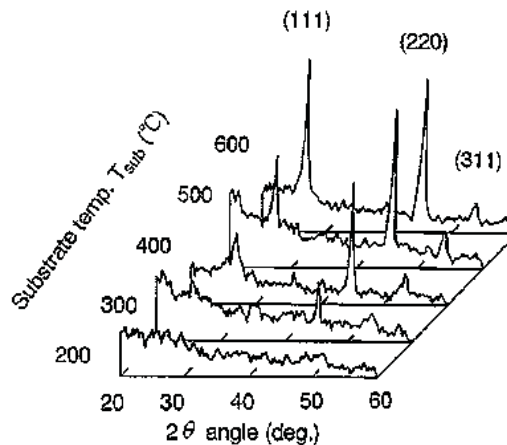


**Figure 2.4:** XRD patterns of Ge thin films evaporated on SiN<sub>4</sub> CVD-coated Si substrate at various temperatures (Kobayashi et al. 1997).

Also in agreement was reference (Hoshi et al. 2005) although the  $T_s$  of 450°C in current work was much lower than 600°C reported. Based on the strong (111) preferential

orientation observed, the film as sputter-deposited at 450°C is thought to be polycrystalline according to a reference (Maruyama et al. 1997), which suggested that preferential Ge (111) orientation is usually observed in poly-Ge films with large grain size while preferential Ge (220) orientation is usually observed in  $\mu\text{-Ge}$  films with grain size with dimensions of several tens of nanometers. This point of view is supported by the extremely strong dominant (111) peak orientation observed in a reference (Mauk et al. 2003), where Ge films having  $>1\text{mm}$  grain size were reported and also by experiments in a reference (Meng et al. 1997). The pronounced (111) orientation of our Ge thin films prepared by PVD is comparable to RF sputter-deposited films on glass deposited at 600°C with a similar thickness (Hoshi et al. 2005) or evaporated 400 nm thick Ge films on  $\text{Si}_3\text{N}_4$  CVD-coated Si substrate at 400°C followed by annealing at 900°C (Kobayashi et al. 1997).

The grain size ( $g$ ) of the film was estimated from the XRD FWHM using the well known Scherrer formula

$$g = \frac{0.9\lambda}{\Delta(2\theta)\cos\theta} \quad (2.1)$$

where  $\lambda$  is the wavelength (1.5418 Å) of the X ray,  $\theta$  is the angle satisfying Bragg's law, and  $\Delta(2\theta)$  is the FWHM in radian (Song et al. 2008a). In this estimation,  $\Delta(2\theta)$  was corrected by subtracting it from an analogous value for a reference sample (Griguceviciene et al. 2004) with  $g > 10 \mu\text{m}$  to correct for the effect of instrumental broadening (Hasegawa et al. 1995). The grain sizes were estimated to be  $\sim 20 \text{ nm}$  (280°C),  $\sim 88 \text{ nm}$  (370°C), and  $\sim 132 \text{ nm}$  (450°C), respectively. It is noted that the grain sizes seem slightly overestimated, especially for those deposited at low temperatures.

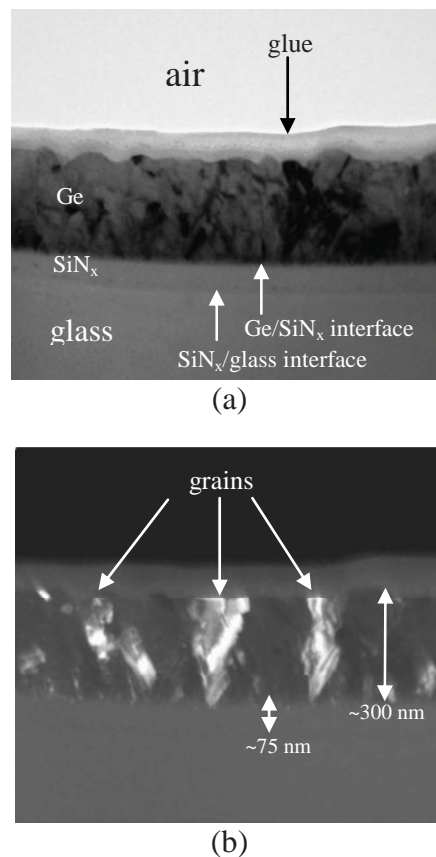


**Figure 2.5:** Cross-sectional TEM image of the Ge film sputter-deposited at 450 °C: (a) bright-field, and (b) dark-field. Surface roughness is visible.

To further confirm the crystallinity of the film, XTEM measurement was performed. Figure 2.5 shows cross-sectional bright-field and dark-field TEM images of this sample. The film structure is identified as being columnar directly from the substrate interface. Also observed are upside-down cone shape grains, typically appearing with (111) orientation, at part of regions in the images, confirming the XRD result shown in Figure 2.2(a). A part of the grains nucleate from the bottom surface and grow to the top surface while others terminate during thin film growth. The surface roughness of the film is also visible in the bright-field image.

Figure 2.2(b) and (c) shows XRD spectra of the SPC samples, which were deposited at RT and 255°C followed by SPC processes. A background contributed by the bare glass substrate is also shown for reference. These results show that even after annealing at 600°C for 20 hours, despite the (111) preferential orientation, the relative intensities of both curves are much weaker than that of the sample as sputter-deposited at 450°C. The largest grain size among the results of these SPC samples was only ~23 nm, which was estimated from the sample sputter-deposited at RT and annealed at 600°C for 20 hours. This implies that the *in situ* crystallized Ge films have better structural quality and these results in Figure 2.2 are consistent with the Raman results in Figure 2.1.

The structural characterization of Ge films crystallized by the *in situ* and *ex situ* methods shows different crystallization properties. For the *in situ* crystallization, the substrate temperature is the most critical factor affecting various thermally activated processes such as adatom diffusion on the substrate surface, the rate of adatom desorption, the rate of nucleation control, and the grain size at impingement (Thompson 2000). All these processes would considerably influence the deposited film quality. The  $T_s$  of 450°C is equivalent to about 0.6 of the homologous temperature of Ge,  $T_s / T_m$  ( $T_m$ , the melting point in degree K of material), at which surface diffusion is significant (Petrov et al. 2003). As a result, the *in situ* grown film sputter-deposited at this temperature under suitable deposition conditions has good quality. On the other hand, the as-deposited films at low  $T_s$ , at which adatom diffusion is negligible, would be underdense (Petrov et al. 2003), especially Ge is one of the materials with diamond cubic structure which has very low diffusivity at a given homologous temperature (Thompson 2000). For the *ex situ* crystallization, the smaller grain size of the SPC samples could be attributed to an abundance of nucleating sites based on the large number of defects such as dislocations,

vacancies, and stacking faults within the films (Choi et al. 2002; Jun et al. 2006). Figure 2.6 and 2.7 show XRD spectra of RF sputter-deposited SiGe (Choi et al. 2002) and Si (Jun et al. 2006) thin films annealed at elevated temperatures, indicating the difficulty for making sputter-deposited films crystallized by SPC. Note the required SPC temperature of Si films prepared by PECVD or evaporation is typically only 600°C.

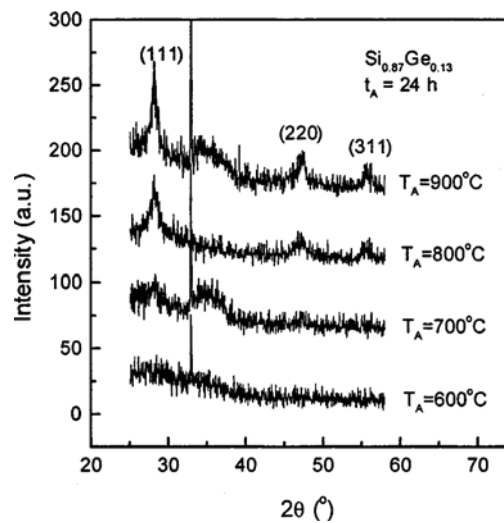


**Figure 2.6:** XRD spectra of RF sputter-deposited  $\text{Si}_{0.87}\text{Ge}_{0.13}$  thin films annealed for 24 h at temperature range 600 -900 °C (Choi et al. 2002).

Another possible reason resulting in such smaller grain size is the incorporated impurities (Choi et al. 2002) such as residual oxygen. Oxygen, known to retard silicon SPC process (Jun et al. 2006), is also very likely to affect Ge SPC process. In fact, the oxygen content of the films sputter-deposited at 255°C in this work determined by X-ray photoelectron spectroscopy (XPS) is up to 5% as shown in Figure 2.8. This high oxygen content also affects the electrical properties of the films, which will be discussed in next chapter.

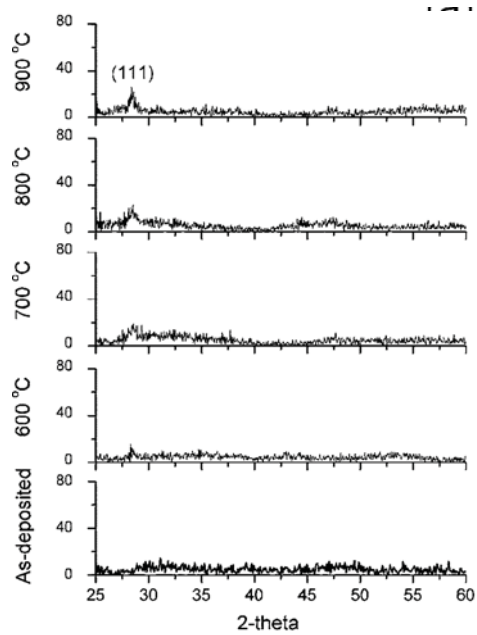


**Figure 2.7:** XRD spectra of RF sputter-deposited Si thin films annealed for 20 h at temperature range 600 -900 °C (Jun et al. 2006).

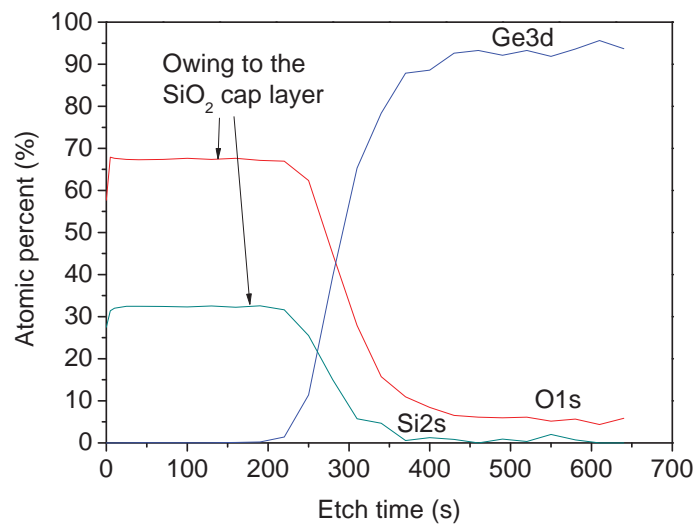
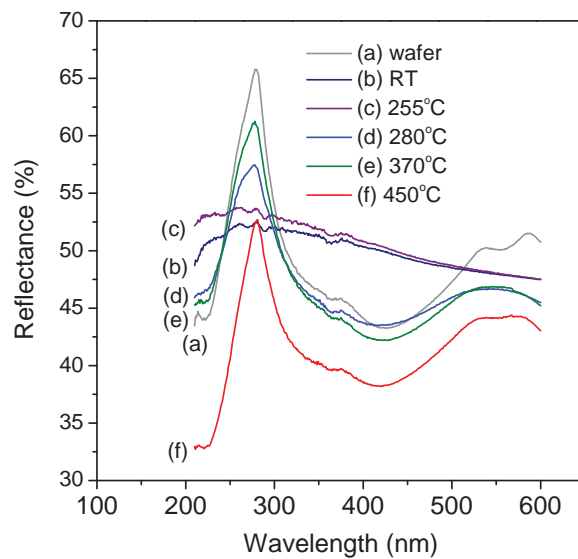


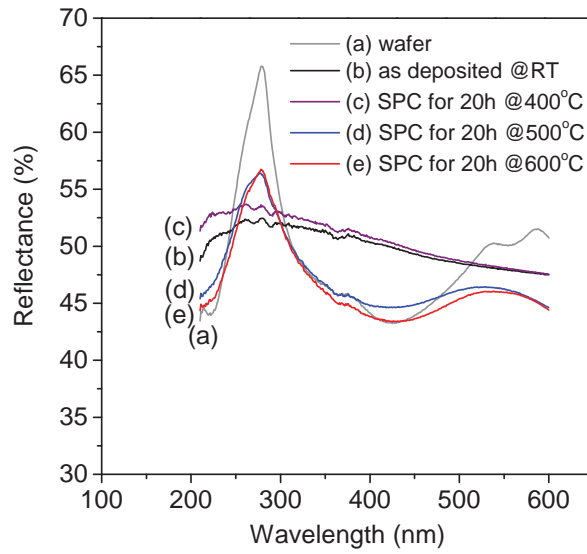
**Figure 2.8:** Depth profile of the Ge film sputter-deposited at 255 °C showing various element contents. The high oxygen and Si content at surface result from the SiO<sub>2</sub> cap layer.

- UV-VIS reflectance

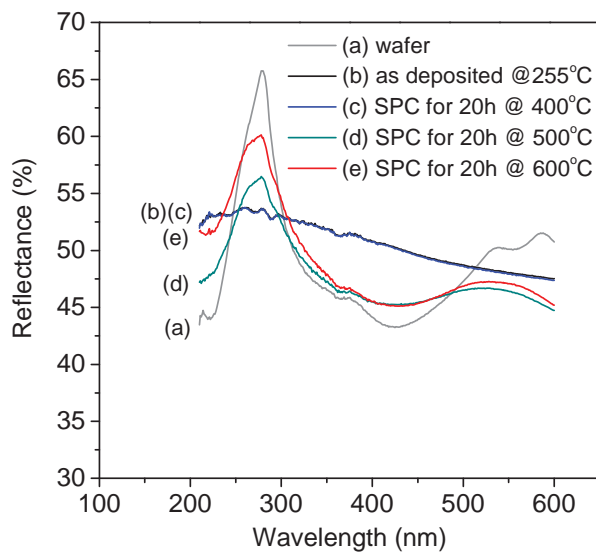
The structural properties of the Ge thin films are further examined by UV-VIS reflectance measurements. Optical reflectance at short wavelength has been widely used as non-destructive method for detecting surface damage (Zanzucchi and Frenchu 1981), measuring near-surface crystallinity (Aberle 2006; Duffy et al. 1982) in semiconductors. The deviations of reflectance spectra of samples from reference spectrum of bulk material at different wavelength may be contributed by Rayleigh scattering due to surface roughness, degree of the crystallization, and existence of a foreign surface layer (Harbeke and Jostrzebski 1990). In addition, a reduction of reflectance intensity could be caused by the antireflective property of a subwavelength surface-relief structure (Gombert et al. 1999).



(a)



(b)



(c)

**Figure 2.9:** UV-VIS reflectance spectra of Ge thin films on  $\text{SiN}_x$ -coated glass: (a) as sputter-deposited at various temperatures, (b) sputter-deposited at RT followed by SPC for 20 hours at  $400^\circ\text{C}$ ,  $500^\circ\text{C}$ , and  $600^\circ\text{C}$  and, (c) sputter-deposited at  $255^\circ\text{C}$  followed by SPC for 20 hours at  $400^\circ\text{C}$ ,  $500^\circ\text{C}$ , and  $600^\circ\text{C}$ . A spectrum measured from a Ge wafer is shown as a reference.

Figure 2.9 presents the resultant UV-VIS reflectance spectra of Ge thin films and Ge wafer reference in the wavelength range of 210~ 600 nm. The reflectance spectrum of the wafer exhibits a global maximum at ~280 nm accompanied by two local maxima at ~540 and 585 nm, as well as minima at ~430 and 555 nm, respectively. A slight shoulder is observed at ~ 380 nm. The reflectance at ~280 nm, which is dependent on the surface conditions prepared by different approaches (Donovan et al. 1963; Grant and Paul 1966), is lower than the calculated theoretical value (Aspnes and Studna 1983). This reflectance profile is in good agreement with reference (Donovan et al. 1963) except that no apparent shoulder is observed at 500 nm.

On the other hand, the samples sputter-deposited at RT and 255°C show no characteristic peaks except a weak maximum at ~280 nm (see Figure 2.9 (a)), indicating their amorphous behaviors again in agreement with the reference (Donovan et al. 1963). Nevertheless, it is noted that these two spectra are overlapped at the wavelength above 500 nm but gradually deviate from each other with decreasing wavelength. This is due to the Rayleigh scattering caused by surface roughness, dominating at shorter wavelength. The lower reflectance of the former implies its rougher surface, supported by comparing the RMS roughness values shown in Figure 2.11 for these two samples (see later discussion). Also noticed is that the maximum reflectance at 255°C is higher than that of the other, indicating less disordered structure probably resulting from the increased surface mobility.

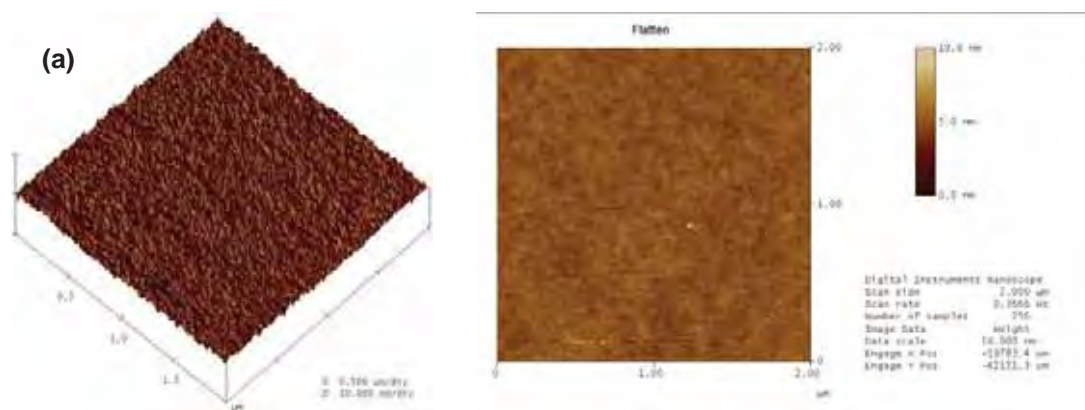
In contrast, the sample sputter-deposited at 280°C shows two distinctive peaks, but with much lower reflectance compared to those of the wafer at about ~280 nm and ~550 nm (see Figure 2.9(a)), revealing that this sample was poorly crystallized and may be

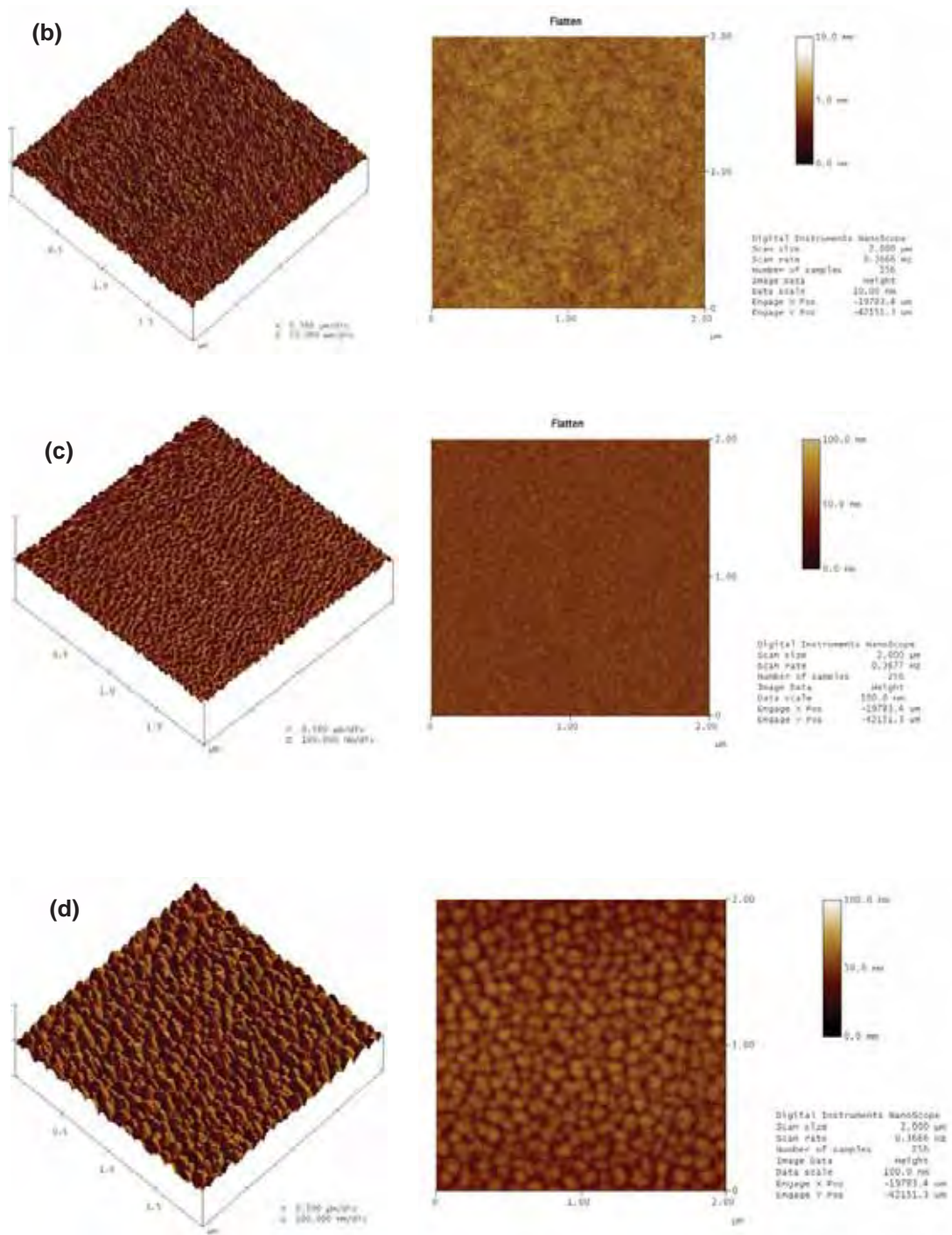
nano-crystalline at best. With the  $T_s$  increased to 370°C, the spectrum shows two peaks with increased reflectance still at about ~280 nm and the other shifted to ~560 nm, indicating this sample had better crystallinity than its previous peer. Also observed is the a bit down-shift of the reflectance over the wavelength range between ~350 nm and ~500 nm. In addition, the spectrum of the sample deposited at 450°C has the sharpest peak at about 280 nm while the other peak split into maxima at ~530 and 575 nm, showing the spectrum most resembling that of the reference wafer except with a considerable downward shift of the reflectance spectrum. The overall downshift in reflectance with increasing substrate temperature is in contrast to the apparent increase in crystal quality, which can be concluded from the increasing similarity with the Ge wafer reflectance spectrum. This apparent contradiction can be explained by the increase in surface roughness which was clearly visible in AFM images (see Figure 2.10) and the corresponding RMS roughness values (see Figure 2.11). Since the roughness feature size is much smaller than the wavelengths measured, the roughness optically behaves like a layer with a graded refractive index, which gradually changes from  $n=1$  (air) to that of the bulk poly-Ge material. This subwavelength roughness might well turn out to be beneficial for the performance of a photovoltaic device, since it behaves like an antireflection coating (Gombert et al. 1999).

The UV reflectance spectra of Ge thin films sputter-deposited at room temperature as well as at 255°C followed by SPC at different conditions were also shown in Figure 2.9 (b) and (c), respectively. It can be seen in Figure 2.9 (b) that the reflectance of the sample heated at 400°C slightly increases at shorter wavelength side including ~280 nm, an indication of less rough surface and perhaps also a less disordered microstructure. As the SPC temperature increased to 500°C, two distinctive peaks appear, a signal of structure

evolving from amorphous phase into nano-crystalline at best. Also observed is that the increase of SPC temperature to 600°C seems to cause only a small change in the reflectance spectrum. On the other hand, in Figure 2.9 (c) the reflectance of the sample sputter-deposited at 255°C and then heated at 400°C does not change at all but is similar to the corresponding one in Figure 2.9 (b). The increase of SPC temperature to 500°C results in an improvement in the reflectance spectrum while the further increase of  $T_{spc}$  to 600°C does lead to a further improvement in the reflectance spectrum. No obvious downward shift of the spectra is observed and in terms of crystallinity none of the spectra of the samples in Figure 2.9 (b) or (c), even those heated at 600 °C, is as close to the wafer spectrum as those deposited at 370°C or 450°C shown in Figure 2.9 (a). The above analysis of the results of the UV-VIS reflectance reveals that with increasing  $T_s$  not only the crystallinity of the Ge films improves, consistent with the interpretation of Raman spectra and XRD spectra, but also an antireflective property becomes stronger.

- AFM and SEM measurements





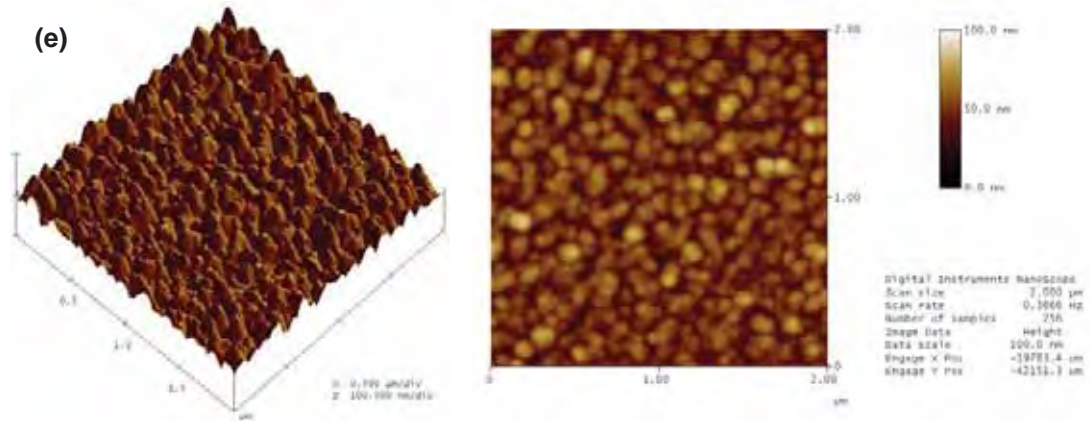


**Figure 2.10:** AFM images of Ge thin films on  $\text{SiN}_x$ -coated glass with increasing  $T_s$ : (a) RT, (b) 255°C, (c) 280°C, (d) 370°C, (e) 450°C.

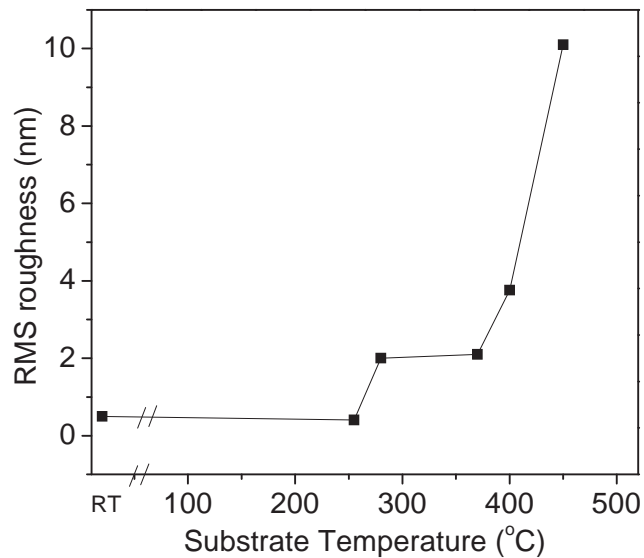
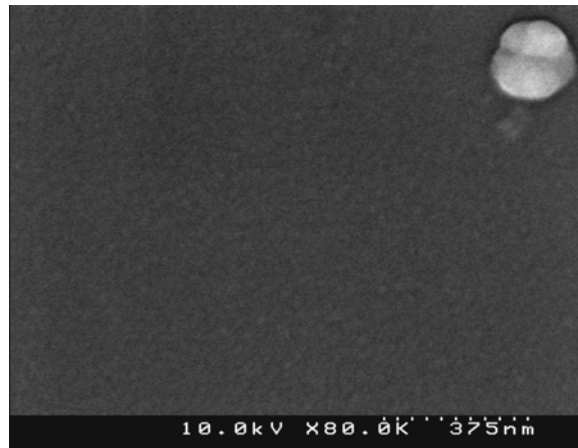


**Figure 2.11:** RMS roughness of the Ge thin films as a function of  $T_s$

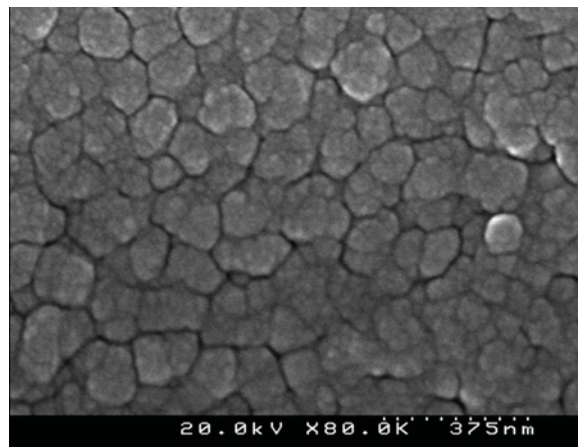
Figure 2.10 (a)-(e) show AFM images of Ge thin films on  $\text{SiN}_x$ -coated glass with various  $T_s$ : (a) RT, (b) 255°C, (c) 280°C, (d) 370°C and (e) 450°C. The scanned area is  $2 \times 2 \mu\text{m}^2$ . From the 3D AFM plots it can be seen that surface morphologies vary significantly among the films grown at different  $T_s$ . With increasing  $T_s$ , the film surface becomes

rougher. The AFM images offer clear evidence for the various extent of the reduction of UV-VIS reflection spectra in Figure 2.9. Furthermore, these AFM images can be analyzed quantitatively by the data processing software package of the Digital Instruments, allowing extracting the root-mean-square (RMS) roughness. Figure 2.11 shows RMS roughness from AFM measurements as a function of  $T_s$ . Surface roughness appears to remain low for depositions at RT and 255°C. When  $T_{spc} > 280^\circ\text{C}$ , RMS roughness increases monotonically to ~10 nm. It is thought that the surface roughness was caused by protruding crystallites similar to that reported in the literature (R. W. Collins 1985), where protruding crystallites having a height modulation of about 15 nm were reported. It is noticed that the transition temperature between amorphous and crystallized phases for the *in-situ* crystallized Ge films is between 255°C and 280°C according to the foregoing analysis of Raman, XRD, and UV-VIS measurements.

SEM micrographs in Figure 2.12 show the surface morphology of Ge thin films corresponding to the samples in Figure 2.10 (a) and (e), respectively. Both SEM images are consistent with the corresponding AFM images. There is no surface feature on the sample sputter-deposited at RT as shown in Figure 2.12. Please note that the scanning area of the former was intentionally selected to include a particle, showing that the image taken was well in focus. On the other hand, the SEM micrograph shown in Figure 2.12 exhibits clear grain boundaries and grains in 100 nm scale, consistent with the foregoing grain size estimation.



(a)



(b)

**Figure 2.12:** SEM images of Ge thin films on  $\text{SiN}_x$ -coated glass with increasing  $T_s$ : (a) RT, (b)  $450^\circ\text{C}$ .

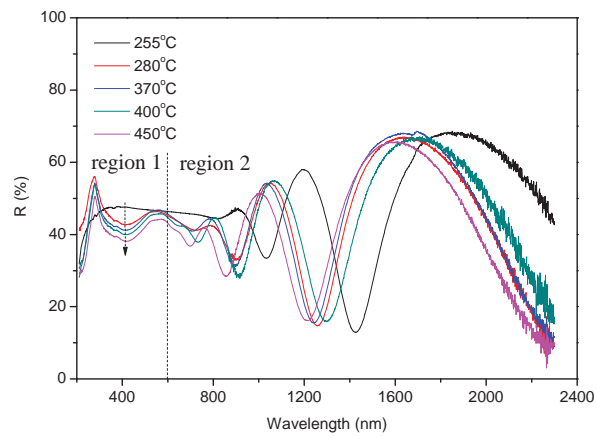
### 2.4.2 Optical properties of *in situ* grown poly-Ge thin films

In this section, the research scope is extended into the optical properties of the films to assist in solar cell design. Reflectance and transmittance spectra are used to determine the absorption coefficient, from which optical band gaps are derived using the Tauc method. These results are checked against Spectroscopic ellipsometry (SE) derived values. The

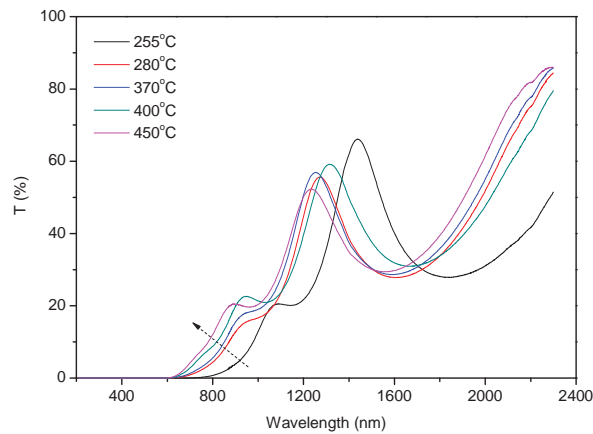
influence of how variation of  $T_s$  affects optical properties is presented. The correlation between the structural and optical properties is also studied.

- **Reflectance and transmittance**

Figure 2.13 shows the dependence of the optical reflectance ( $R$ ) and transmittance ( $T$ ) on  $T_s$ . Arrows across the curves indicate the trend with increasing  $T_s$ . For the reflectance spectra, the curves can be separated roughly into two regions of interest: wavelengths  $\lambda < \sim 600$  nm (region 1) and  $\lambda > \sim 600$  nm (region 2). In region 2, the curves exhibit interference fringes, a sign of incomplete absorption. In a tandem structured solar cell also involving indirect bandgap material such as Si, the Ge layer would be expected to share a light trapping scheme. With decreasing wavelength the envelopes bounding interference extrema decay with the onset of stronger absorption. In region 1, reflection spectra are strongly dependent on the near-surface crystallinity (Aberle 2006). The curves indicate that with increasing  $T_s$  the films change gradually from the amorphous to poly-crystalline phase (Tsao et al. 2009). Also noted is that the increasing  $T_s$  leads to apparent reflectance reduction in this region (see Figure 2.13(b)). This is not interpreted as a reduction in crystal quality, but is attributed to a graded effective refractive index because of the monotonically increasing sub-wavelength scale surface roughness, up to 10nm, as revealed by our atomic force microscopy (AFM) measurements shown earlier (Tsao et al. 2009). It is noted that how the wavelength at near-zero transmittance varies from  $\sim 800$  nm (sputter-deposited at  $255^\circ\text{C}$ ) to  $\sim 600$  nm (sputter-deposited at  $450^\circ\text{C}$ ). This blue-shift in absorption edge and the increase of absorption in the reflectance spectra suggest bonding changes in the Ge films with accompanied  $T_s$  (Song et al. 2007).



(a)



(b)

**Figure 2.13:** The reflectance ( $R$ ) and the transmission ( $T$ ) spectra of Ge films sputter-deposited at various substrate temperatures: (a)  $R$ , and (b)  $T$ . Arrows across the curves indicate the increasing substrate temperature.

Equations (2.2) and (2.3) (Demichelis et al. 1987; Song et al. 2008b) below were used to calculate the Ge absorption coefficient  $\alpha$  deduced from the  $R$  and  $T$ . This simple method can be applied because with near-normal incidence all back reflections are negligible.

$$T = (1 - R)\exp(-\alpha t), \quad (2.2)$$

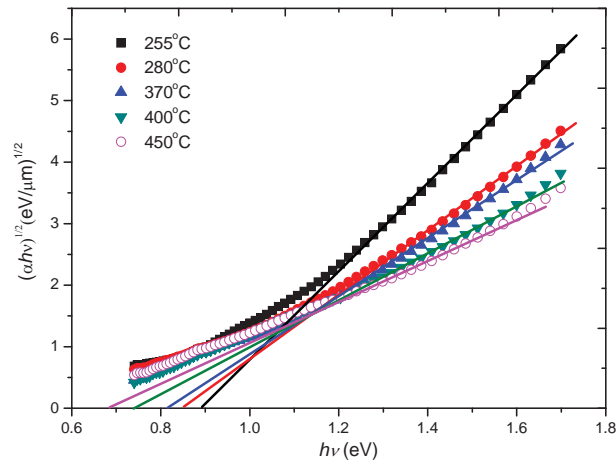
$$\alpha = \frac{1}{t} \ln \left( \frac{1-R}{T} \right), \quad (2.3)$$

where  $t$  is the thickness of the film. Equation (2.3) uses  $T$  to account for absorption and  $R$  to correct for uncoupled light and is only valid where  $T$  is nonzero.

Subsequently, the optical band gap energy ( $E_g$ ) was determined by Tauc's equation (Pilione et al. 1987; Song et al. 2008b), given as

$$(\alpha h\nu)^{\frac{1}{n}} = B(h\nu - E_g), \quad (2.4)$$

where  $h\nu$  is the photon energy,  $B$  is the edge width parameter dependent on structural disorder of films, and the exponent  $n$  depends on the type of transition. For a direct-allowed transition,  $n = 1/2$ , for an indirect-allowed transition,  $n = 2$ , and for a direct-forbidden transition,  $n = 3/2$  (Banerjee and Chattopadhyay 2005). For Ge, known as an indirect semiconductor,  $n$  was chosen as 2. Although equation (2.4) was originally developed and is most suitable for extracting the band gap for amorphous materials, it has been used to determine the band gap of nano-crystalline materials (Banerjee and Chattopadhyay 2005; Song et al. 2008b) and poly-Ge films (Tripathi et al. 2006). Here it was used to roughly estimate the band gap shift of our films.



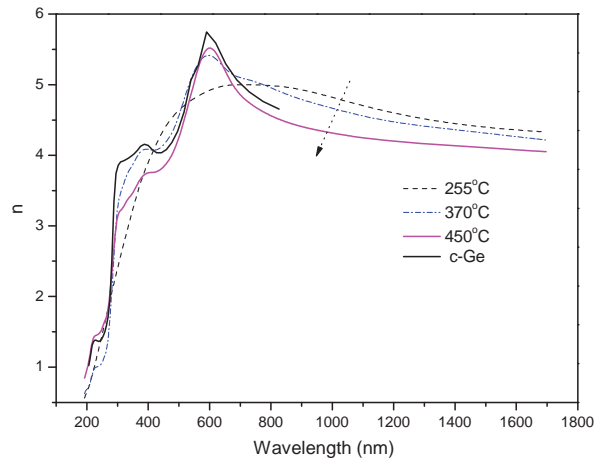
**Figure 2.14:** Tauc plot of  $(\alpha hv)^{1/2}$  versus photon energy  $hv$  of Ge films sputter-deposited at various substrate temperatures based on the  $\alpha$  values obtained from  $R$  &  $T$ .

Figure 2.14 shows a Tauc plot of  $(\alpha hv)^{1/2}$  versus photon energy  $hv$  of Ge films sputter-deposited at various  $T_s$  based on the  $\alpha$  values obtained from  $R$  &  $T$ . The linear portion was extrapolated to yield the optical band gap  $E_g$  at  $(\alpha hv)^{1/2} = 0$ . As demonstrated in the figure, there is a general trend for the band gaps to decrease with increasing  $T_s$  while the change from a knee shape curve (a-Ge) to a straight line (c-Ge) indicates the increase in crystallinity (Amutha et al. 2006). The band gap of the sample sputter-deposited at 255°C is ~0.88 eV in agreement with literature for a-Ge (Pilione et al. 1987), while that of the film sputter-deposited at 450°, is ~0.68 eV, approaching that of c-Ge. A direct correlation between crystallized degree and band gap is apparent.

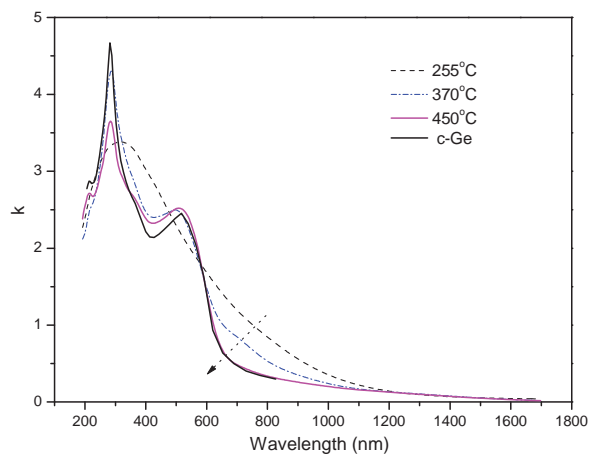
As mentioned, the above method is limited to wavelengths where  $T > 0$  (see Figure 2.13 (b)), while poor detector sensitivity over 1600 nm in  $R$  (while inline  $T$  measurement was possible, an integrating sphere, which has low throughput efficiency, had to be used for  $R$

scans) leads to high noise (see Figure 2.13(a)). SE has been used to explore outside this range, as well as to independently confirm the above findings.

- SE measurements



(a)



(b)

**Figure 2.15:** Refractive index  $n$  and extinction coefficient  $k$  spectra of Ge films sputter-deposited at various substrate temperatures: (a)  $n$  (b)  $k$ . Arrows across the curves indicate the trend with increasing  $T_s$ . The black solid line indicates these data for c-Ge from literature (Aspnes and Studna 1983) for reference.

Figure 2.15 shows dispersion in refractive index and extinction coefficient of our Ge films over a variety of  $T_s$ . The data of the films sputter-deposited at 280 °C and 370 °C, as well as 400 °C and 450 °C, are very close. For clarity, only three out of five spectra are shown accompanied with the reference  $n$  and  $k$  reported in literature (Aspnes and Studna 1983). It can be seen from the figure that the  $n$  and  $k$  values of Ge films are, as expected, strongly dependent on substrate temperature. The evolution of the  $n$  and  $k$  spectra are similar to those of polycrystalline silicon (Tompkins and McGahan 1999).

The absorption coefficient  $\alpha$  was then calculated according to the well-known equation:

$$\alpha = \frac{4\pi k}{\lambda}, \quad (2.5)$$

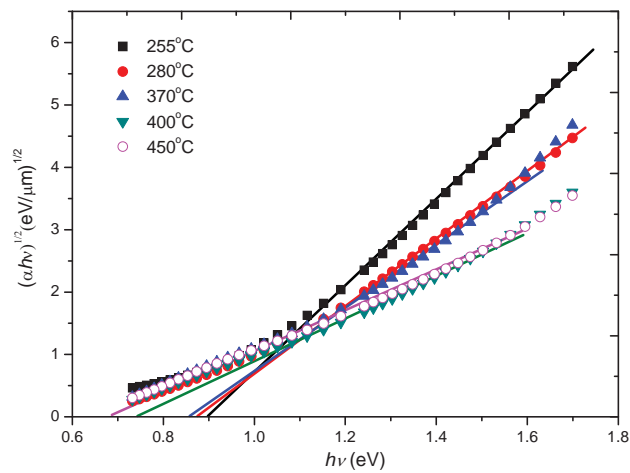


**Figure 2.16:** Tauc plot of  $(\alpha hv)^{1/2}$  versus photon energy  $h\nu$  of Ge films sputter-deposited at various substrate temperatures based on the  $\alpha$  values obtained from SE.

Based on the  $\alpha$  values obtained from SE, the band gaps of the Ge films were estimated using a Tauc plot again and are shown in Figure 2.16. Compared to Figure 2.14, the trends of both figures are in a reasonable agreement. Table 2.2 summaries the band gaps of the films obtained by Tauc plots from these two different optical measurements as a function of substrate temperature.

**Table 2.2:** Summary of the band gaps of the films obtained by Tauc plots from two different optical measurements as a function of substrate temperature.

$T_s$	255°C	280°C	370°C	400°C	450°C
$E_g$ (eV) <sup>a</sup>	0.88	0.86	0.83	0.74	0.68
$E_g$ (eV) <sup>b</sup>	0.89	0.87	0.85	0.73	0.68

<sup>a</sup>Based on the  $\alpha$  values obtained from  $R&T$

<sup>b</sup>Based on the  $\alpha$  values obtained from SE

## 2.5 Summary

Poly-Ge films were prepared by both *in situ* sputter deposition and by *ex situ* SPC annealing of sputter-deposited a-Ge films. The influence of the  $T_s$  and  $T_{spc}$  on the structural properties of the films was investigated by Raman, XRD and UV-VIS reflectance measurements. The results from these characterization techniques are all in a good agreement, indicating the transition temperature from amorphous to polycrystalline is between 255°C and 280°C for *in situ* grown poly-Ge films, whereas the transition temperature is between 400 °C and 500°C for films produced by SPC for a 20h annealing time. With increasing  $T_s$  and  $T_{spc}$ , the film structural properties characterized by Raman, XRD and UV-VIS reflectance spectra have the following features: i) Raman FWHM

decreases, ii) XRD (111) peak becomes more pronounced, which is further confirmed by XTEM measurements. iii) characteristic peaks of UV-VIS reflectance spectra become more resembling to that of bulk Ge, and iv) the RMS roughness of the films measured by AFM increases with increasing  $T_s$ . These results showed improved crystalline properties when  $T_s$  and  $T_{spc}$  increase. Compared to SPC films annealed at 600 °C, *in situ* grown Ge films are crystallized at a temperature of 450 °C and have better crystalline quality. The poor results of the SPC samples could stem from the defects and residual impurities, particularly oxygen, within the underdense films sputter-deposited at low temperature.

The correlations between the structural and optical properties of *in situ* grown Ge thin films have also been studied. Band gaps estimated by Tauc plots based on both reflectance/transmittance data as well as on SE analysed results have the same trend that band gaps decrease with increasing  $T_s$  from 255 °C to 450 °C, where the structure of the films evolves from amorphous to polycrystalline phase. The refractive index, extinction coefficient, and absorption coefficient of the films determined by SE change toward those of c-Ge as  $T_s$  increases. The poly-Ge film produced at a low  $T_s$  of 450 °C, with a band gap of ~0.68 eV, suggests the poly-Ge films could be promising for use in thin film solar cells on glass. Two papers arising from this chapter have been published in Applied Surface Science (Tsao et al. 2009) and Solar Energy Materials and Solar Cells (Tsao et al. 2010c).

## CHAPTER

# 3

## ***In Situ* Hydrogenation of Poly-Ge Thin Films on Glass by RF Sputtering**

---

---

- *Overview*
- *Literature review*
- *Experiment*
- *Results and discussion*
- *Summary*

### **3.1 Overview**

The previous chapter has investigated fabricating non-hydrogenated poly-Ge thin films on glass. In this chapter, the focus is shifted to hydrogenated films, as hydrogen properly incorporated in the material may benefit the device performance (Scheller et al. 2009). Section 3.2 gives a literature review, providing the background to the application of hydrogenation in semiconductor thin film fabrications. Section 3.3 provides the experimental detail of the work described in this chapter. In an attempt to further improve the properties of the Ge films, *in situ* hydrogenated Ge (Ge:H) thin films were deposited

on silicon nitride ( $\text{SiN}_x$ ) coated glass at low  $T_s$ . The structural and optical properties of the Ge:H films were characterized and compared with those of Ge films presented in Chapter 2. The influence of hydrogenation on the electrical properties of Ge films was also explored, with emphasis on the correlation with the structural properties. Section 3.4 presents the results and discussion. A clear influence of hydrogenation on the properties of Ge films is demonstrated. Section 3.5 summarizes the findings in this chapter.

## 3.2 Literature review

Although *ex situ* hydrogenation has been successfully employed to passivate grain boundaries and bulk defects of poly-Si thin film solar cells (Aberle 2006; Keevers et al. 2005), this post deposition process leads to an extra fabrication cost. On the other hand, *in situ* hydrogenation has been employed for obtaining high quality Ge thin films, for instance, amorphous Ge (a-Ge:H) using  $\text{GeH}_4$  by plasma enhanced chemical vapor deposition (PECVD); nanocrystalline Ge (nc-Ge:H) using  $\text{GeH}_4$  by PECVD (Poulsen et al. 1998); microcrystalline Ge ( $\mu\text{c-Ge:H}$ ) using  $\text{GeH}_4$  by CVD (Okamoto et al. 2005). To avoid the use of the extremely toxic and expensive  $\text{GeH}_4$  (germane) gas, recently T. Narita *et al.* tried to fabricate  $\mu\text{c-Ge:H}$  thin films on glass by using a Ge target reacting with hydrogen atoms generated by the hot-wire decomposition of  $\text{H}_2$  gas; however, they suffered from the extremely low deposition rate and the resultant Ge films on glass seemed only nano-crystallised even at a temperature up to  $500^\circ\text{C}$  (Narita et al. 2008). In contrast, poly-Ge films on glass could be produced by PVD techniques such as evaporation and sputtering. For evaporation, however, to obtain hydrogenated poly-Ge films usually require an *ex situ* plasma hydrogenation process since *in situ* hydrogenation by evaporation is hardly possible. For sputtering, various *in situ* hydrogenated materials

such as Ge:H (Comedi et al. 2000), Si:H (Freeman and Paul 1979), and GaAs:H (Ouyang et al. 2002) thin films were deposited in a mixture of argon (Ar) and hydrogen (H<sub>2</sub>). D. Hoshi *et al.* seems to be the first group attempting to fabricate poly-Ge:H films by RF magnetron sputtering; nevertheless, only (220) orientation preferential films, usually implying  $\mu$ c-Ge:H, could be produced even at a high substrate temperature of 600°C (Hoshi et al. 2005). Since Chapter 2 has demonstrated that poly-Ge films can be successfully produced by RF magnetron sputtering at a much lower substrate temperature of 450°C, it is interesting to explore the influence of hydrogenation on the structural and optical properties of such films.

Also interesting is to explore not only the influence of hydrogenation but also the structural dependence on the electrical properties of Ge and Ge:H thin films. Sundaram *et al.* (Sundaram and Garside 1984) reported that Ge films deposited by RF sputtering exhibited firstly p-type behaviour at higher input power. The relatively low resistivity of these p-type films increased to reach a peak as input power decreased down to about 40-50W, where the films became n-type (attributed to n-type bismuth doping) with higher resistivity which decreased with further decrease in input power (Sundaram and Garside 1984). More recently, Beensh-Marchwicka *et al.* observed that pulse magnetron sputtered antimony (Sb)-doped Ge films deposited at low temperature showed n-type behaviour with high resistivity, but when deposited at high temperature showed p-type behaviour with lower resistivity, and that this change in conduction type occurred regardless of the Sb content (Beensh-Marchwicka et al. 2001). Interestingly, each of these two groups was able to produce n-type Ge films (which tend to be naturally p-type due to acceptor-like states associated with crystallographic defects (Sundaram and Garside 1984)). This casts doubts on the effectiveness of dopants in the control of Ge film majority carrier type and

resistivity. This chapter will provide further evidence in support of the view that deposition conditions alone suffice to determine the electrical characteristics of Ge films. In particular, this work demonstrates in nominally undoped Ge and Ge:H films a general dependence of conduction type on the films' deposition temperature, and that the type switch is accompanied by a change in the preferential crystallographic orientation.

### 3.3 Experiment

Ge:H thin films were grown by reactive RF magnetron sputtering in an Ar-H<sub>2</sub> plasma with an AJA ATC2200 sputter system. The typical base pressure of the sputter system was less than  $1 \times 10^{-6}$  Torr. During the deposition the pressure in the chamber was kept at 1 mTorr. The Ar flow was kept at 15 sccm (standard cubic centimeter per minute) with the addition of H<sub>2</sub> at 10 sccm. The Ar and H<sub>2</sub> gas flows were controlled using mass flow controllers. ~300 nm thick Ge:H films were sputtered on SiN<sub>x</sub> coated glass substrates, which were electrically floating, from a 4 inch intrinsic Ge target supplied by AJA International with a purity of 99.999% with 150 W RF power at various substrate temperatures ( $T_s$ ) of 255 °C, 280 °C, 370 °C, 400 °C, and 450 °C. The hydrogen concentration in the films was varied by changing the  $T_s$ . The  $T_s$  was a calibrated temperature based on the temperature calibration data supplied and measured with a Si wafer by the manufacturer of the sputter system as described in Chapter 1. The Ge deposition rate was monitored by a crystal deposition rate monitor and was calibrated by a Dektak IIA profilometer. The details of the preparation and clean of the SiN<sub>x</sub>-coated glass substrates were given in previous chapter, where the details of Raman, XRD, and

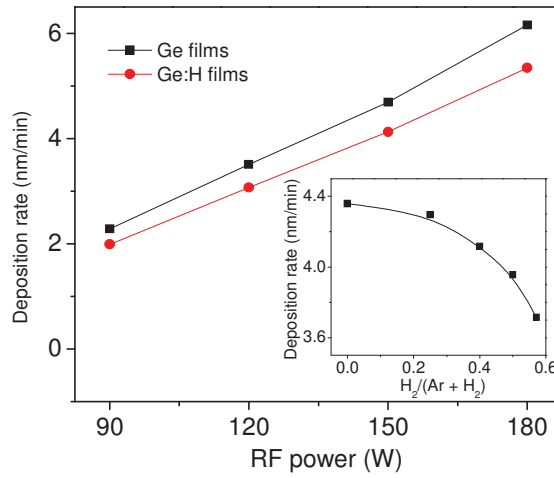
AFM measurements were also given. The methods for SE measurements and the subsequently analysis of the resultant data were the same used in the previous chapter.

To elucidate the structural dependence of films on the electrical properties, additional Ge and Ge:H films deposited at 500°C were included and characterized in terms of structural and electrical properties. Room temperature dark resistivity measurements were carried out by four-point probe technique, and the conduction-type of each film was identified by hot-probe measurements. The resistivity and conduction-type were furthered verified by Hall-effect measurements, by the Van der Pauw method at room temperature.

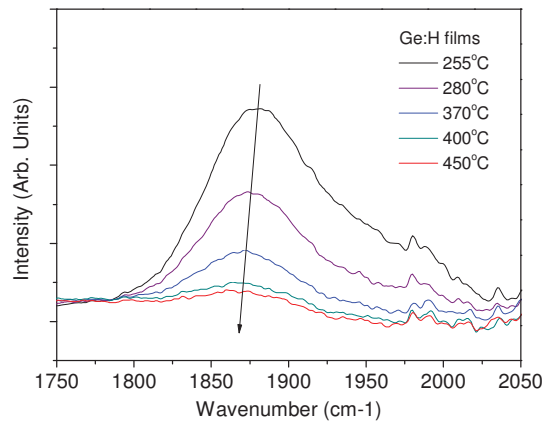
## 3.4 Results and discussion

### 3.4.1 Deposition rate and infrared absorption measurement

Figure 3.1(a) shows the average deposition rates in pure Ar gas as well as in a mixture gas of Ar and H<sub>2</sub> as a function of applied RF power. As shown, the introduction of hydrogen leads to a reduction of deposition rate. On the other hand, the inset shows the average deposition rate as a function of the ratio of hydrogen to total partial pressures, i.e. H<sub>2</sub>/(Ar + H<sub>2</sub>), under a constant total pressure of 1.5 mTorr. It can be seen, as expected, that the deposition rate decreases as this ratio increases. The decrease of deposition rate stemming from the addition of hydrogen is consistent with work on Ge:H (Comedi et al. 2000), Si:H (Freeman and Paul 1979), and GaAs:H (Ouyang et al. 2002) thin films prepared by sputtering. This is mainly because the relatively small atomic mass of hydrogen atoms results in less-efficient momentum exchange with target atoms although the ionization energies for hydrogen from H and H<sub>2</sub> to H<sup>+</sup> and H<sub>2</sub><sup>+</sup> are 13.6 and 15.24 eV, respectively, similar to that for Ar (15.76 eV)(Ouyang et al. 2002).



(a)



(b)

**Figure 3.1:** (a) Deposition rate of Ge films as a function of RF power at 1mTorr. Inset: Deposition rate as a function of flux ratio of H<sub>2</sub>, H<sub>2</sub>/(Ar + H<sub>2</sub>), at 1.5mTorr. (b) Infrared absorption spectra of Ge:H films sputtered at various T<sub>s</sub>. An arrow across the curves indicates the increasing T<sub>s</sub>. The slight shift of the peak centres is due to the baseline tilt.

As mentioned above, the hydrogen concentration in the films was varied by changing T<sub>s</sub>. To examine the bonded hydrogen incorporated in the samples with Fourier transform infrared spectroscopy, hydrogenated Ge films were simultaneously sputtered onto polished single crystal Si wafers and SiN<sub>x</sub> coated glass at 450°C. Bubbles were observed

on the films sputtered on Si wafers by optical microscope while not observed on those co-deposited on glass. Such bubbles, likely stemming from the molecular hydrogen, owing to the surface desorption of hydrogen atoms into internal voids, have also been observed in hydrogenated amorphous Ge(a-Ge:H) films deposited on single crystal Si substrates (Godet and Cabarrocas 1992). Apparently, features of Ge:H films sputtered on Si wafers are different from those sputtered on glass substrates. Therefore, attenuated total reflection (ATR) was used in the measurement, with a PerkinElmer Spectrum 100 Spectrometer equipped with a universal ATR (UATR) accessory and a spectroscopy software. The ATR is an approach requiring no special sample preparation for IR absorption measurements. The Ge:H films sputtered on glass were directly placed on the top of a crystal equipped for the UATR. A pressure was applied to the glass pane to ensure good contact between the film and the crystal, preventing any loss of IR incident radiation. A scan range  $4000\text{-}550\text{ cm}^{-1}$  was taken and 16 scans were averaged for each measurement.

It is known that a-Ge:H samples may display three typical absorption bands: the first of them corresponding to Ge-H wagging mode, centred at  $570\text{ cm}^{-1}$ , and the other two associated with Ge-H bond stretching vibrations centred at  $1874\text{ cm}^{-1}$  and at wavenumbers between  $1970$  and  $2000\text{ cm}^{-1}$ , respectively (Peng et al. 1999). By comparing the infrared absorption spectra of the Ge:H films sputtered at various  $T_s$ , a peak at  $\sim 570\text{ cm}^{-1}$ , which is commonly used to estimate the hydrogen content, only appears in the Ge:H film sputtered at  $255^\circ\text{C}$ . With increasing  $T_s \geq 280^\circ\text{C}$  no more peak at  $\sim 570\text{ cm}^{-1}$  is observed, consistent with this peak decreasing in amplitude with increasing  $T_s$  (Rudder et al. 1983). The lack of the  $570\text{ cm}^{-1}$  peak in the films makes the hydrogen content estimation difficult. Nevertheless, all the hydrogenated films exhibit visible

absorption peaks at  $\sim 1874 \text{ cm}^{-1}$  as shown in Figure 3.1(b). These peaks correspond to what are known as bulk-like modes (Peng et al. 1999; Poulsen et al. 1998) associated with hydrogen bonded in voids of the size of a Ge vacancy (Chambouleyron 1993; Peng et al. 1999), where material is compact (Zanzig et al. 1995). It is observed that the absorption peaks decrease with increasing  $T_s$ . This is because the increased mobility of Ge species with increasing temperature improves the structures of the films by lowering the density of Ge vacancy size voids and the amount of bulk-like bonded hydrogen. For instance, the substantial reduction of the peaks from  $T_s$  at 255 and 280°C to 370°C is accompanied by a structural change from amorphous to crystalline (shown later by Raman and XRD measurements).

In contrast, relatively weak peaks between 1970 and 2000  $\text{cm}^{-1}$  are also observed. It is considered these arise from a superposition of (a) peaks attributed to the  $\text{SiN}_x$  coated glass substrates and (b) the well-known surface-like mode associated with hydrogen bonded at the surface of voids (Chambouleyron 1993; Peng et al. 1999; Poulsen et al. 1998). The author observed IR peaks in this same frequency range for case (a) without attached Ge or heat treatment and found low level peaks with magnitude similar to the case with Ge for  $T_s \sim 450^\circ\text{C}$ . This suggests (b) is the main component here. Once  $T_s$  reaches  $\sim 450^\circ\text{C}$  the amount of surface-like modes with bonded hydrogen has probably decreased below the detection limit and any remaining peaks in that range arise purely from the  $\text{SiN}_x$ -coated substrate.

As  $T_s$  increases from 255 to 450°C (see Figure 3.1(b)), the height of the bulk-like peak centred around  $\sim 1874 \text{ cm}^{-1}$  decreases more noticeably than that of the surface-like peaks (1970 - 2000  $\text{cm}^{-1}$ ). This trend was not so noticeable for Mulato *et al.* (Mulato et al. 1996),

who considered the range between 75 and 340°C because surface-like peaks below 255°C are more significant, whereas over 350°C they become insignificant. It should be noted that IR spectroscopy can only detect and quantify bonded hydrogen, suitable to be employed in the present work, focusing on poly-Ge films deposited at high  $T_s$ . Nevertheless, to determine the total hydrogen content, other methods, such as ion spectroscopy, scattering or nuclear reaction techniques, would be required.

### 3.4.2 Structural properties and morphology

The influence of hydrogenation on the structural properties of the Ge films was firstly examined by Raman measurements. Figure 3.2(a) and (b) show the Raman spectra of the Ge films presented in Chapter 2 and Ge:H films sputtered at various  $T_s$ . The dotted lines at 300  $\text{cm}^{-1}$  indicate the measured Raman peak position of a Ge wafer for reference. Although it was reported that the introduction of hydrogen gas may significantly reduce the onset crystallization  $T_s$  for sputtered SiGe films (Nakamura et al. 2006), surprisingly, this is not the case for sputtered Ge films. By comparing the two figures, it can be observed that the hydrogen incorporated in the films leads to an increase of onset crystallization  $T_s$  from 280 to 370°C, similar to the increase of onset crystallization  $T_s$  from 400 to 500°C reported elsewhere (Hoshi et al. 2005). This result is also surprising as it is known that in PECVD the inclusion of hydrogen gas in the plasma may lead to a reduction of the substrate temperature required to achieve crystalline Si (Rath 2003) and Ge (Goshima et al. 1999) layers.

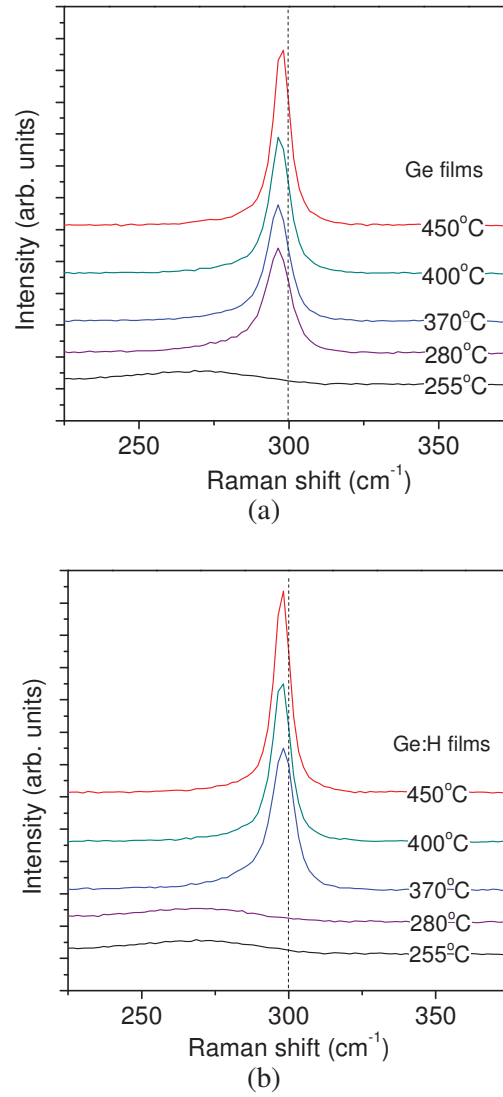


**Figure 3.2:** Raman spectra of (a) Ge films presented in Chapter 2 and (b) Ge:H films on SiN<sub>x</sub>-coated glass sputtered at various  $T_s$ . The peak position of a Ge wafer is depicted for reference.

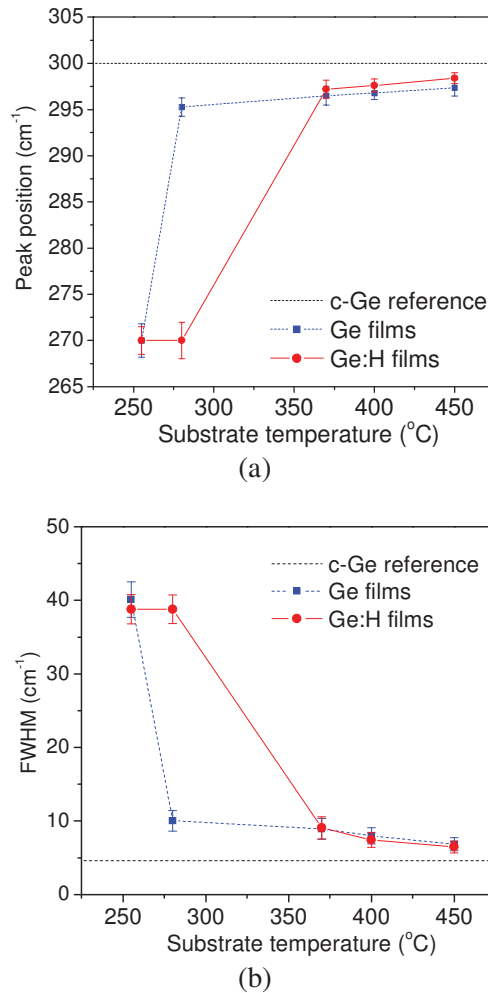


**Figure 3.3:** (a) The peak locations and (b) FWHM values by curve fitting for the corresponding to the Raman spectra. The peak position and FWHM of a Ge wafer are depicted for reference.

The increase of onset crystallization  $T_s$  is very likely caused by a reduction of particle bombardment effects. This is because in the case of sputter deposition, the adatom mobility and hence surface diffusion are mainly controlled by substrate temperature and energetic particle bombardment (Thornton 1986). An increase of substrate temperature or

ion bombardment energy can enhance surface mobility, which will enhance the onset of crystallization (Drevillon and Godet 1988). In addition to bombardment by Ar ions from the adjacent plasma, the surface of the growing Ge films during the sputtering process may be bombarded by sputtered Ge atoms and energetic neutral Ar atoms, namely Ar ions neutralized and reflected at the sputtering target, while the latter may have considerably higher energies than the former (Thornton 1986). Despite the addition of ionic H containing species and energetic neutral H reflected from the target (Myers et al. 1991), the introduction of hydrogen gas will cause a decrease of Ar gas concentration in the chamber and thus a decrease of the densities of Ar ions, sputtered Ge atoms as well as the energetic neutral Ar atoms, resulting in a reduction of the total particle bombardment energy. Consequently, the Ge:H films require a higher substrate temperature compared to their non-hydrogenated counterparts to achieve the surface mobility to crystallize.

Figure 3.3(a) and (b) depict the peak locations and the full width at half maximum (FWHM) values by Gaussian curve fitting for the Raman spectra corresponding to the Ge films and the Ge:H films shown in Figure 3.2(a) and (b). The peak position ( $300 \text{ cm}^{-1}$ ) and FWHM ( $4.6 \text{ cm}^{-1}$ ) of the Ge wafer are also depicted for reference. As shown, the peak positions of Ge films sputtered at the temperatures  $\geq 370^\circ\text{C}$  are more red-shifted than those of Ge:H films. The red shift is attributed to tensile strain due to the larger linear thermal expansion coefficient of Ge ( $5.8 \times 10^{-6} \text{ K}^{-1}$ ) compared to that of Borofloat glass ( $3.25 \times 10^{-6} \text{ K}^{-1}$ ) (Schott Inc. 2009). When deposited films cool on the glass substrates, differential thermal expansion may lead to significant tensile extrinsic strain. This biaxial strain of magnitude  $\epsilon_{th}$  can be described as (Thompson 1998)

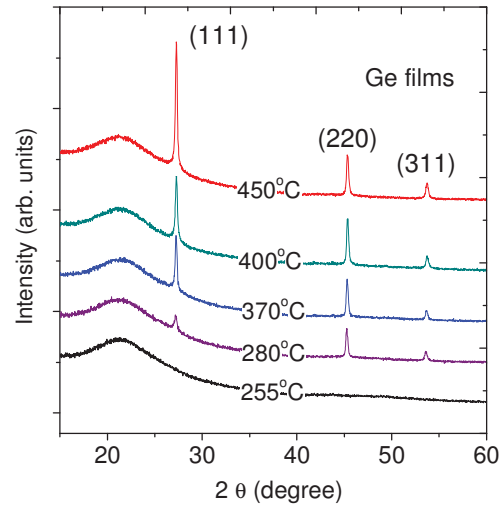
$$\epsilon_{th} = \int_{T_{dep}}^{T_r} (\alpha_f - \alpha_s) dT \approx (\Delta\alpha)(\Delta T) \quad (3.1)$$

where  $\Delta T = T_r - T_{dep}$ ,  $T_r$  and  $T_{dep}$  are the room and deposition temperatures of substrate while where  $\Delta\alpha = \alpha_f - \alpha_s$ ,  $\alpha_f$  and  $\alpha_s$  are the thermal expansion coefficients of the films and substrate, respectively. In the case of the film deposited at  $T_{dep}$  of 450°C and then cooling to room temperature (assuming 25°C), the  $\Delta T$  of 425°C would result in a  $\epsilon_{th}$  of up to 0.11%.

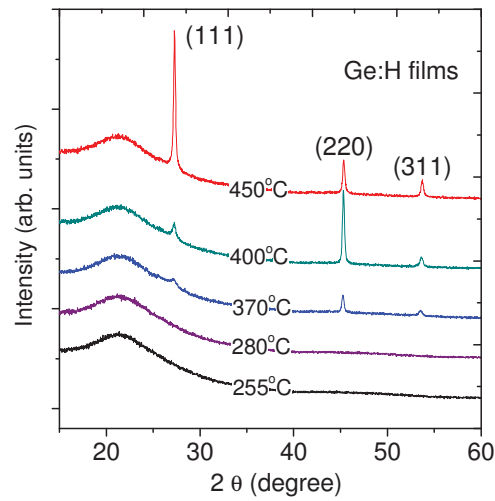
For the Ge:H films, on the other hand, the peaks approaching closer to 300  $\text{cm}^{-1}$  and the narrower FWHM are attributed to saturating the Ge dangling bonds with hydrogen, which can significantly reduce the peak shift and broadening line, as reported by Fortner *et al.* (Fortner et al. 1990). In addition, the tensile strain of the Ge:H films may be reduced by the presence of hydrogen as reported elsewhere (Hoshi et al. 2005). This is reasonable because hydrogen atoms may relax the structure of Ge films (Dalba et al. 1997) and hence be capable of reducing the strain.

- XRD measurements

The influence of hydrogenation on the structural properties of the Ge films was also examined by XRD measurements. Figure 3.4(a) and (b) show the XRD spectra of the Ge films presented in Chapter 2 and Ge:H films sputtered at various  $T_s$ . A hump at around 22° is attributed to the glass substrate. The diffraction peaks appear at around  $2\theta = 27.3^\circ$ , 45.3°, and 53.7°, corresponding to the (111), (220), and (311) crystal planes of Ge. It can be seen that the Ge:H films require a higher onset crystalline temperature compared to Ge films, and the structural evolution of both films are in agreement with the abovementioned Raman data.



(a)



(b)

**Figure 3.4:** XRD spectra of (a) Ge films presented in Chapter 2 and (b) Ge:H films on SiN<sub>x</sub>-coated glass sputtered at various  $T_s$ .

As shown, the films sputtered at temperatures  $\leq 280^\circ\text{C}$  are amorphous as no Ge characteristic peaks appear. With increasing  $T_s$  to  $370^\circ\text{C}$ , the film is (220) preferentially

oriented as it begins to crystallize. With further increasing temperature to 400°C, the intensity of the (220) orientation increases dramatically while that of (111) orientation grows slightly. Finally, when  $T_s$  increases to 450°C, the (220) orientation decreases noticeably whereas the (111) one increases significantly. Consequently, the preferential orientation changes from (220) to (111). The trend is in good agreement with others (Hoshi et al. 2005; Inoue and Yasuoka 1988; Kobayashi et al. 1997) except that in the case  $T_s = 450^\circ\text{C}$  the film has (111) preferential orientation while that of the film with a similar thickness reported elsewhere (Hoshi et al. 2005) was dominated by the (220) orientation up to 600°C. Based on the strong (111) preferential orientation observed, the Ge:H film sputtered at 450°C is thought to be polycrystalline. It is noted that the intensity of this strong (111) preferential orientation is higher than its non-hydrogenated counterpart shown in Figure 3.4(a), suggesting its higher degree of crystalline perfection (Choi et al. 2002).

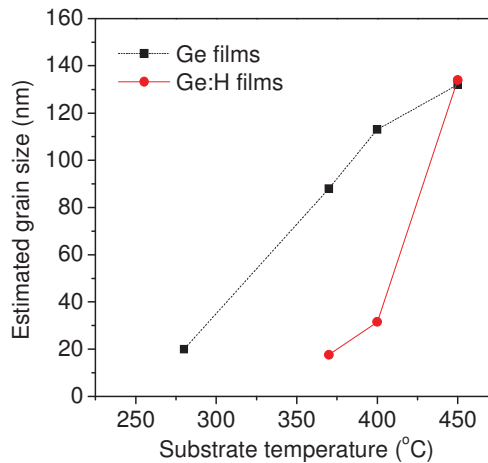


**Figure 3.5:** Variation of the estimated grain sizes of the Ge films and Ge:H films as a function of  $T_s$ .

Figure 3.5 compares the estimated grain sizes of the Ge films and Ge:H films. The grain sizes ( $g$ ) of the films were estimated from the FWHM of (111) XRD characteristic peaks using a modified version of the Scherrer formula

$$g = \frac{0.9\lambda}{B \cos \theta} \quad (3.2)$$

where  $\lambda$  is the wavelength (1.5418 Å) of the X ray,  $\theta$  is the angle satisfying Bragg's law,  $B$  is the FWHM in radians corrected for instrumental broadening. The calculation of  $B$  is commonly expressed in two classical forms for simply separating “size” and “strain” broadening effects (Mittermeijer and Scardi 2004):

$$B = B_o - B_i \quad (3.3)$$

$$\text{Or } B^2 = B_o^2 - B_i^2 \quad (3.4)$$

where  $B_o$  is the FWHM measured for the sample, and  $B_i$  is the FWHM measured for the reference material. It is found that the use of  $B$  derived from Equation (3) or (4) can lead to significantly different grain size estimates. For instance, the grain size of the Ge film sputtered at 450°C estimated by employing Equation (3) and (4) is ~130 nm and ~52 nm, respectively. The discrepancy is because these simplified approaches for estimating grain size are semi-quantitative and do not account for various types of micro-structural details (Mittermeijer and Welzel 2008). The grain size of this sample revealed by transmission electron microscopy is over 100 nm (Tsao et al. 2010c). Therefore, it seems more reasonable to adopt Equation (3) as here the focus is on the films deposited at high  $T_s$  although it slightly overestimates the grain sizes. As shown in the figure, for sputtering at lower  $T_s \leq 400^\circ\text{C}$ , the Ge:H films have much smaller grain sizes than their non-hydrogenated counterparts. However, once the  $T_s$  increases to 450°C, the poly-Ge:H film appears to have a slightly larger grain size than the poly-Ge film.

- AFM measurements

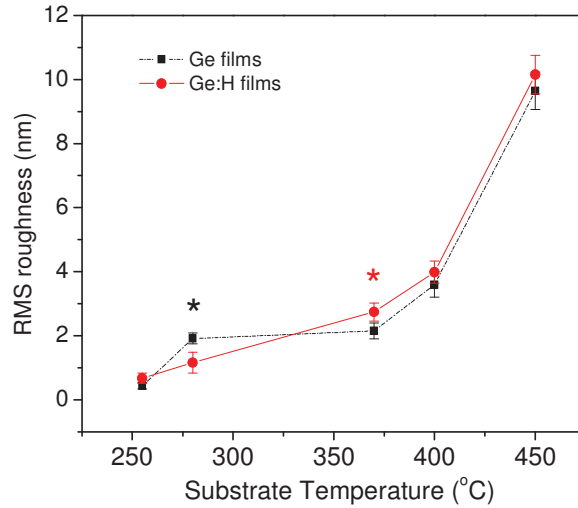


**Figure 3.6:** Variation of RMS roughness of Ge films and Ge:H films as a function of  $T_s$ . The asterisks indicate the onset crystallization temperatures.

The influence of hydrogenation on the surface morphology of the Ge films was examined by AFM measurements. Figure 3.6 depicts the variation of root-mean-square (RMS) roughness of the Ge films and Ge:H films as a function of  $T_s$ . The asterisks indicate the onset crystallization temperatures. As shown in the figure, the RMS roughness is strongly dependent on the crystallinity of the films. It is thought that the surface roughness was caused by protruding crystallites similar to that reported in the literature (R. W. Collins 1985).

Figure 3.7(a)-(d) show the typical  $2\ \mu\text{m} \times 2\ \mu\text{m}$  AFM images of Ge films and Ge:H films on  $\text{SiN}_x$ -coated glass at  $450^\circ\text{C}$ : (a) 3D image (Ge film), (b) 2D image (Ge film), (c) 3D image (Ge:H film), (d) 2D image (Ge:H film). It can be seen that the Ge:H film sputtered at  $450^\circ\text{C}$  exhibits a larger roughness feature size than the Ge film sputtered at the same temperature although both are polycrystalline and with similar RMS roughness. This

offers evidence that despite relatively low hydrogen residual in the film sputtered at  $T_s$  up to 450°C, hydrogen does influence the morphology of the film.

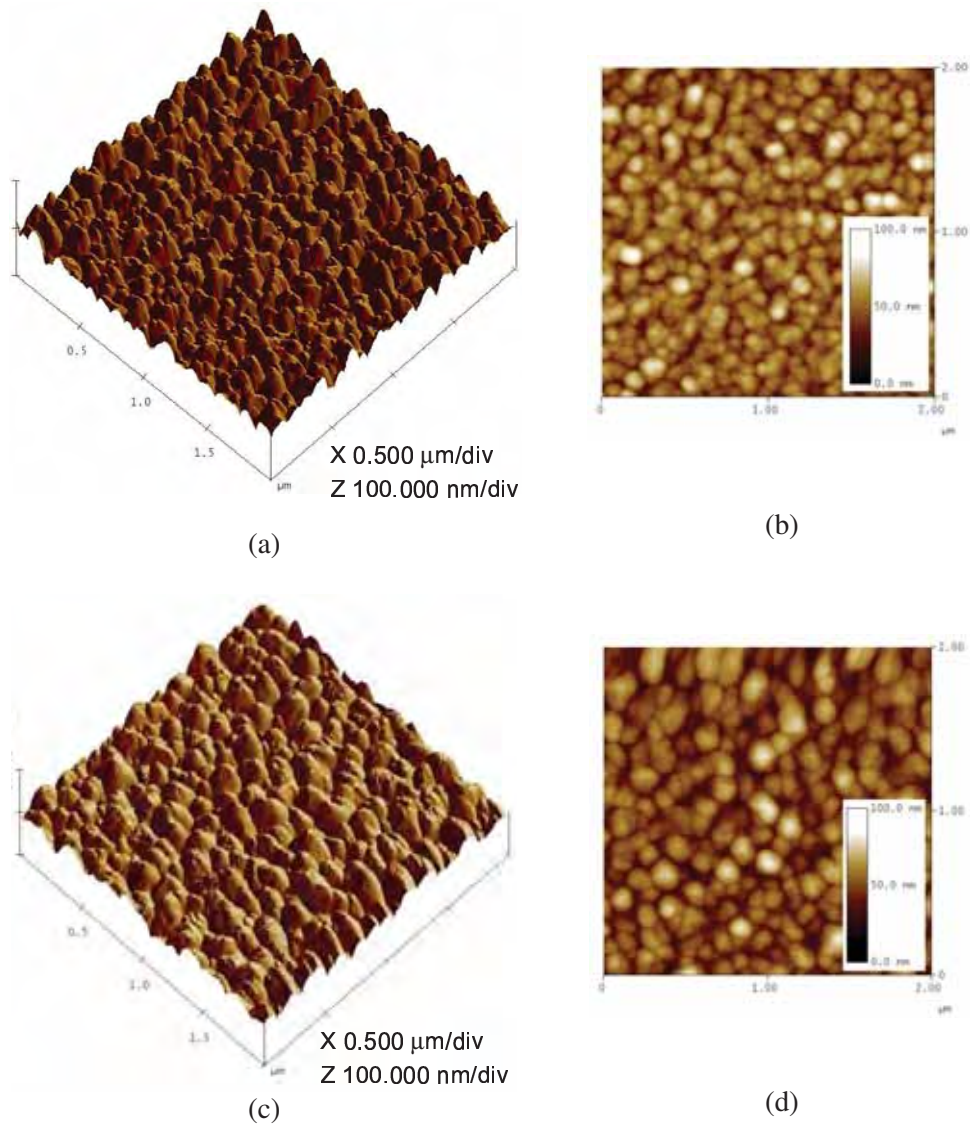


**Figure 3.7:** Typical AFM images ( $2\ \mu\text{m}\times 2\ \mu\text{m}$ ) of Ge films and Ge:H films on  $\text{SiN}_x$ -coated glass sputtered at various  $T_s$ : (a) 3D 450°C (Ge film), (b) 2D 450°C (Ge film), (c) 3D 450°C (Ge:H film), (d) 2D 450°C (Ge:H film).

### 3.4.3 Optical properties

- **Refractive index and extinction coefficient**

The influence of hydrogenation on the optical properties of the Ge films was firstly examined in terms of refractive index and extinction coefficient. Refractive index  $n$  and extinction coefficient  $k$  were obtained by analysing the spectroscopic ellipsometry (SE) measured data. The SE used polarized light to characterize Ge thin films by characterizing the reflection of polarized light with two measured parameters,  $\Delta$  and  $\psi$ , related to the ratio,  $\rho$ , of complex Fresnel reflection coefficients,  $R_p$  and  $R_s$ , for p- (in the plane of incidence) and s- (perpendicular to the plane of incidence) polarized light, respectively, as in the equation shown below (Hilfiker 2009).

$$\rho = \frac{R_p}{R_s} = \tan(\psi)e^{i\Delta} \quad (3.5)$$

As a result, SE offers one well known advantage over simple intensity-based reflection or transmission measurements. Measurement is defined by a ratio, thus SE is not sensitive to variations in absolute intensity of the measurement beam. The  $n$  and  $k$  values were subsequently determined by building a model describing the measured sample using layers for each material, followed by fitting with the measured parameters,  $\Delta$  and  $\psi$  (Hilfiker 2009). The general model is illustrated in Figure 3.8. Figure 3.9(a) and (b) demonstrate the worst case of the fitted results among the samples presented in this section, which is for Ge:H sputtered at 400 °C (Hilfiker 2009). As shown in the figure, the fitting is nevertheless very good, ensuring high reliability of the resultant  $n$  and  $k$  values.

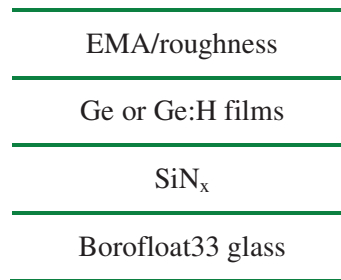
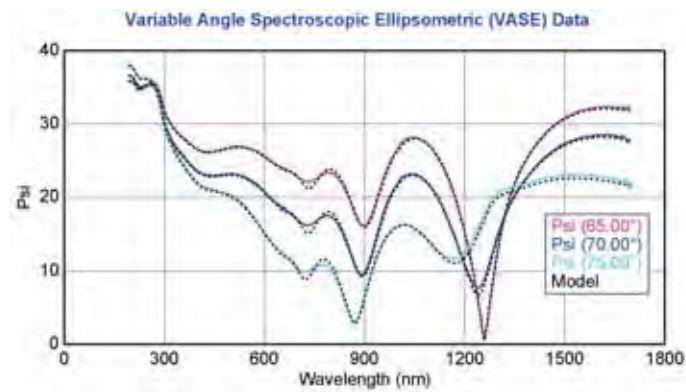
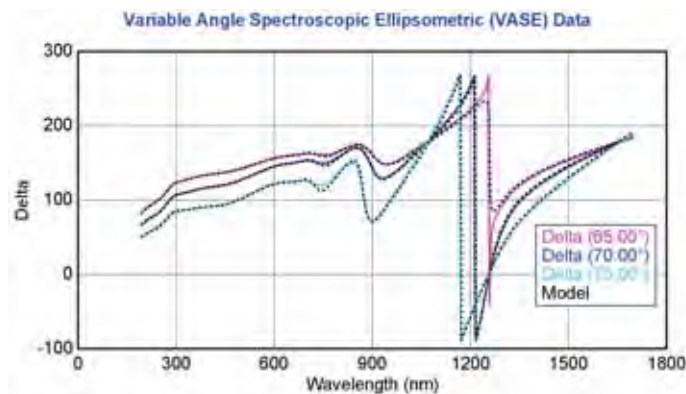


**Figure 3.8:** The general model used for fitting the optical properties of Ge films and Ge:H films.



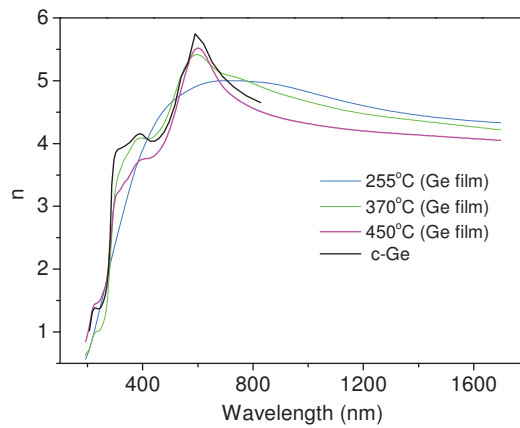
(a)



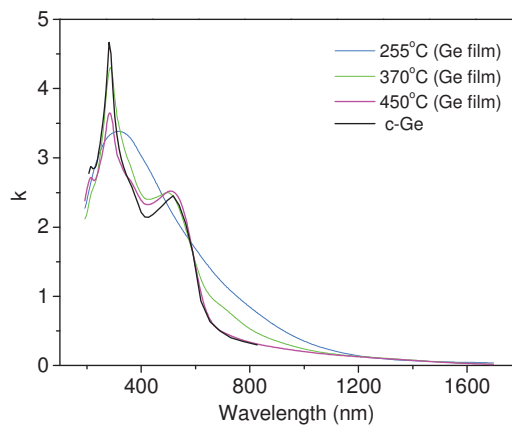
(b)

**Figure 3.9:** The worst case of the fitted results for the optical properties among all the samples presented in this section (Ge:H sputtered at 400°C): (a)  $\psi$  (b)  $\Delta$  from an internal Woollam report (Hilfiker 2009).

Figure 3.10 and 3.11 show dispersion in  $n$  and  $k$  of Ge films of Chapter 2 and Ge:H films over a variety of  $T_s$ , respectively. The data of the films sputtered at 280 °C and 370 °C, as well as 400 °C and 450 °C, are very close. For clarity, only three out of five spectra are shown accompanied with the reference  $n$  and  $k$  reported elsewhere (Aspnes and Studna 1983). It can be seen from the figure that the  $n$  and  $k$  values of both the Ge films and Ge:H films are, as expected, strongly dependent on  $T_s$  (more specifically, strongly dependent on the crystallinity of the films). The evolution of the  $n$  and  $k$  spectra are similar to those of polycrystalline silicon (Tompkins and McGahan 1999). By comparing Figure 3.10(a) and 3.11(a) as well as Figure 3.10(b) and 3.11(b), respectively, it is evident that the incorporation of hydrogen leads to  $n$  and  $k$  profiles closer to those of single crystalline germanium. This suggests that it has more ordered crystallites, consistent with the structural properties revealed by Raman and XRD measurements described above.

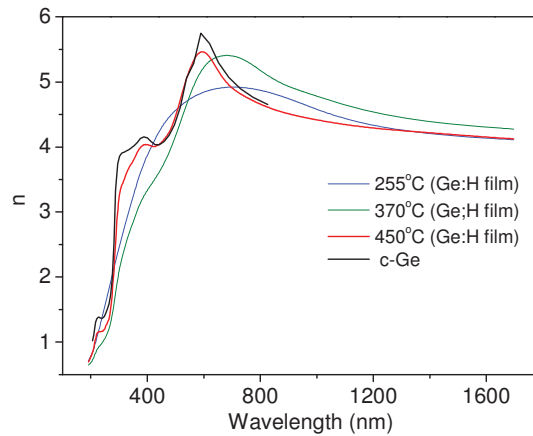


(a)

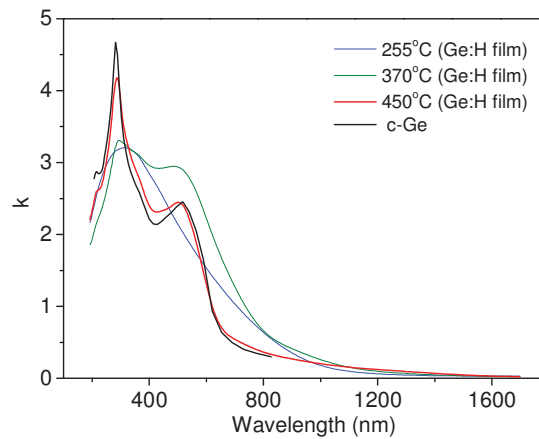


(b)

**Figure 3.10:** Refractive index  $n$  spectra and extinction coefficient  $k$  spectra of Ge films in Chapter 2 sputtered at various  $T_s$ : (a)  $n$  for Ge films (b)  $k$  for Ge films. The black solid line indicates the corresponding data for c-Ge (Aspnes and Studna 1983) for reference.



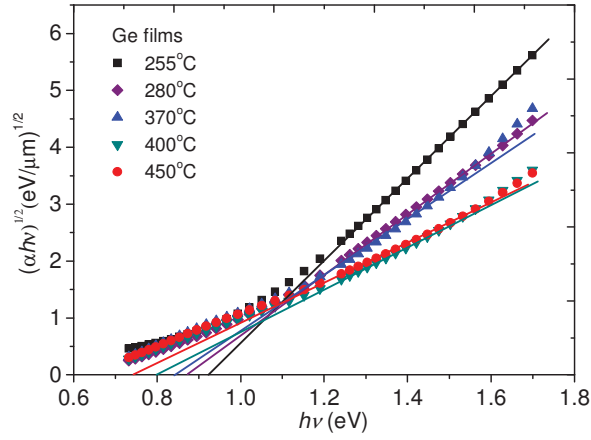
(a)



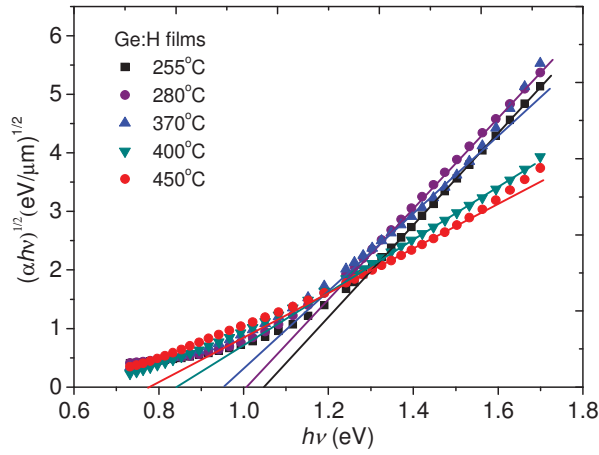
(b)

**Figure 3.11:** Refractive index  $n$  spectra and extinction coefficient  $k$  spectra of Ge:H films sputtered at various  $T_s$ : (a)  $n$  for Ge:H films (b)  $k$  for Ge:H films. The black solid line indicates the corresponding data for c-Ge (Aspnes and Studna 1983) for reference.

- **Band gap**



(a)



(b)

**Figure 3.12:** Tauc plot of  $(\alpha h\nu)^{1/2}$  versus photon energy  $h\nu$  of (a) Ge films and (b) Ge:H films sputtered at various  $T_s$  based on the  $\alpha$  values obtained from SE.

The influence of hydrogenation on the optical properties of the Ge films was then examined in terms of band gap. The band gap energy ( $E_g$ ) was determined by Tauc's equation (Pilione et al. 1987; Song et al. 2008), given as

$$(\alpha h\nu)^{\frac{1}{n}} = B(h\nu - E_g) \quad (3.6)$$

where  $\alpha = 4\pi k/\lambda$  is absorption coefficient,  $h\nu$  is the photon energy,  $B$  is the edge width parameter dependent on structural disorder of films, and the exponent  $n$  depends on the

type of transition. For a direct-allowed transition,  $n=1/2$ , for an indirect-allowed transition,  $n=2$ , and for a direct-forbidden transition,  $n=3/2$  (Banerjee and Chattopadhyay 2005). For Ge, known as an indirect semiconductor,  $n$  was chosen as 2. As noted previously, although this equation was originally developed and is most suitable for extracting the band gap for amorphous materials, it has been used to determine the band gap of nano-crystalline materials (Banerjee and Chattopadhyay 2005; Song et al. 2008) and poly-Ge films (Tripathi et al. 2006). Here it was used to estimate the band gap shift of the films.

Figure 3.12(a) and (b) show Tauc plots of  $(\alpha hv)^{1/2}$  versus photon energy  $hv$  of Ge films and Ge:H films sputtered at various  $T_s$ . The band gap  $E_g$  can be obtained by extrapolating the linear portion of the curve to the x-axis, i.e. at  $(\alpha hv)^{1/2} = 0$ . As demonstrated in the figures, there is a general trend for the band gaps to decrease with increasing  $T_s$  while the change from a knee shape curve (a-Ge) to a straight line (c-Ge) indicates the increase in crystallinity (Amutha et al. 2006). The band gaps of the hydrogenated films sputtered at 255°C and 280°C, both amorphous, are ~1.05 eV and ~1.01 eV, similar to those of a-Ge:H films prepared by RF magnetron sputtering at 300°C (Saito et al. 1995). These values are lower than state of the art RF sputtered a-Ge:H films (1.1 eV), deposited at 200°C (Chambouleyron 1993). Although it is hard to directly compare the results prepared by different sputtering systems as the sputtering machines employed will use components with different characteristics, it was demonstrated that for a-Ge:H films the band gaps were linearly dependent on the hydrogen content of the films (Drusedau and B 1994; Mulato et al. 1996). The hydrogen content may be altered by sputtering parameters, such as RF power or sputtering pressure (Saito et al. 1995), and, importantly, substrate temperature (Drusedau et al. 1994; Mulato et al. 1996). In the present case, the varied

parameter is substrate temperature, influencing not only the structure but also hydrogen content of the film. Therefore, the narrower band gaps of the a-Ge:H films compared to films described in (Chambouleyron 1993) might be due to the higher substrate temperatures applied to the samples.

With increasing  $T_s$ , the band gaps of both series of films gradually decrease. As shown in the figures, the Tauc plots are highly dependent on  $T_s$ , owing to the different degree of crystallinity (and different hydrogen content for Ge:H films). Both films sputtered at 450°C are polycrystalline, as concluded from XRD measurement results. Polycrystalline material can be described as comprising different homogenous components- intragrain, grain boundary and other regions where dangling bonds occur. This makes for a very limited portion of the Tauc plot from which to extrapolate.

**Table 3.1:** Summary of the estimated band gaps of the Ge films and Ge:H films obtained by Tauc plots as a function of  $T_s$ .

$E_g$ (eV) \ $T_s$	255°C	280°C	370°C	400°C	450°C
Ge films	0.92	0.88	0.85	0.80	0.75
Ge:H films	1.05	1.01	0.96	0.84	0.77

Table 3.1 summarizes the estimated band gaps of the Ge films and Ge:H films both obtained by Tauc plots as a function of  $T_s$ . Comparing the band gaps shown in the table, it is found that the introduction of hydrogen results in the increase of band gap for all Ge:H films. The wider band gaps of Ge:H films compared to those of Ge films may result from the substitution of Ge-Ge bonding and anti-bonding states by Ge:H states in the valence and conduction bands. It should be noted that as  $T_s$  increases, the difference in  $E_g$  due to

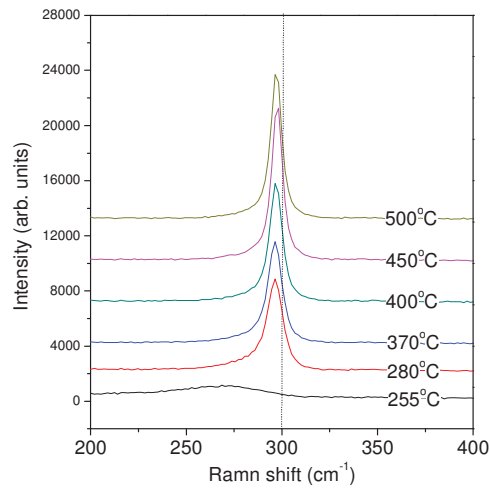
the presence or absence of hydrogen becomes less pronounced. This may be because with increasing  $T_s$  the amount of hydrogen bonded in the films reduces, as discussed earlier. As a result, the largest increase of band gap occurs in the films sputtered at 255° C and then descends with increasing  $T_s$ .

### 3.4.4 Structural dependence of electrical properties

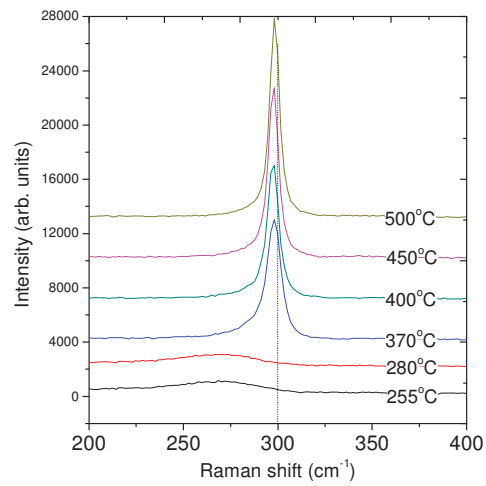
To elucidate the structural dependence of the electrical properties of films, the structural properties of the Ge and Ge:H films were re-visited. The Raman spectra shown in Figure 3.2(a), (b) are re-drawn in Figure 3.13 with additional information about the Ge films and Ge:H films sputtered at 500°C. The figure shows Raman spectra of (a) Ge films and (b) Ge:H films sputtered at various  $T_s$ . Figure 3.3 was also re-drawn in Figure 3.14 with additional information about the Ge films and Ge:H films sputtered at 500°C, depicting the Raman peak position of both series of films as a function of  $T_s$ . Dotted lines at 300  $\text{cm}^{-1}$  indicate the measured Raman peak position of a Ge wafer for reference. The presence of typical infrared absorption bands, measured by a PerkinElmer Spectrum 100 Spectrometer equipped with a universal attenuated total reflection accessory, shows the evidence of hydrogen incorporation in the Ge:H films, as discussed in Section 3.4.1. The figures reveal the structures of both series of films evolving from amorphous to crystalline phase. Also revealed by the figures is that the onset crystallization temperature of Ge:H films at 370°C is higher than that of Ge films at 280°C. The increase of onset crystallization  $T_s$  is similar to those observed elsewhere (Hoshi et al. 2005) and is very likely caused by a reduction of particle bombardment effects as previously discussed. This is because for sputter deposition, the adatom mobility and hence surface diffusion are mainly controlled by substrate temperature and energetic particle bombardment

(Thornton 1986). If processing pressure is fixed, the introduction of hydrogen gas will cause a decrease in bombardment of the film mainly by energetic neutral argon atoms. Consequently, the Ge:H films require a higher substrate temperature to achieve the surface mobility to crystallize. More detailed discussion by the author has been given elsewhere (Tsao et al. 2010a).

As shown, the results of both series of films clearly show a general trend that the peaks shift toward  $300\text{ cm}^{-1}$  with increasing  $T_s$  except the Ge film deposited at  $500^\circ\text{C}$ . The increase in  $T_s$  enhances the degree of crystallinity but also leads to a higher tensile strain of the films due to the larger linear thermal expansion coefficient of Ge ( $5.8 \times 10^{-6}\text{ K}^{-1}$ ) compared to that of Borofloat glass ( $3.25 \times 10^{-6}\text{ K}^{-1}$ ) (Song et al. 2006). By comparing the figures, it can be seen that despite a higher onset crystallization temperature required, the peaks of Ge:H films sputtered at the temperatures  $\geq 370^\circ\text{C}$  are sharper and closer to  $300\text{cm}^{-1}$  than those of Ge films, suggesting that the Ge:H films are of higher quality. The more red-shifted peaks of the Ge films illustrated in Figure 3.14 in contrast with their hydrogenated peers may be caused by both poorer crystallinity and tensile strain. The better crystal quality of Ge:H films is attributed to the removal of weak bonds and the passivation of dangling orbitals by hydrogen atoms (Chambouleyron 1993). In addition, the strain may be relaxed by the hydrogen (Dalba et al. 1997). It is noted that with further increase in  $T_s$  from  $450$  to  $500^\circ\text{C}$ , the peak of the Ge film does not further shift toward but away from  $300\text{ cm}^{-1}$ , suggesting the tensile strain caused by the high temperature becomes severe. In contrast, the Ge:H film deposited at  $500^\circ\text{C}$  does not apparently suffer from the tensile strain very likely because of the relaxation of the strain by the incorporated hydrogen (Dalba et al. 1997).



(a)



(b)

**Figure 3.13:** Raman spectra of (a) Ge films and (b) Ge:H films sputtered at various  $T_s$ . Dotted lines at  $300 \text{ cm}^{-1}$  indicate the measured Raman peak position of a Ge wafer for reference.

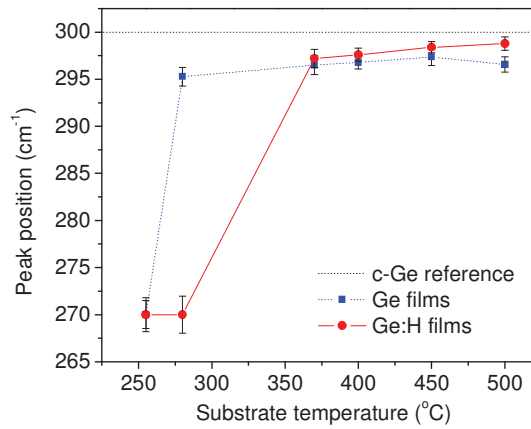


**Figure 3.14:** The Raman peak position of both series of films as a function of  $T_s$ . Dotted lines at  $300 \text{ cm}^{-1}$  indicate the measured Raman peak position of a Ge wafer for reference.

### ● XRD measurements

Similarly, the XRD spectra shown in Figure 3.4(a) and (b) were re-drawn in Figure 3.15 with additional information about the Ge films and Ge:H films sputtered at  $500^\circ\text{C}$ . XRD spectra in Figure 3.15(a) and (b) show the structure evolution of the Ge films and Ge:H films sputtered at various  $T_s$ . A hump at around  $2\theta = 22^\circ$  is attributed to the glass substrate. The diffraction peaks appearing at around  $2\theta = 27.3^\circ$ ,  $45.3^\circ$ , and  $53.7^\circ$ , correspond to the Ge {111}, {220}, and {311} crystal planes. By comparing Figure 3.15(a) and (b), it can be seen that the hydrogenated films have a higher onset crystallization temperature at  $370^\circ\text{C}$  than that of Ge:H films at  $280^\circ\text{C}$  in Ge films, consistent with the Raman data aforementioned. Also noted is that for both Ge and Ge:H films the diffraction peak of (111) orientation increases with temperature, but that of (220) orientation is rather irregular. Since the absolute values of peak intensities cannot be compared directly for different planes due to the thickness effect of the variation in the angle of incidence, the intensities were corrected using the ratio  $[I(111):I(220):I(311) = 100:57:39]$  based on the

reference pattern of Ge from PANalytical. The corrected intensities were plotted as a function of  $T_s$  in Figure 3.16(a) and (b). As shown, the films sputtered at  $T_s \leq 400^\circ\text{C}$  are either amorphous (having no characteristic XRD peaks) or preferentially (220) oriented while the films sputtered at  $T_s > 400^\circ\text{C}$  are preferentially (111) oriented. It is noted that there is a degradation of the peak intensity of (111) orientation of the Ge film deposited at  $500^\circ\text{C}$ , suggesting its lower degree of crystalline perfection and attribute this to the tensile strain.

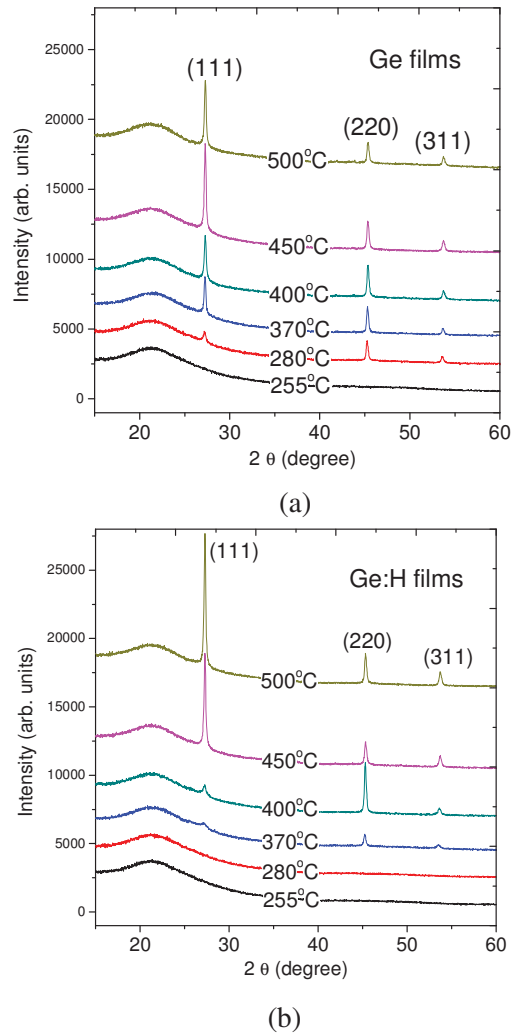
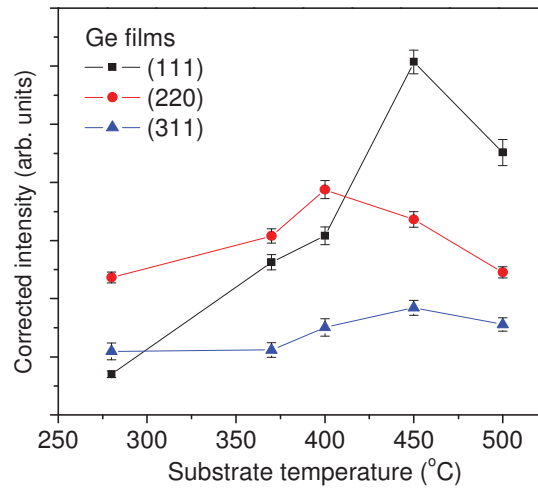
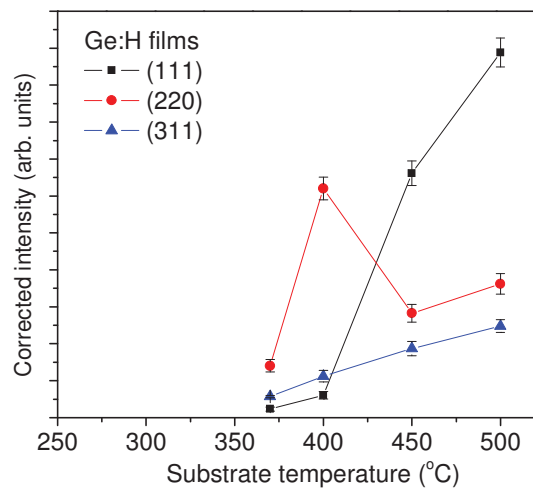


**Figure 3.15:** XRD spectra of (a) Ge films and (b) Ge:H films sputtered at various  $T_s$ . A hump at around  $2\theta = 22^\circ$  is attributed to the glass substrate.



(a)



(b)

**Figure 3.16:** Corrected intensities of the XRD characteristic peaks as a function of substrate temperature (a) Ge films (b) Ge:H films.

- **Electrical characterization**

The electrical properties of the Ge films were examined in terms of dark resistivity, concentration, mobility, and conduction type. Figure 3.17 shows the room temperature dark resistivity and the conduction type of the Ge films and Ge:H films as a function of  $T_s$ . The resistivity values were calculated from the sheet resistance obtained by the four-point probe technique. The trends of resistivity obtained by Hall measurement are similar despite a slight variation in the individual resistivity values (not shown here). The hydrogenation generally reduced the resistivity at all  $T_s$ , which may result from the passivation of near midgap localized states (Scheller et al. 2009). Initially the resistivity of the films in both series gradually increases with  $T_s$  up to 400°C, after which the resistivity decreases rapidly with further rise in  $T_s$ . Similar trends in Ge film resistivity have also been observed in relation to thermal annealing temperature (Chopra and Randhawa 1977) and laser irradiation power density (Srivastava et al. 1986) on evaporated films. The similarity of the trends in the resistivity of Ge films related to the thermal annealing temperature (Chopra and Randhawa 1977), laser irradiation power density (Srivastava et al. 1986), the aforementioned sputter input power (Sundaram and Garside 1984), and the substrate temperature in the present work suggests that the dark resistivity profiles of evaporated or sputtered Ge films are strongly dependent on the amount of energy applied to the films, either during deposition or after. As expected, hot-probe measurements show that the peak in the resistivity corresponds to a conduction type change, with the films being p-type for  $T_s > 400^\circ\text{C}$  and n-type for  $T_s \leq 400^\circ\text{C}$ .

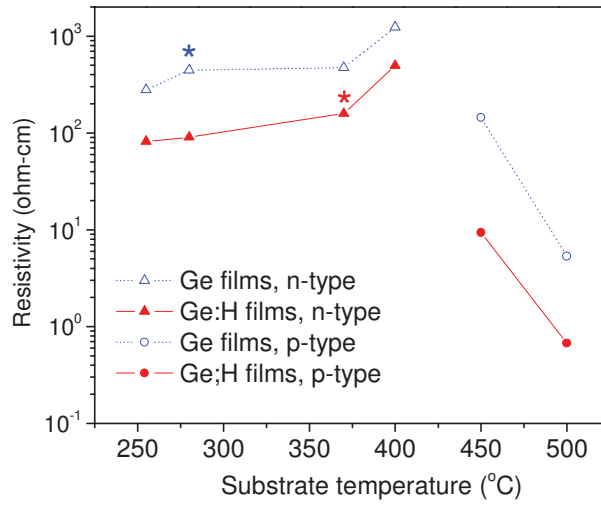
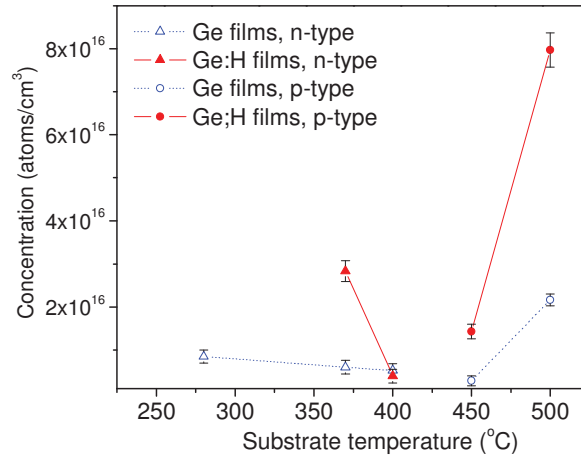


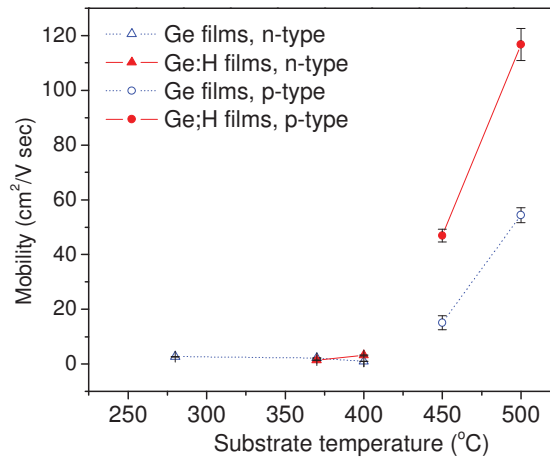
**Figure 3.17:** Variation of room temperature dark resistivity and conduction type of Ge films and Ge:H films on  $\text{SiN}_x$ -coated glass as a function of substrate temperature. The asterisks indicate the onset crystallization temperatures.

The conduction types were confirmed by Hall measurements except for the entirely amorphous films deposited at low temperatures, for which reliable results could not be obtained. The difficulty of identifying the conduction type of amorphous Ge (a-Ge) films by Hall measurements has been previously documented elsewhere (Kumru 1991; Saito et al. 1995), although Clark (Clark 1967) did report that evaporated a-Ge films as measured by Hall measurements were n-type and Giangregorio *et al.* (Giangregorio et al. 2006) proved that their plasma enhanced chemical vapor deposited a-Ge:H films were n-type by examining the rectification characteristics of a-Ge:H/(p-type)-crystalline silicon diodes. By comparing Figure 3.16(a) and (b) with Figure 3.17, it is interesting to note that the conduction type transitions of both Ge and Ge:H films are accompanied by a simultaneous change in the preferential film crystallographic orientations, namely from (220) to (111). This is not unusual amongst semiconductor thin films as the correlation between conduction type and preferential orientation in Si-doped GaAs and InSb have been reported before (Isai et al. 1991; Sakamoto et al. 1995). Below an explanation for the

correlation between the type switch and the preferential orientation change will be offered.



(a)



(b)

**Figure 3.18:** (a) The concentration and (b) mobility of Ge films and Ge:H films on SiN<sub>x</sub>-coated glass as a function of substrate temperature. The absence of the concentration and mobility data of the amorphous films, i.e. Ge film sputtered at 255 °C and Ge:H films sputtered at 255 and 280 °C, is due to the lack of reliable results from Hall measurements.

The n-type conduction of Ge films deposited at low  $T_s$  may be attributed to incorporated impurities such as oxygen or nitrogen (Schroder et al. 1993) despite the possibility of electron hopping among localized states. It has been reported that sputter-deposited undoped a-Ge:H exhibits strong n-type conductivity due to oxygen incorporation (Schroder et al. 1993). Although nitrogen in a-Ge films may act as an effective donor for Ge (Chambouleyron and Zanatta 1998; Schroder et al. 1993), oxygen arising from plasma-dissociated water vapor is generally the main culprit of unintentional n-type doping of sputter-deposited Ge films. The typical atomic percentage of oxygen incorporated in the presented Ge and Ge:H films was around 4-5% detected by X-ray photoelectron spectroscopy measurements. Such high oxygen content incorporated in the Ge films is due to the moisture introduced into the deposition chamber when the chamber is opened for changing targets. The targets need to be changed to a Ge target prior to the Ge film deposition as about 10 users, employing different targets, share the usage of the sputter system. The solution for reducing the incorporated oxygen will be discussed in the next chapter.

At the onset crystallization temperatures, both the Ge and Ge:H films undergo step increases in resistivity, while remaining n-type. This resistivity increase might be due to the formation of isolated p-type crystalline grains which act to reduce the volume of the continuous n-type a-Ge network. The transition temperature marks the threshold where the crystalline grains form a percolating network, thus rendering the film p-type. In this model, the conduction pathway for the n-type films is a-Ge material, and that for the p-type films is polycrystalline material, consistent with Figure 3.18(b) where the mobilities of p-type films are more than an order of magnitude higher than those of the n-type films. Also, about the transition temperature, the films evolve from (220)

preferential orientation to (111), which is characteristic of a transition from microcrystalline to polycrystalline structure (Tsao et al. 2009) whereupon percolation of the crystalline grains become much more probable. Beyond the transition temperature, the film resistivities decrease rapidly due to the rise in both carrier concentration and mobility, as shown in Figure 3.18. This suggests that trapped carrier density decreases and the grain boundary barrier height reduces, indicating that the film material quality improves with higher  $T_s$ .

### 3.5 Summary

Structural, morphology, optical, and electrical properties of hydrogenated Ge thin films sputtered on SiNx coated glass at various substrate temperatures have been investigated. The structural evolution of the *in situ* deposited hydrogenated Ge films characterized by Raman and XRD measurements are in good agreement. The inclusion of hydrogen leads to an increase of the substrate temperature required to achieve crystalline Ge prepared by RF magnetron sputtering, owing to a resultant reduction of energetic particle bombardment effects. Despite the higher onset crystallization temperature required, the introduction of hydrogen reduces the tensile strain. In addition, it leads to higher degree of crystalline perfection of the poly-Ge:H film sputtered at temperature  $\geq 450^\circ\text{C}$  compared to its non-hydrogenated counterpart. In addition, it also results in a different surface morphology. Moreover, the hydrogen incorporated in the films leads to broadened band gaps of the films sputtered at different  $T_s$ . Furthermore, it was found, as expected, that the hydrogenation resulted in a reduction of the resistivity, an increase of concentration as well as mobility of the films deposited at all  $T_s$ . Finally, this work

demonstrated the sputtered Ge and Ge:H films a dependence of conduction type on the films' deposition temperature, and that the type switch was accompanied by a change from (220) to (111) preferential orientation. The resistivity change of the sputtered films is strongly dependent on their degree of crystallinity attributed to the percolation effects of the crystalline grains. The n-type films exhibit extremely low mobility associated with the amorphous conduction pathway and the p-type films exhibit high mobility as the film material quality improves. Two papers arising from this chapter have been published in *Journal of Crystal Growth* (Tsao et al. 2010a) and *Applied Physics A* (Tsao et al. 2011c).

## CHAPTER

# 4

## Controlled doping of Poly-Ge Thin Films

---

- *Overview*
- *Literature review*
- *Experiment*
- *Results and discussion*
- *Summary*

### 4.1 Overview

Chapter 3 has elucidated the improvement of the properties of poly-Ge films by *in situ* hydrogenation, enhancing the potential of poly-Ge:H thin films on glass in the application of the bottom cells of low-cost monolithic tandem solar cells. Like other p-n junction based devices, the performances of these bottom cells rely on well-controlled doping. This chapter focuses on the development of p-type and n-type doping techniques of poly-Ge:H films sputter-deposited on glass. Section 4.2 gives a literature review about doping techniques for sputter-deposited films. Section 4.3 provides the experimental

details. P-type films were deposited and *in situ* doped by co-sputtering Ge:H with B at various power levels ( $P_B$ ) in a mixture of argon and hydrogen at 500°C, and then followed by a rapid thermal anneal process (RTA). On the other hand, n-type films were fabricated by firstly sputter-depositing a Ge:H layer and then capping with SiO<sub>2</sub>/(P<sub>2</sub>O<sub>5</sub>+SiO<sub>2</sub>)/SiO<sub>2</sub>/SiN<sub>x</sub> multi-layers, and finally a thermal drive-in process with RTA. Section 4.4 gives the results and discussion. The properties of boron-doped (B-doped) and phosphorus-doped (P-doped) poly-Ge:H films sputter-deposited on glass are investigated. Evidence for successfully controlled p-type and n-type doping of poly-Ge:H films sputter-deposited on glass will be presented. Section 4.5 summarizes the findings.

## 4.2 Literature review

In recent years, a number of researches (Chao et al. 2005; Chui et al. 2003a; Hutin et al. 2008; Simoen et al. 2008) have achieved high activation level p-type doping of Ge wafers implanted with B. However, ion implantation would not be applicable in the doping of large area monolithic thin films due to its relatively high cost. In addition, implantation generally results in undesired concentration profiles of Gaussian distribution with diffusion tails. Other *ex situ* doping techniques, such as furnace thermal diffusion (FTD) and spin-on-dopant (SOD), are very challenging or nearly impossible in this application since B atoms hardly diffuse in Ge below 800°C (Hutin et al. 2008). For instance, Uppal *et al.* (Uppal et al. 2001) reported that with a calculated diffusion coefficient of  $1.5(\pm 0.3) \times 10^{-16}$  cm<sup>2</sup>/s B barely diffused into Ge even after being annealed at 850°C for 24 hours.

This diffusion characteristic of B in Ge leads to several difficulties in the doping of Ge thin films. Firstly, long period thermal processes at such high temperature ( $>800^{\circ}\text{C}$ ) are incompatible with low cost substrates such as glass with low softening point. Secondly, Ge loss due to the high temperature is another concern (Chroneos 2009; Ioannou et al. 2008). Unlike  $\text{SiO}_2$ , thermally grown  $\text{GeO}_2$  can not protect underlying Ge so that the Ge would be lost in high temperature processes without appropriate protection. The loss of Ge films may stem from the sublimation of GeO, formed by the solid phase reaction between Ge and  $\text{GeO}_2$  films at above  $450^{\circ}\text{C}$  (Tsao et al. 2009). Thirdly, the low gradient concentration profile commonly resulting from thermal diffusion is also a drawback. Therefore, to develop an *in situ* B doping approach meeting the requirements for large area monolithic thin film solar cells on glass is essential. In present work chemical vapour deposition techniques are excluded to avoid the use of very expensive and extremely toxic germane gas while co-sputtering is employed as it is an environment friendly, economical, and simple deposition technique. One of the advantages of co-sputtering is that the B is *in situ* incorporated so that only dopant activation but no extra diffusion process is necessary. The required activation temperature is expected to be considerably lower than the diffusion temperature ( $>800^{\circ}\text{C}$ ). Satta *et al.* (Satta et al. 2005a) successfully activated ion-implanted B in c-Ge and preamorphized Ge by employing RTA in the range of  $400\text{-}600^{\circ}\text{C}$  while activation of ion-implanted B in c-Ge could occur during the implantation process even without annealing (Simoen et al. 2006).

On the other hand, the n-type doping of sputter-deposited Ge thin films is much more challenging. For instance, the two references in Chapter 3 (Beensh-Marchwicka et al. 2001; Sundaram and Garside 1984) indicated the difficulty of n-type doping of

sputter-deposited Ge films. Although P is an excellent n-type dopant for Ge because of the high maximum solubility (Claeys and Simoen 2007), there are very few literature reports of the success of *in situ* P doping of Ge thin films by sputtering except Paul et al. (Paul et al. 1976), where the working gas consists of phosphine (PH<sub>3</sub>) gas in argon (Ar) with hydrogen (H<sub>2</sub>). PH<sub>3</sub> in hydrogen was also employed for *in situ* n-type doping of a-SiGe films by sputtering (Banerjee et al. 1988). Unfortunately, the sputter system used by the author had not been modified for using PH<sub>3</sub> gas during the course of this thesis, due to its extreme toxicity. The co-sputtering technique developed by the author for B doping is not applicable for P doping because no pure P target exists due to its high reactivity. Therefore, here the focus is shifted to *ex situ* P doping approaches.

It is known that n-type doping of poly-Ge films is challenging due to the inherent strong p-type characteristic, associated with crystallographic defects (Kobayashi et al. 1997; Sundaram and Garside 1984). Recently research has reported n-type doped c-Ge by implantation of P (Chui et al. 2003; Satta et al. 2005b; Simoen and Vanhellefont 2009). Unlike B, nevertheless, implantation of P in Ge may lead to much more pronounced damage, owing to the heavier mass of P (Simoen et al. 2006). It has been reported that implantation of P with practical dose level may result in formation of a p-type amorphized top layer of Ge, and thus requires an annealing process to remove the damage (Benourhazi and Ponpon 1992; Simoen et al. 2006). In addition, as previously mentioned, ion implantation would not be applicable in the doping of the large area thin films due to its relatively high cost. Another P doping approach, spin-on-dopant (SOD), has been used to realize an n-type shallow emitter on a c-Ge wafer by a research group devoting to developing thermal photovoltaics (Posthuma et al. 2007). However, Ge loss resulting from the high drive-in temperature is a concern (Chroneos 2009; Ioannou et al. 2008). As

discussed earlier, thermally grown  $\text{GeO}_2$  could not protect underlying Ge so that without appropriate protection Ge will be lost in high temperature annealing processes. Moreover, the non-optimal concentration profiles commonly resulting from thermal diffusion are another drawback. As a result, conventional thermal diffusion is apparently not applicable. Similarly, the required high thermal budget results in the difficulty of employing SOD on Ge thin films as the films need to be well protected by a cap layer to prevent Ge loss. To minimise the potentially introduced oxygen during the drive-in processes, the author has tried to drive-in the baked SOD into Ge films by annealing at  $600^\circ\text{C}$  for 60 seconds in a rapid thermal annealing (RTA) process, a tube furnace, and even by vacuum annealing in a sputter chamber but all failed because of the Ge loss.

In contrast, the SPC experiments discussed in Chapter 2 show that merely a  $\sim 50\text{-nm}$ -thick  $\text{SiO}_2$  cap layer can successfully prevent the loss of Ge films during the heating process at  $600^\circ\text{C}$  for 20 hours. These results imply that an intact cap layer of  $\text{SiO}_2$  or similar is essential to protect Ge when subjected to a thermal process. It would be possible to obtain P-doped Ge films by an *ex situ* doping approach if the Ge film is well capped with a  $\text{SiO}_2$  layer. It is known that annealed at a certain temperature, a thin layer of  $\text{P}_2\text{O}_5$  may provide elemental phosphorus for the diffusion into its underlying silicon via the reaction:



As  $\text{P}_2\text{O}_5$  targets were available for the sputter system employed in this work, this reaction stimulated an idea, which will be discussed later, to use  $\text{P}_2\text{O}_5$  as an n-type doping source.

## 4.3 Experiment

### 4.3.1 Boron-doping of poly-Ge:H thin films

*In situ* p-type doping of poly-Ge:H thin films was carried out by co-sputtering of Ge with B by RF magnetron sputtering in Ar and hydrogen H<sub>2</sub> plasma with an AJA ATC2200 sputter system. The typical base pressure of the sputter system was less than  $6.5 \times 10^{-7}$  Torr (by means of deliberately cyclically baking out the vacuum chamber at 550 °C for 6 hours to get rid of the chamber moisture introduced during the period the chamber is open for changing targets). The Ar flow was kept at 15 sccm while the addition of H<sub>2</sub> at 10 sccm. The deposition pressure was maintained at 1.5 mTorr. Please note that although the Ar and H<sub>2</sub> flows were the same as those used in Chapter 3, the pressure could not be reduced to 1 mTorr for the present work since a baffle shielding the turbo pump from sputtered material was installed and thus the pressure in the chamber could not be pumped down as effectively. The installation of the baffle was intended to prevent the crash of the pump attributed to sputtered material, especially silicon, entering the pump bearings and damaging them. ~300 nm thick Ge:H films were sputtered on SiN<sub>x</sub> coated glass substrates from a 2 inch intrinsic Ge target supplied by AJA International with a purity of 99.999% with 120 W RF power at a fixed substrate temperature ( $T_s$ ) of 500 °C. The amount of incorporated B was controlled by varying the input power ( $P_B$ ) from 0, 15, 23, to 55 W for sputtering from a 2 inch B target. A ~40 nm SiO<sub>2</sub> cap layer was *in situ* sputtered onto each Ge:H film for preventing Ge loss (Tsao et al. 2009) and B depletion caused by B-nitride formation on the film surface (Makino and Nakamura 1981) in a subsequent thermal annealing process in nitrogen atmosphere. To investigate the effect of thermal annealing on the properties of films, in addition to the as-sputtered films, films cut from the same samples were also subjected to a rapid thermal annealing (RTA) at 550 °C for 120 seconds or 600 °C for 60 seconds. The cap layers were removed by HF dipping prior to various measurements.

It is known that a high level of oxygen can be incorporated into sputtered films, just from the residual gas in the vacuum chamber (Jelenkovic et al. 2000). Oxygen has been found to reduce adatom mobilities and hence impact the structural properties of sputtered Ge films (Thornton 1986). In addition, oxygen contamination may also affect the electrical properties of sputtered Ge films (Schröder et al. 1993). To determine the oxygen and B content of the films, X-ray photoelectron spectroscopy (XPS) measurements were performed using a Fisons ESCALAB 220i-XL with a monochromatic AlK $\alpha$  (1486.5 eV) x-ray source and a hemispherical energy analyzer. To explore the effect of B incorporation on the structural properties of the films, Raman and X-ray diffraction (XRD) measurements were carried out.

Raman spectra of the samples were measured at room temperature (RT) with a Renishaw inVia Raman Microscope in backscattering configuration, using an Ar<sup>+</sup> laser with wavelength of 514.5 nm as the excitation source. XRD measurements were performed (PANalytical's X'Pert Pro materials research diffraction system) at a voltage of 45 kV and a current of 40 mA, using Cu K $\alpha$  radiation ( $\lambda = 1.5418 \text{ \AA}$ ). TEM was performed to confirm the crystallinity of grown Ge thin films by Philips CM200 operated at 200 kV with cross-section samples prepared by Focussed Ion Beam. Electrical properties including conduction type, resistivity, mobility, and concentration were examined by Hall measurements with the Van der Pauw method at RT. Van der Pauw patterns were formed by laser scribing with ohmic contact enhanced by GaAl alloy. All the contacts were then checked to ensure that they were ohmic prior to the Hall measurements. A typical result of contact checking for Ge:H films measured in the lab at UNSW is shown in Figure 4.1, where a linear relationship of applied current and the resultant voltage indicates the contacts are ohmic.

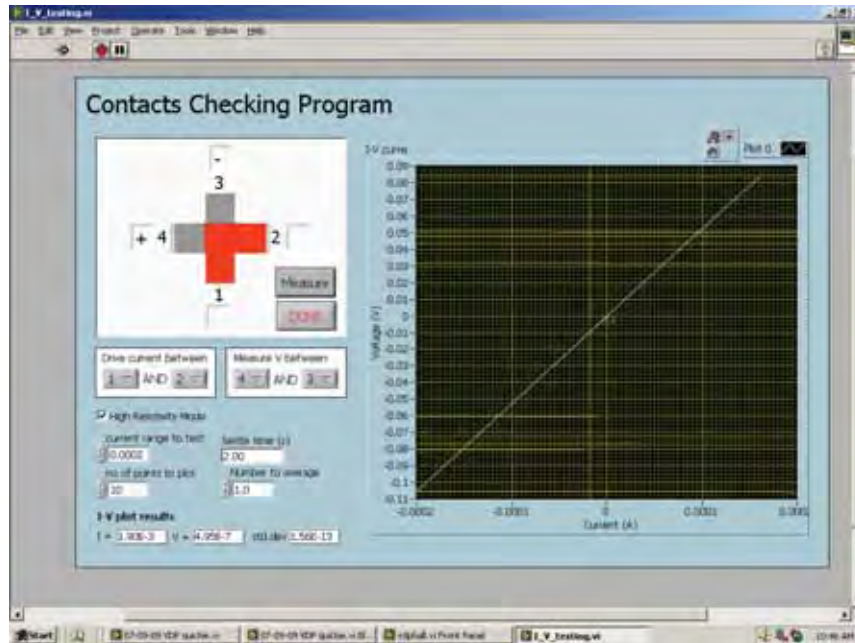


Figure 4.1: A typical result of a contact check for Ge:H films

### 4.3.2 Phosphorous-doping of poly-Ge:H thin films

*Ex situ* n-type doping of poly-Ge:H thin films was carried out by firstly sputtering of 500 nm thick Ge:H films on  $\text{SiN}_x$  coated glass in a mixture of Ar and  $\text{H}_2$ , subsequently *in situ* capping  $\text{SiO}_2/(\text{P}_2\text{O}_5+\text{SiO}_2)/\text{SiO}_2/\text{SiN}_x$  multi-layers in Ar by RF magnetron sputtering with an AJA ATC2200 sputter system, followed by a RTA process. Figure 4.2 depicts the structure of sputter-deposited films. The 2 nm thick  $\text{SiO}_2$  was used as a buffer layer. This layer is thin enough to allow the P to diffuse into the underlying Ge:H layer but prevents the direct reaction of the co-sputtered mixture of  $\text{P}_2\text{O}_5$  and  $\text{SiO}_2$  with the underlying Ge:H layer during the post RTA process and simplifies the lift-off of the multi-layers by HF dip. The 20 nm  $\text{SiN}_x$  layer was used to prevent the loss of phosphorus dopants since  $\text{SiN}_x$  material may be denser than  $\text{SiO}_2$  and does not allow P to out diffuse (Chroneos 2009).

Therefore, this SiN<sub>x</sub> layer forces the resultant elemental phosphorus to diffuse towards the Ge:H layer and makes the doping more effective.

The typical base pressure of the sputter system was less than  $6.5 \times 10^{-7}$  Torr by means of deliberately baking out. The Ar flow was kept at 15 sccm with the addition of H<sub>2</sub> at 10 sccm. The deposition pressure was maintained at 1 mTorr. Please note that in this case the pressure was able to reach 1 mTorr because the baffle shielding the turbo pump had been removed and thus the pressure in the chamber could be pumped down effectively. The Ge:H films were sputtered on SiN<sub>x</sub> coated glass substrates from a 4 inch intrinsic Ge target supplied by AJA International with a purity of 99.999% with a 150 W RF power at a fixed substrate temperature ( $T_s$ ) of 500 °C. The subsequent multi-layers were all *in situ* sputtered in Ar at 200°C.

To investigate the effect of thermal annealing on the P doping of the Ge:H films, in addition to the as-sputtered films, films cut from the same samples were also subjected to different RTA processes with different temperature profiles, including 800°C for 20s, 700°C for 60s, 650°C for 180s. The cap multi-layers were removed by HF dip prior to various measurements. To explore the influence of the RTA on the structural properties of the films, XRD measurements were carried out. The details of XRD measurements are the same as documented in Section 4.3.1. Similar to the case of B-doped films, the conduction types of the films were identified by hot-probe measurements and further confirmed by Hall measurements, which was also utilised to examine the dark resistivity, mobility, and electrical concentration of the films. To determine the depth profile of resistivity of the films, a combination of four-point-probe technique, hot-probe technique, and a layer removal method (Widenborg and Aberle 2007) was employed since all of

them are simple, fast, inexpensive and readily available in the author's lab. The layer removal method utilised plasma etching in a conventional 13.56MHz parallel-plate PECVD system with sulphur hexafluoride ( $\text{SF}_6$ ) as etching gas. The  $\text{SF}_6$  gas pressure was 350mTorr and the RF power  $\sim 0.17\text{W}/\text{cm}^2$ , resulting in a Ge removal rate of around 100 nm/min.

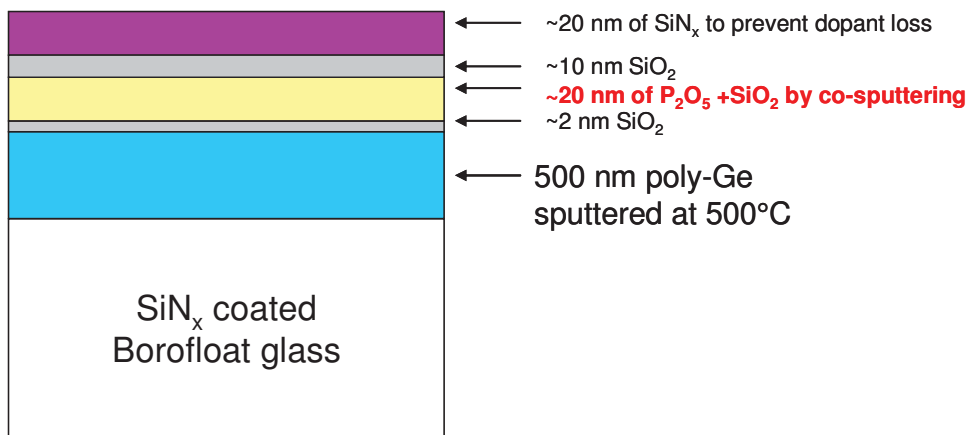


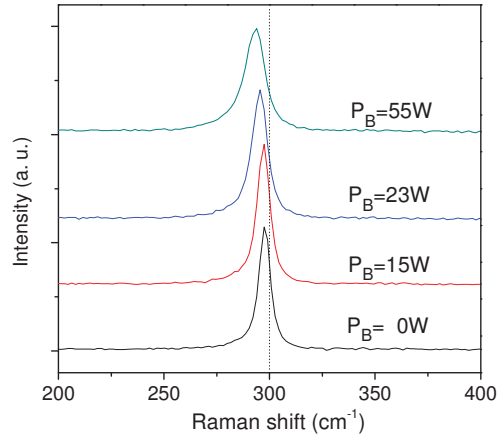
**Figure 4.2:** The structure of the Ge:H films with *in situ* capped multi-layers designed in this work for *ex situ* phosphorus doping by RTA.

## 4.4 Results and discussion

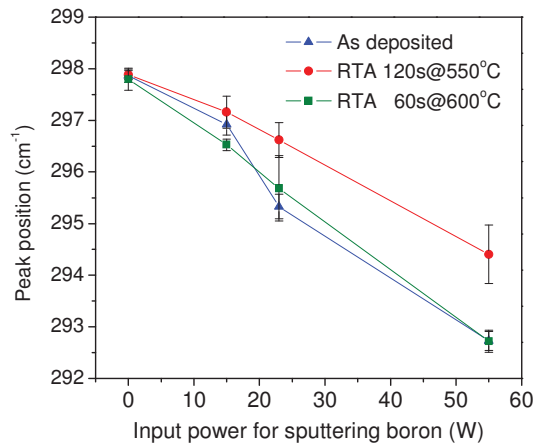
### 4.4.1 Boron-doping of Poly-Ge Thin-Films

XPS measurements revealed no detectable level of oxygen throughout the films, ensuring that the influence of oxygen on the properties of the films is insignificant. The amount of B incorporation at  $P_B = 55$  W detected by XPS was 0.66 at.% while those for  $P_B = 23$  or 15 W are difficult to detect. This is because boron has very low relative sensitivity factor, which makes it difficult to detect by XPS.

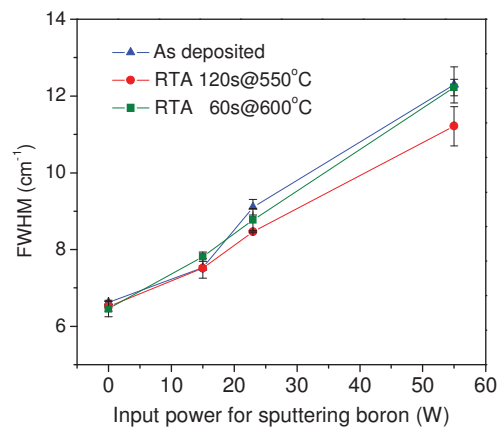
- Structural properties
- Raman measurements



(a)



(b)



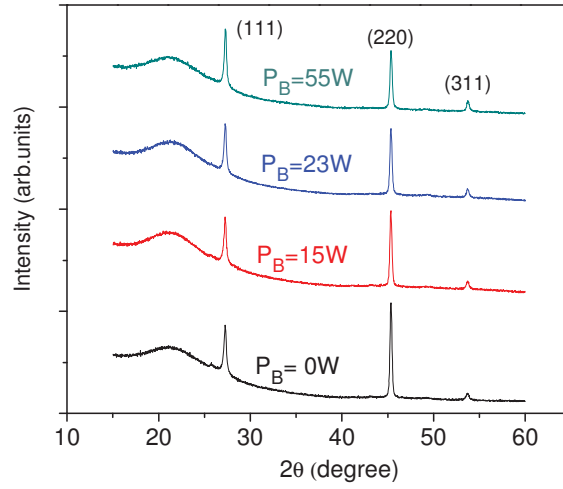
(c)

**Figure 4.3:** (a) Comparison of the Raman spectra of Ge:H films as deposited at 500°C at various power levels ( $P_B$ ) applied to the boron target. (b) Peak locations and (c) FWHM values of as deposited, 550°C, and 600°C annealed films as a function of power level ( $P_B$ ) applied to the boron target.

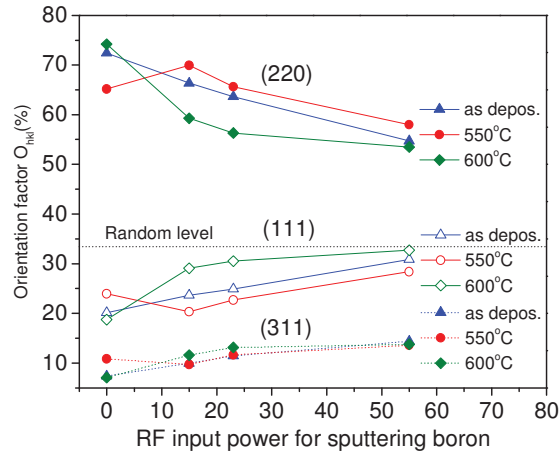
The influence of varying  $P_B$  on the structural properties is revealed by Raman measurements. Figure 4.3(a) shows the Raman spectra of the Ge:H films as deposited at 500°C at various values of  $P_B$ . The dotted lines at 300  $\text{cm}^{-1}$  indicate the Raman peak position of c-Ge for reference. As shown, the peak positions of Ge:H films shift away from 300  $\text{cm}^{-1}$  and FWHM values increase with increasing  $P_B$ . The red-shift and the broadening of the peaks suggest that the B incorporation degrades the crystallinity of the Ge:H films. This is similar to that observed elsewhere (Lin et al. 1994 ), where poly-Si films were *in situ* heavily doped with B.

To examine the effect of anneal processes on the crystallinity of the films, the corresponding peak locations and FWHM values of the films, as deposited, annealed at 550°C and 600°C, as a function of  $P_B$  are shown in Figure 4.3(b) and (c), respectively. The fact that RTA at 550°C for 120 s results in a blue-shift and the narrowing of the peaks of doped Ge films suggests that this RTA process improves crystallinity. On the other hand, the RTA at 600°C for 60 s does not improve the crystallinity of the doped films.

- XRD measurements



(a)



(b)

**Figure 4.4:** (a) Comparison of the XRD spectra of Ge:H films as deposited at 500°C with various power levels ( $P_B$ ) (b) Calculated orientation factors of as deposited, 550°C, and 600°C annealed films as a function of power level ( $P_B$ ) applied to the boron target.

The influence of varying  $P_B$  on the structural properties is revealed by XRD measurements as well. Figure 4.4(a) compares the XRD spectra of Ge:H films as deposited at 500°C at various values of  $P_B$ . A hump at around  $2\theta = 22^\circ$  is attributed to the glass substrate. The diffraction peaks appearing at around  $2\theta = 27.3^\circ$ ,  $45.3^\circ$ , and  $53.7^\circ$ , correspond to the Ge (111), (220), and (311) crystal planes. The intensity of the

characteristic peaks shown in Figure 4.4(a) follows the expected intensity ratio ( $I_{111}:I_{220}:I_{311}=100:57:39$ ) indicating all the films are of strong (220) preferential orientation. The variation among the peak intensities of (111) orientation of the films is minor. In contrast, the gradually degraded intensities and increased FWHM of (220) peak apparently with increasing  $P_B$  is observed. The observation suggests that the incorporated B significantly retards the grain growth of the as-deposited films. This is again similar to that observed elsewhere (Lin et al. 1994), where higher level B incorporation led to smaller grain sizes of poly-Si films *in situ* doped with B. It is noted that here the undoped Ge:H film is of strong (220) preferential orientation while Figure 3.9 shows Ge:H as deposited at the same temperature is of strong (110) preferential orientation. According to the Thornton's structural zone model for sputtered films of metals documented in Chapter 1, this may be attributed to the effect of the higher deposition pressure of 1.5 mTorr, owing to the installation of the baffle aforementioned in the present case. In other words, it would be possible to obtain films of strong (220) preferential orientation at a significantly lower temperature, say  $\sim 400^\circ\text{C}$ , or to obtain films of strong (111) preferential orientation at the current temperature if the deposition pressure can be reduced to 1 mTorr. The latter case is confirmed later in Figure 4.6 where the XRD spectrum of a Ge:H film as deposited at  $500^\circ\text{C}$  at 1mTorr pressure exhibits strong (111) preferential orientation.

To explore the effect of anneal processes on the crystallographic orientation of the films, by comparing the intensities of XRD diffraction peaks of as deposited,  $550^\circ\text{C}$ , and  $600^\circ\text{C}$  annealed films with those obtained on a randomly oriented standard powder, the orientation factors  $O_{hkl}$  are calculated as follows (Joubert et al. 1987):

$$O_{hkl} = 100 \times \frac{\frac{I_{hkl}}{I_{0hkl}}}{\sum_{hkl} \frac{I_{hkl}}{I_{0hkl}}} \quad (4.2)$$

where, for each diffraction plane,  $I_{0hkl}$  is the intensity measured on a randomly oriented Ge standard power and  $I_{hkl}$  is the measured intensity. The samples have randomly oriented grains when the three orientation factors are close to 33 % as our calculation only takes account of the three major diffraction peaks (i.e., (111), (220), and (311)) (Song et al. 2006). As shown in Figure 4.4(b), the orientation factor  $O_{220}$  of our Ge films has a value of about 55–75 % for all investigated films. The other two important orientations,  $O_{111}$  and  $O_{311}$ , have values in the range below 33 % and 15 %, respectively. It is noted that RTA at 550°C for 120 s leads to an enhancement of orientation factor  $O_{220}$  at the expense of a degradation of  $O_{111}$  except for the undoped films. In contrast, RTA at 600°C for 60 s, inversely, results in an enhancement of orientation factor  $O_{111}$  at the expense of a degradation of  $O_{220}$  except for the undoped films. As grains with (220) orientation dominate in the films, the enhanced orientation factor  $O_{220}$  suggests improved grain homogeneity, i.e. more ordered structure.

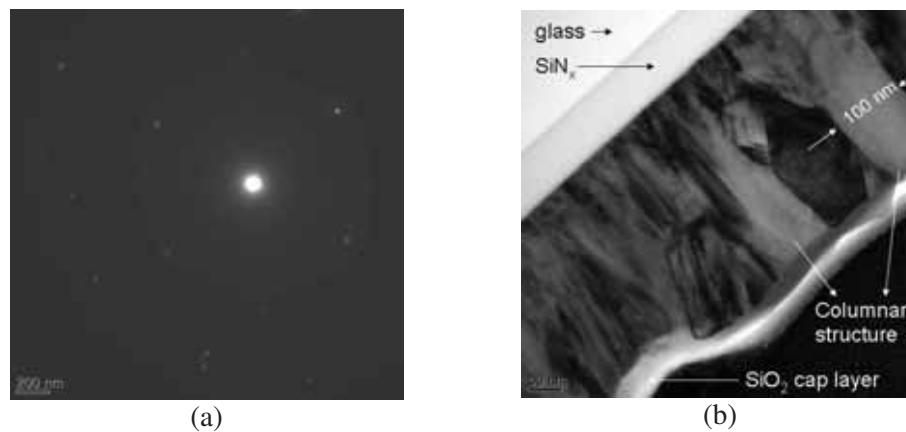


**Figure 4.5:** Cross-sectional TEM micrographs of a 300 nm thick Ge film deposited at 500°C: (a) Diffraction pattern at [011] beam direction (b) Bright field image

It is well known that silicon films with (220) preferential orientations have a columnar structure, beneficial to the carrier transport along the direction perpendicular to the plane of the film (Matsui et al. 2002), and hence could yield excellent photovoltaic performance. We expect the structures of our Ge:H films, which have been shown to be of (220) preferential orientation, will also have a columnar structure. To confirm this point, TEM measurement was performed. Figure 4.5 shows a diffraction pattern at [011] beam direction and a cross-sectional bright-field TEM image of the as-deposited, un-doped film. The diffraction pattern indicates the film is well crystallized. The film structure is identified as being columnar directly from the substrate interface with grain sizes of ~100 nm.

- Electrical properties

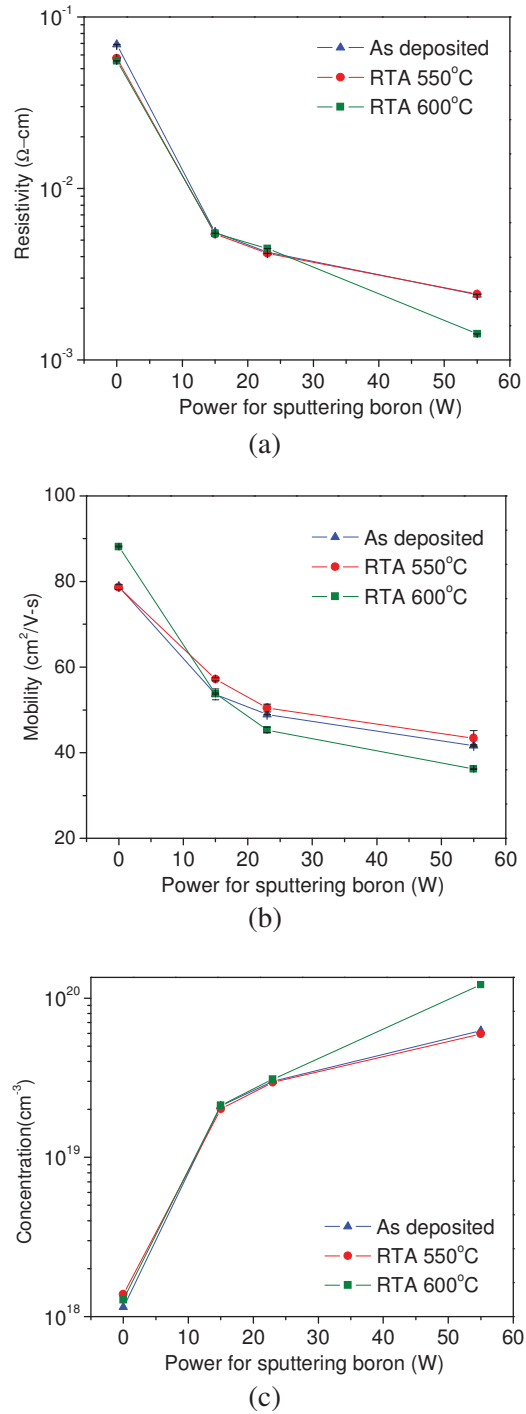


**Figure 4.6:** Variation of (a) room temperature dark resistivity, (b) mobility, and (c) concentration of as deposited and annealed Ge:H films on  $\text{SiN}_x$ -coated glass as a function of input power for sputtering boron.

Varying B incorporation significantly influences the electrical properties of the films, which are all strongly p-type, identified by Hall measurements. Figure 4.6(a), (b), and (c) show the variation of RT dark resistivity, mobility, and electrical concentration of as deposited and annealed Ge:H films as a function of  $P_B$ , respectively. Although it is well known that vacuum deposited polycrystalline Ge films invariably exhibit non-intentionally doped p-type (Chopra and Bahi 1970), the resistivity, as shown, has a tendency to decrease with increasing amount of incorporated B, as a consequence of the decrease of mobility and the considerable increase of carrier concentration. The correlation between the gradual degradation of the crystal qualities observed by Raman and XRD data discussed previously and the dramatic drop of resistivities of the films with increasing amount of incorporated B is not a contradiction, but offers evidence of successful activation of B dopant. It is not surprising because the required activation temperature is expected to be considerably lower than the diffusion temperature ( $>800^\circ\text{C}$ ). For instance, as previously mentioned, Satta *et al.* (Satta et al. 2005a) successfully activated ion-implanted B in c-Ge and preamorphized Ge by employing RTA in the range of  $400\text{-}600^\circ\text{C}$  while activation of ion-implanted B in c-Ge could occur during implantation process even without annealing (Simoen et al. 2006). The increasing amount of activated B dopants lead to the general trend of the decrease of mobility, stemming from the growing ionized impurity scattering effect (Sze and Ng 2007).

RTA also affects the electrical properties of the films. The author is aware that the possibility of formation of GeB alloy at such temperature and dopant level is excluded according to the boron-germanium phase diagram (Bidwell 1970). As shown in Figure 4.6(a), both RTA processes result in a slight decrease of resistivity of the non-doped films. The influence of RTA at  $550^\circ\text{C}$  for 120 seconds on the resistivity of the doped films is

insignificant because of the counteraction of the increased mobility and decreased carrier concentration shown in Figure 4.6(b) and (c). The increase of mobility may result from the improved crystal quality as revealed by Raman and XRD previously, whereas the decrease of carrier concentration from super-saturated values as deposited to thermal equilibrium values due to annealing effects (Makino and Nakamura 1981).

In contrast, RTA at 600°C for 60 seconds leads to slight increases of the resistivity of the doped films with B at  $P_B = 15$  W and 23 W but a significant drop with B at  $P_B = 55$  W as shown in Figure 4.6(a). This results from the decrease of mobility shown in Figure 4.6(b), associated with the deteriorated crystal quality again revealed by Raman and XRD previously, and the increase of electrical concentration shown in Figure 4.6(c). It is noted that the resistivity of the film doped with B at  $P_B = 55$  W reduces from 2.4 to 1.4 mΩ-cm after RTA at 600°C. By comparing the figures, it can be observed that the decrease of resistivity results from the considerable increase of carrier concentration (from  $6.24 \times 10^{19}$  to  $1.21 \times 10^{20}$  atoms/cm<sup>3</sup>) accompanied with deteriorated mobility (from 41.66 to 36.21 cm<sup>2</sup>/V-s). The increase of carrier concentration results from a non-equilibrium state obtained by the RTA at 600°C for 60 s. This observation indicates that the RTA process at 600°C has effectively improved the doping efficiency.

It's worth noting that the resultant electrical concentration,  $1.21 \times 10^{20}$  atoms/cm<sup>3</sup>, is significantly higher than the suggested maximum solid solubility of activated B dopants in Ge,  $\sim 2 \times 10^{18}$  atoms/cm<sup>3</sup> at 875°C (Uppal et al. 2004) and  $3 \pm 0.5 \times 10^{18}$  atoms/cm<sup>3</sup> at the melting point (937°C) for Czochralski grown Ge (Taishi et al. 2010). Table 4.1 summarizes the resistivity, mobility, and electrical concentration of the Ge:H films. To further improve the electrical properties, an optimization of RTA temperature profile

would be required. Besides, it should be noted that the required RTA temperature for our B doped Ge films is only 600°C, far below the threshold diffusion temperature of 800°C. Therefore, a near-rectangular doping concentration profile would be expected although slightly compensated due to n-type dopant diffusion from the base, where the concentration is considerably lower compared to that at the emitter. As a result, shallow junctions with abrupt concentration profile could be formed. This is of great importance for the fabrication of tandem thin film cells since the total thickness of the Ge bottom cells would be sub-micrometer while the thickness of the emitter would be only several tens of nanometers.

**Table 4.1:** Summary of the resistivity, mobility, and carrier concentration of the Ge:H films

Sample	Resistivity (mΩ-cm)			Mobility (cm <sup>2</sup> /V-s)			Concentration (atoms/cm <sup>3</sup> )		
	As depos.	RTA 550°C	RTA 600°C	As depos.	RTA 550°C	RTA 600°C	As depos.	RTA 550°C	RTA 600°C
P <sub>B</sub> =0W	69.03	57.42	55.52	78.80	78.67	88.15	1.15×10 <sup>19</sup>	1.38×10 <sup>18</sup>	1.28×10 <sup>18</sup>
P <sub>B</sub> =15W	5.55	5.41	5.47	53.65	57.18	53.81	2.10×10 <sup>19</sup>	2.02×10 <sup>19</sup>	2.12×10 <sup>19</sup>
P <sub>B</sub> =23W	4.24	4.18	4.46	48.94	50.44	45.34	3.01×10 <sup>19</sup>	2.96×10 <sup>19</sup>	3.09×10 <sup>19</sup>
P <sub>B</sub> =55W	2.40	2.41	1.42	41.66	43.42	36.21	6.24×10 <sup>19</sup>	5.96×10 <sup>19</sup>	1.21×10 <sup>20</sup>

#### 4.4.2 Phosphorus-doping of Poly-Ge Thin-Films

- XRD measurements

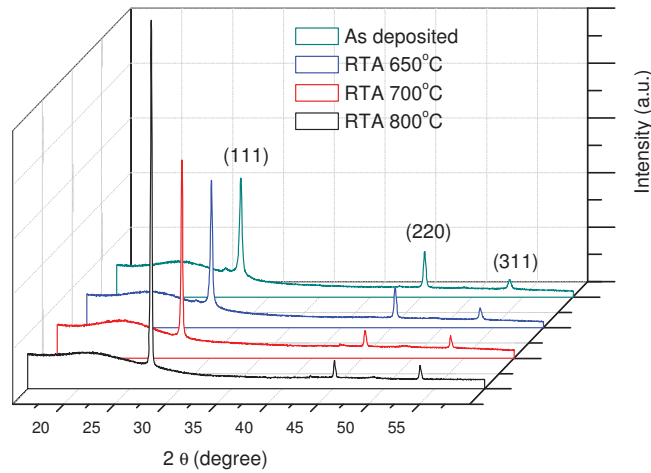


**Figure 4.7:** Comparison of the XRD spectra of Ge:H films as deposited at 500°C, and after RTA at 650°C for 180 seconds, 700°C for 60 seconds, and 800°C for 20 seconds.

The effect of different RTA conditions on the structural properties of the films is revealed by XRD measurements. Figure 4.7 compares the XRD spectra of Ge:H films as deposited at 500°C, annealed at 650°C for 180 seconds, 700°C for 60 seconds, and 800°C for 20 seconds. A hump at around  $2\theta = 22^\circ$  is attributed to the glass substrate. The diffraction peaks appearing at around  $2\theta = 27.3^\circ$ ,  $45.3^\circ$ , and  $53.7^\circ$ , correspond to the Ge (111), (220), and (311) crystal planes. As shown, the XRD characteristic peaks indicate all the films are of strong (111) preferential orientation [I111(100):I220(57):I311(39)]. The variation among the peak intensities of (220) orientation of the films is insignificant. In contrast, the intensities of (111) peak increase with increasing annealing temperature but decreasing annealing duration, suggesting that the annealing temperature is more critical than the annealing duration to promote the grain growth. Please note that, as expected, the film as deposited at 500°C exhibits pronounced (111) orientation, similar to those obtained in Chapter 3, where it was concluded that films of pronounced (111) orientation have larger grain sizes than those of pronounced (220) orientation. The larger grain sizes

may be attributed to the improved vacuum with lower pressure of background gases ( here 1mT) (Thompson 2000).

- Hot-probe measurements

The conduction types of the films identified by hot-probe measurements are listed in Table 4.2, where only the as deposited sample shows p-type conductivity while the others show n-type. The results are in agreement with those furthered verified by Hall-effect measurements, to be discussed later. As it is well known that poly-Ge films exhibit strong non-intentionally p-type conduction characteristic, associated with crystalgraphic defects (Sundaram and Garside 1984), as confirmed by the author's studies in Chapter 3, hereby the change of conduction type resulting from RTA is a sign of successful n-type doping.

Table 4.2: Summary of conduction types of poly-Ge:H films prepared at different conditions.

Sample	As deposited	RTA 650°C	RTA 700°C	RTA 800°C
Conduction type	p	n	n	n

- Hall measurements

Electrical properties including conduction type, sheet resistance, resistivity, mobility, and electrical concentration were examined by Hall measurements with the Van der Pauw method at room temperature. Figure 4.8 shows the conduction type and the variation of room temperature sheet resistance of as deposited and annealed Ge:H films on SiN<sub>x</sub>-coated glass. As presented in the figure, the results of Hall measurements further confirm the change of conduction type induced by the RTA process. In addition, the sheet

resistance apparently decreases with increasing annealing temperature as a consequence of improvement of crystal quality as well as thermal diffusion of P dopant.

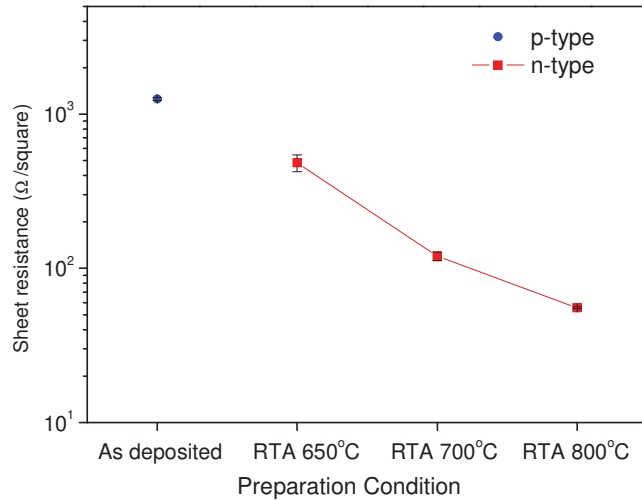


**Figure 4.8:** Variation of room temperature sheet resistance of as deposited and annealed Ge:H films on SiN<sub>x</sub>-coated glass.

Assuming the thermally diffused P dopants reaching the glass substrate with a constant profile, then resistivity, mobility, and electrical concentration can be roughly estimated as below. Figure 4.9 illustrates the variation of room temperature dark resistivity of as deposited and annealed Ge:H films on SiN<sub>x</sub>-coated glass, proportional to the sheet resistance mentioned above. Figure 4.10 shows the room temperature mobility of as deposited and annealed Ge:H films on SiN<sub>x</sub>-coated glass. Interestingly, despite the slightly better crystal quality revealed by XRD measurements, the mobility of the sample annealed at 650°C is apparently lower than that of the as deposited sample. This may be mainly attributed to the resultant P-diffusion (n-type) at the surface side of the poly-Ge:H film.

This point will be supported by the conduction type change of the film depicted in Figure 4.12. In addition, the relatively low mobility of the sample annealed at 650°C could be also partially due to the ionized impurity scattering effect (Sze and Ng 2007), owing to the successfully diffused and activated P dopants. Once the annealing temperature is increased to 700°C, the mobility is apparently increased to a level similar to that of the as deposited film. This is attributed to the effect of ionized impurity scattering as in this case the P dopants reach the bottom of the film as revealed later in Figure 4.12. In the case of 800°C of annealing temperature, the mobility is further increased mainly because of the significant improvement of crystal quality as revealed by XRD measurements. Figure 4.11 depicts the variation of room temperature electrical concentration of as deposited and annealed Ge:H films on SiN<sub>x</sub>-coated glass. The increase of electrical concentration with increasing RTA temperature offers evidence of effective n-type doping.

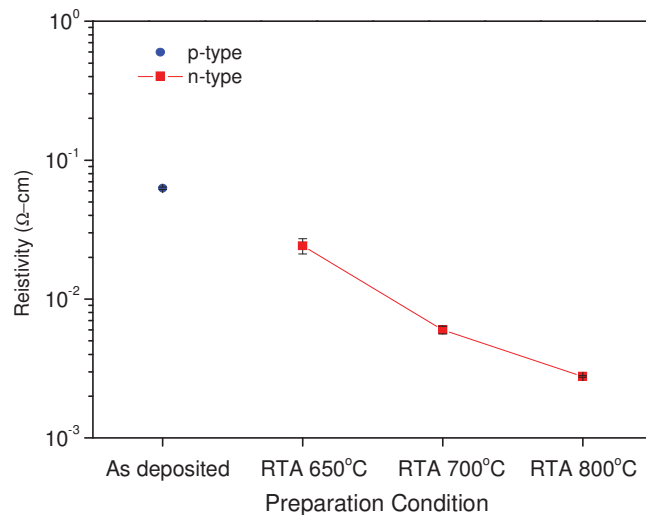


**Figure 4.9:** Variation of room temperature dark resistivity of as deposited and annealed Ge:H films on SiN<sub>x</sub>-coated glass.

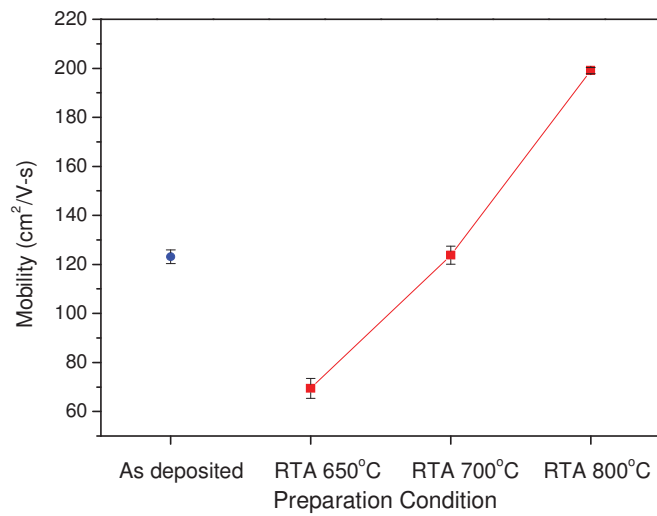


**Figure 4.10:** Variation of room temperature mobility of as deposited and annealed Ge:H films on SiN<sub>x</sub>-coated glass.

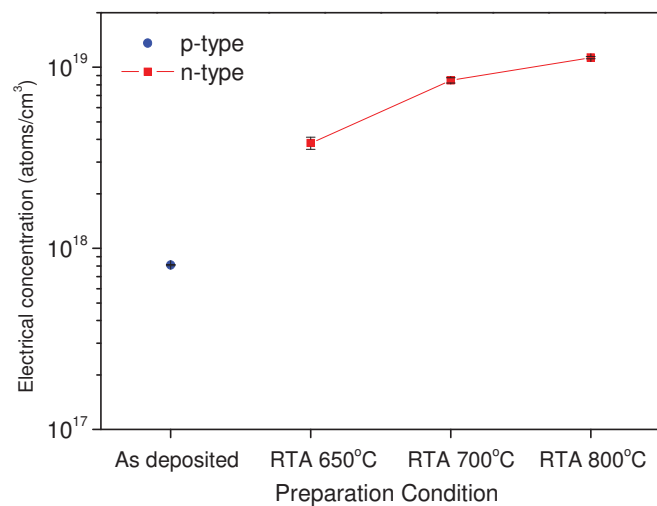


**Figure 4.11:** Variation of room temperature electrical concentration of as deposited and annealed Ge:H films on SiN<sub>x</sub>-coated glass.

- Etched depth profile of resistivity

By repeatedly applying a combination of the four-point-probe technique, hot-probe technique, and the layer removal method, the profile of the sheet resistance and the conduction type of the Ge:H films as a function of depth below the original surface was obtained. Table 4.3 presents the details of the layer removal steps as well as the obtained sheet resistance and conduction type of the 500 nm thick Ge:H films, annealed at (a) 650°C (b) 700°C (c) 800°C, as a function of depth below the original surface, Sheet resistance profiling results for the Ge:H films are depicted in Figure 4.12.

As shown, the sample annealed at 650°C has a sheet resistance of  $893\Omega/\square$  with n-type characteristic at the original surface. By stepwise plasma-etching and measuring the sample, the conduction type changes to p-type while the sheet resistance monotonically increases to  $8535\Omega/\square$ . The change of conduction type from n to p indicates that thermal diffusion of phosphorus into the Ge:H is shallow and the depth of the n-type layer is less than 179 nm as the rest of the film remains non-intentionally p-type doped. This explains why the sample has a lower mobility as shown in Figure 4.10. Please note that a peak, where the p/n junction is located, would appear between the original surface and 179 nm if the resolution of the depth profiling was sufficient high (Aberle and Inns 2004). In contrast, the n-type diffusion of the samples annealed at 700°C and 800°C seem to be reaching the substrate. The negative conduction types identified from all the three annealed samples again offer evidence of successful activation of P dopant. The apparently lowest sheet resistance over the profile of the sample annealed at 800°C implies the highest electrical carrier concentration. To further determine the chemical concentration profiles, the measurements by secondary ion mass spectroscopy would be required.

**Table 4.3:** The details of the layer removal steps as well as the obtained sheet resistance and conduction type of the Ge:H films, annealed at (a) 650°C (b) 700°C (c) 800°C, as a function of depth below the original surface.

(a)

Depth (nm)	total time(min)	step time(s)	FWD [ $\Omega/\square$ ]	REV [ $\Omega/\square$ ]	Type	Average	Stand Deviation
0	0		819	967	n	893	105
179	2	120s	2840	2940	p	2890	71
269	3	60s	4140	4200	p	4170	42
358	4	60s	7986	7990	p	7988	3
381	4.25	15s	8300	8350	p	8325	35
403	4.5	15s	8380	8390	p	8385	7
425	4.75	20s	8540	8530	p	8535	7
500	5.583	finish					

(b)

Depth (nm)	total time(min)	step time(s)	FWD [ $\Omega/\square$ ]	REV [ $\Omega/\square$ ]	Type	Average	Stand Deviation
0	0		125	197	n	161	51
222	2	120s	396	449	n	422.5	37
333	3	60s	676	721	n	698.5	32
444	4	60s	1373	1370	n	1371.5	2
472	4.25	15s	1790	1809	n	1799.5	13
500	4.5	finish					

(c)

Depth (nm)	total time(min)	step time(s)	FWD [ $\Omega/\square$ ]	REV [ $\Omega/\square$ ]	Type	Average	Stand Deviation
0	0		64.25	57.9	n	61	4
207	2	120s	104	156	n	130	37
310	3	60s	143	202	n	172.5	42
414	4	60s	549	553	n	551	3
440	4.25	15s	500	530	n	515	21
465	4.5	15s	518	530	n	524	8
500	4.83	finish					

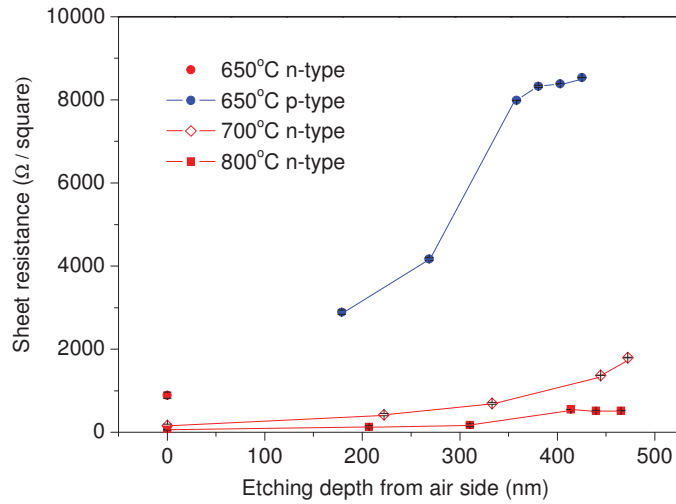


**Figure 4.12:** The depth profile of the sheet resistance and conduction type of the Ge:H films, annealed at (a) 650°C (b) 700°C (c) 800°C, as a function of depth below the original surface.

## 4.5 Summary

This chapter investigates B (p-type) doping and P (n-type) doping of sputter-deposited poly-Ge:H thin films. P-type poly-Ge:H films were sputtered and *in situ* doped by co-sputtering Ge with B in argon and hydrogen plasma at 500°C. The dramatic drop of the resistivity of the films, caused by the addition of B, is evidence of successful activation of B dopant. The post annealing processes alter the structural and electrical properties of the films. The RTA at 550°C for 120 s favors the structural properties of the films, and hence results in an improvement of film mobility. In contrast, the higher temperature but lower duration RTA at 600°C for 60 s enhances the activation of B dopants, especially in the heavily doped case, where a carrier concentration of  $1.21 \times 10^{20}$  atoms/cm<sup>3</sup> was obtained. This low thermal budget process is compatible to Schott Borofloat33 glass, currently used in commercial poly-Si thin film solar cells. This process temperature, far below the

required diffusion temperature of B in Ge, makes the formation of shallow abrupt junctions possible. A brief report and a more detailed study of the heavily doped Ge:H films on glass formed by co-sputtering have been published in *Electrochemical and Solid-State Letters* (Tsao et al. 2010b) and *Solar Energy Materials & Solar Cells* (Tsao et al. 2011a), respectively.

On the other hand, an approach for phosphorus doping of poly-Ge:H has been developed. Initial results indicate the success of this n-type doping approach for sputter-deposited poly-Ge:H films. Nevertheless, how to combine and optimize the p-type and n-type doping technologies for the poly-Ge:H films would need further investigation. Considering the fabrication cost, *ex situ* doping approaches should be avoided. Therefore, it would be more cost effective to use  $\text{PH}_3$ , once available, for the *in situ* n-type doping of the films.

# CHAPTER

# 5

## ***In situ* Growth of Ge-rich Poly-SiGe:H Thin Films on Glass**

---

---

- *Overview*
- *Literature review*
- *Experiment*
- *Results and discussion*
- *Summary*

### **5.1 Overview**

Chapter 2-4 have investigated fabricating polycrystalline Ge (poly-Ge) films with and without hydrogenation, as well as controlled doping of the hydrogenated poly-Ge, with an aim to develop a material for bottom sub-cells under SiGe monolithic thin film solar cells. Despite the capability of absorbing long wavelength light, Ge bottom sub-cells are expected to suffer from low open circuit voltage ( $V_{oc}$ ) due to the inherent narrow band gap, 0.66 eV, of Ge. Since the total cell current is determined by the lowest sub-cell current while the total cell voltage is a sum of those of all sub-cells, the contribution of a

bottom sub-cell is the addition of voltage at the expense of sharing light absorption and thus lowering cell current. Therefore, to raise the cell efficiency effectively, the  $V_{oc}$  of a bottom sub-cell should be enhanced as much as possible. Towards this end, using Ge-rich SiGe alloys for bottom cells will be appealing. This chapter extends the research scope into polycrystalline Ge-rich SiGe alloy material to explore the properties of Ge layers alloyed with small amounts of Si by RF sputtering.

Section 5.2 gives a literature review, providing the background about the fabrication of SiGe alloys. Section 5.3 provides the experimental details of the work described in this chapter. Hydrogenated SiGe (SiGe:H) thin films on silicon nitride ( $\text{SiN}_x$ ) coated glass were prepared by RF magnetron sputtering. The *in situ* hydrogenation is employed to improve the structural and electrical properties of the films (Tsao et al. 2010a). Films with a thickness of  $\sim 300$  nm were as deposited at  $500^\circ\text{C}$ . Si and Ge atomic percentage of the films was determined by X-ray photoelectron spectroscopy (XPS). To compare the microstructure of the films grown with different Ge content, the surface morphology was analysed by atomic force microscopy (AFM). Structural properties of films were examined by Raman and X-ray diffraction (XRD) measurements. For optical properties, reflectance and transmittance spectra were used to determine the absorption coefficient, from which optical band gaps were derived by using the Tauc method. The conduction type and resistivity of the films were identified and determined by hot-probe and four point-probe techniques, respectively. Section 5.4 presents the results and discussion. The influence of varying Si fraction on the structural evolution, band gap shift and resistivity variation of the films is presented. The correlation between the roughness, structural, optical and electrical properties are explored and discussed. Section 5.5 summaries the findings in this chapter.

## 5.2 Literature review

Ge-rich SiGe alloys gain less attention in contrast with their Si-rich peers. Graeff *et al.* (Graeff and Chambouleyron 1994) have investigated Ge-rich hydrogenated amorphous SiGe films prepared by RF sputtering while Cannon *et al.* (Cannon *et al.* 2007) have epitaxially grown Ge-rich SiGe films directly on silicon substrates by ultrahigh vacuum chemical-vapor deposition (CVD) at temperatures  $\geq 600^\circ\text{C}$  followed by a vacuum annealing at  $900^\circ\text{C}$  for  $\geq 20$  min. In addition, polycrystalline SiGe (poly-SiGe) films on quartz have been fabricated by CVD followed by laser-crystallization (Scheller *et al.* 2009). For obtaining poly-SiGe materials the higher Si fraction will require higher thermal budget since the melting point of Si ( $1414^\circ\text{C}$ ) is considerably higher than that of Ge ( $937^\circ\text{C}$ ). As a result, most of the studies in fabricating polycrystalline Si-rich SiGe alloy materials required a post deposition process, such as solid phase crystallization with high thermal budget (Choi *et al.* 2002; Jelenkovic. *et al.* 1997; Olivares *et al.* 2000). Early reports (Koschier *et al.* 1999; Weber and Alonso 1989) have indicated that for  $\text{Si}_x\text{Ge}_{1-x}$  alloys, in Ge-rich region the band gap may rapidly increase with increasing Si fraction, and then slowly increases when  $x > 0.15$ . This implies that an effective gain of band gap could be obtained with relatively little incorporation of Si within the region. Since poly-Ge films with grain size  $> 100$  nm could be obtained by *in situ* sputtering at  $450^\circ\text{C}$  (Tsao *et al.* 2010c), it is expected that Ge-rich poly-SiGe alloy materials could be obtained by *in situ* sputtering at a reasonably low temperature.

### 5.3 Experiment

An AJA ATC2200 RF magnetron sputtering system equipped with a substrate holder heated by a quartz halogen lamp heater was used for SiGe:H deposition. Films were deposited onto glass by co-sputtering a 2" intrinsic Ge target (99.999% purity) with a 4" Si target (99.999% purity) in an argon (15 sccm) and hydrogen (10sccm) mixture with a process pressure of 2mTorr. The Ge and Si deposition rate were monitored by a crystal monitor. SiN<sub>x</sub>-coated borosilicate glass panes (Borofloat33, 5×5 cm<sup>2</sup>, 3 mm thick) were used as substrates. The SiN<sub>x</sub>-coated glass panes were cleaned with de-ionized water in an ultrasonic bath and were then heated at 200°C in a furnace in nitrogen ambient for 10 minutes to remove any residual moisture prior to deposition. Substrates were rotated at 30 revolutions per minute during deposition to ensure the uniformity of the films. The temperature calibration data was supplied by the manufacturer of the sputter system and measured with a Si wafer.

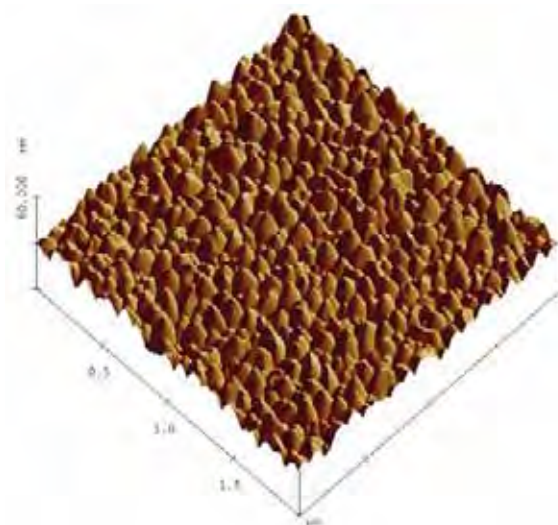
XPS measurements were carried out by using a Fisons ESCALAB 220i-XL with a monochromatic Al K $\alpha$  (1486.5 eV) x-ray source and a hemispherical energy analyzer. Raman spectra of the samples were measured at RT with a micro-Raman spectroscopy (Renishaw inVia Raman Microscope) in backscattering configuration, with a 50× optical microscope objective and using an Ar<sup>+</sup> laser with wavelength of 514.5 nm as the excitation source. To prevent local laser annealing on the films during measurement, the samples were excited with the beam power limited to 6 mW. The measurement mode was static while 20 times accumulation was used to improve the signal to noise ratio. Before

measurement of the SiGe:H films, a single crystal FZ-Si wafer, which had a narrow peak at around  $520\text{ cm}^{-1}$ , was used to calibrate the Raman system regarding wavenumber. XRD measurements were performed (PANalytical's X'Pert Pro materials research diffraction system) at a voltage of 45 kV and a current of 40 mA, using Cu K $\alpha$  radiation ( $\lambda = 1.54\text{ \AA}$ ). The AFM measurements were performed using the tapping mode (Digital Instruments 3000). The scan area was  $2\text{ }\mu\text{m} \times 2\text{ }\mu\text{m}$  while the scan rate was 0.37 Hz. Reflectance and transmittance measurements were performed (Perkin Elmer Lambda 1050 UV/VIS/NIR Spectrometer) in a wavelength range of 200-2400 nm.

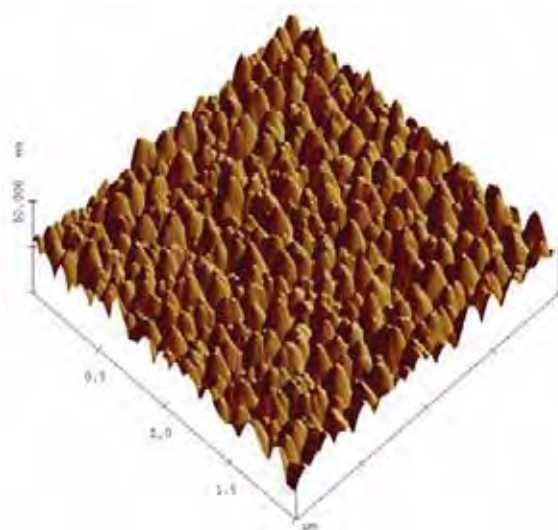
## 5.4 Results and discussion

### 5.4.1 Surface morphology

Varying Si fraction influences the surface morphology of the SiGe:H films, reflected in the  $2\text{ }\mu\text{m} \times 2\text{ }\mu\text{m}$  three dimensional AFM images shown in Figure 5.1 (a)-(d). Figure 5.2 depicts root-mean-square (RMS) roughness value of the films as a function of Si fraction, which was extracted from the AFM measurements by analyzing the image quantitatively with the data processing software package of the Digital Instruments. As shown, the RMS roughness increases monotonically from 2.87 to 6.01 nm, with decrease of Si fraction  $x$  from 0.246 to 0.048. Since surface roughness may be caused by protruding crystallites as reported in the literature (Collins 1985), the increase of roughness is a sign of a raised degree of crystallization with decreasing Si fraction, as will be confirmed later by the results of XRD measurements.



(a)  $x=0.246$



(b)  $x=0.137$

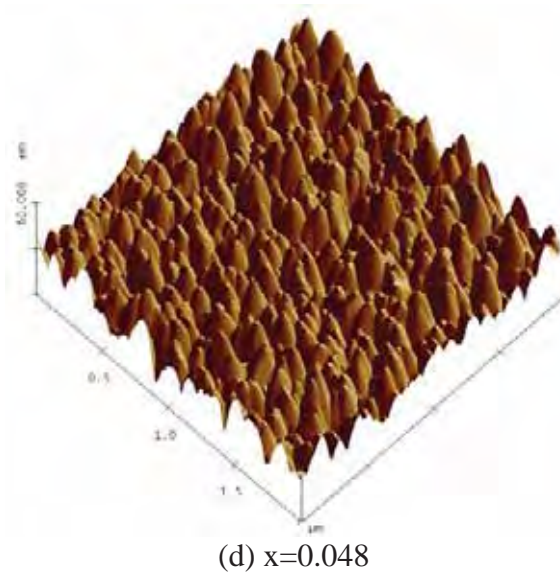
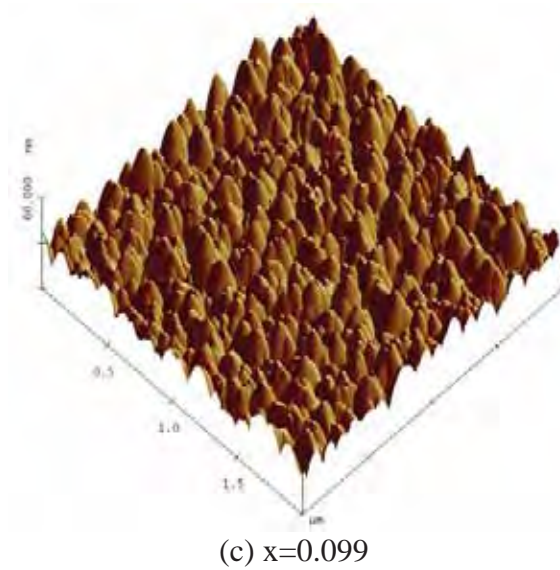


**Figure 5.1:**  $2\mu\text{m}\times 2\mu\text{m}$  three dimensional AFM images of  $\text{Si}_x\text{Ge}_{1-x}:\text{H}$  films with various Si fraction: (a)  $x=0.246$ , (b)  $x=0.137$ , (c)  $x=0.099$ , (d)  $x=0.048$

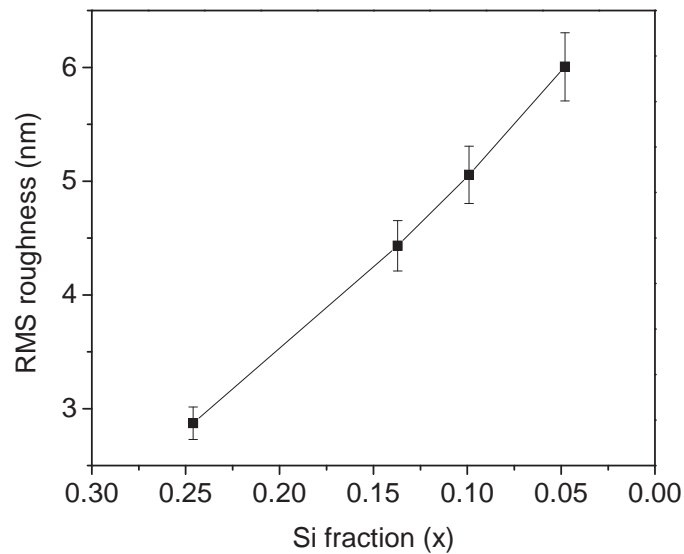


**Figure 5.2:** RMS roughness of the  $\text{Si}_x\text{Ge}_{1-x}:\text{H}$  films as a function of Si fraction.

## 5.4.2 Structural properties

### ● XRD measurements

Varying Si fraction significantly affects structural properties of the films revealed by XRD measurements. The XRD spectra, shown in Figure 5.3, all exhibit singular peaks, corresponding to the {111}, {220}, {311} planes. A hump at around  $22^\circ$  is attributed to the glass substrate. The absence of dual peaks offers evidence that the deposited films are composed of  $\text{Si}_x\text{Ge}_{1-x}$  alloy material, rather than clusters of Si or Si-rich material embedded in a Ge matrix (King and Saraswat 1994). The films evolve from (220) to strong (111) preferential orientation, indicating the crystallinity of the films is improved with decreasing Si fraction, in agreement with work published elsewhere (K.Teh et al. 2001). The pronounced (111) diffraction peak of the  $\text{SiGe}:\text{H}$  films with  $x \leq 0.099$

indicates the films are polycrystalline. The grain size ( $g$ ) of the film was estimated from the FWHM of (111) XRD characteristic peaks using the Scherrer formula

$$g = \frac{0.9\lambda}{\Delta(2\theta)\cos\theta} \quad (5.1)$$

where  $\lambda$  is the wavelength (1.54 Å) of the X ray,  $\theta$  is the angle satisfying Bragg's law, and  $\Delta(2\theta)$  is the FWHM in radian (Song et al. 2008a). In this estimation,  $\Delta(2\theta)$  was corrected by subtracting it from an analogous value for a reference sample (Grigućeviciene et al. 2004) with  $g > 10 \mu\text{m}$  to correct for the effect of instrumental broadening (Hasegawa et al. 1995). The estimated grain sizes of the films are shown in Figure 5.4 as a function of Si fraction. As expected, the decrease of Si fraction  $x$  leads to an increase of grain size. With decreasing  $x$  from 0.246 to 0.048, the grain size increases from ~52 nm to ~132 nm.

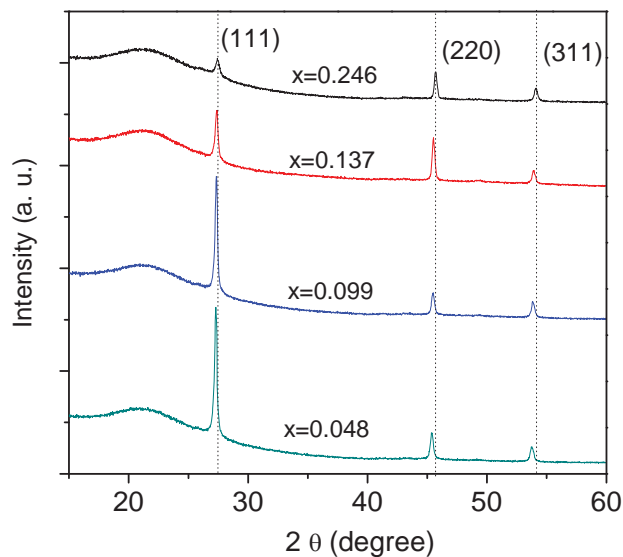


**Figure 5.3:** XRD spectra of the  $\text{Si}_x\text{Ge}_{1-x}$  films with various Si fraction  $x \leq 0.246$  sputter-deposited at  $500^\circ\text{C}$ .

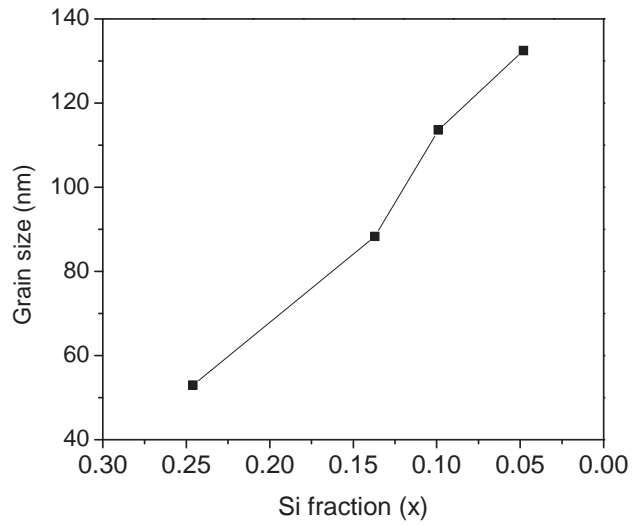


**Figure 5.4:** Estimated grain size of the  $\text{Si}_x\text{Ge}_{1-x}$  films with various Si fraction  $x \leq 0.246$  sputter-deposited at  $500^\circ\text{C}$ .

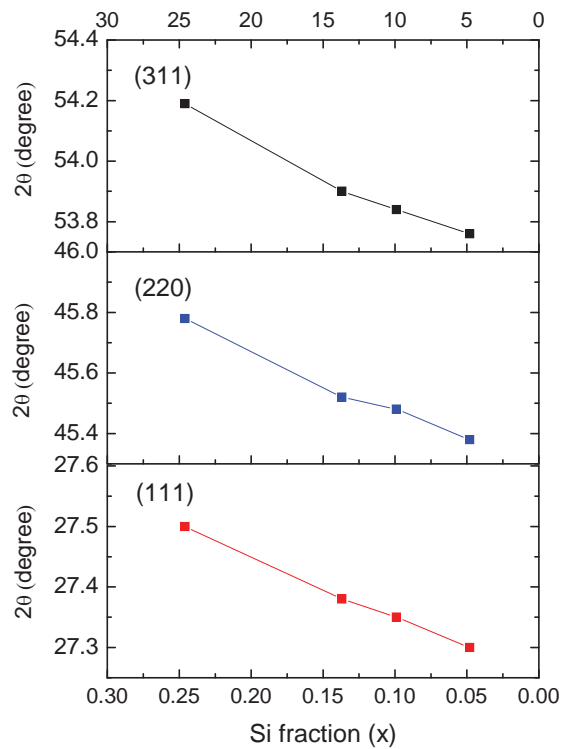


**Figure 5.5:** Diffraction peak angles of the (111), (220), and (311) orientations of the  $\text{Si}_x\text{Ge}_{1-x}$  films with various Si fraction  $x \leq 0.246$  sputter-deposited at  $500^\circ\text{C}$ .

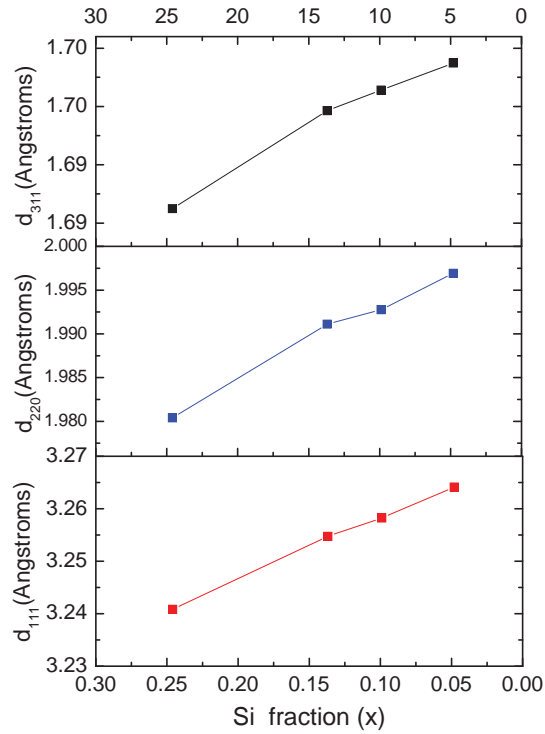


**Figure 5.6:** Interplanar spacings in the  $\text{Si}_x\text{Ge}_{1-x}:\text{H}$  films as a function of the Si fraction.

The singular peaks are located in between those of poly-Si and poly-Ge, and are shifted more towards those of pure Ge for the films with lower Si content, as shown in Figure 5.5. The shifts of the peaks are a result of the modification of the interplanar spacings,  $d_{hkl}$ , which can be determined from Bragg's law

$$n\lambda = 2 d_{hkl} \sin \theta \quad (5.2)$$

where  $n = 1$ ,  $\lambda$  is the wavelength (1.54 Å) of the X ray,  $\theta$  is the angle satisfying Bragg's law (King and Saraswat 1994). Figure 5.6 shows the  $d_{111}$ ,  $d_{220}$ ,  $d_{311}$  interplanar spacings as a function of Si fraction. It has been reported that the interplanar spacings vary proportionately with the amount of minority fraction, enabling the use of Vegard's law for estimating the minority fraction in SiGe:H films from XRD measurements (King and Saraswat 1994). Note that the curves shown in the figure are not perfectly linear,

implying that some lattice distortion exists (King and Saraswat 1994), likely stemming from the strain in the films.

### ● Raman measurements

The influence of varied Si fraction on the structural properties was also revealed by Raman measurements. Figure 5.7 shows the Si fraction dependence of Raman spectra of the SiGe:H samples. The  $\text{Si}_{0.246}\text{Ge}_{0.754}\text{:H}$  film exhibits three peaks at around 280, 390, and 460  $\text{cm}^{-1}$ , corresponding to Ge-Ge, Si-Ge, and Si-Si bonds. It is known that the composition and strain in the SiGe:H films are the main factors influencing the position of the peaks (Choi et al. 2002). Instead of the strain commonly induced from the lattice mismatch between the deposited SiGe layer and the underlying Si wafer substrate, the strain in the current case mainly originates from the difference of the linear thermal expansion coefficient between SiGe:H layer with different composition of Ge ( $5.8 \times 10^{-6} \text{ K}^{-1}$ ) as well as Si ( $2.6 \times 10^{-6} \text{ K}^{-1}$ ), and borofloat glass ( $3.25 \times 10^{-6} \text{ K}^{-1}$ ). For a pure Ge film on borofloat glass, the strain will be tensile because of its larger linear thermal expansion coefficient than that of the glass. For Ge-rich SiGe:H films, it is reasonable to expect that the tensile strain in the film would be reduced with increasing Si fraction. In the current case, the degree of film crystallinity is an additional factor influencing the Raman peak position. By comparing the Raman peaks, the more red-shifted Ge-Ge peak of the  $\text{Si}_{0.246}\text{Ge}_{0.754}\text{:H}$  film compared to those of its peers with less Si fraction is attributed to the lower degree of crystallinity rather than tensile strain. With decreasing Si fraction, the relative intensity of the Ge-Ge peak increases, accompanied with a reduced peak width, indicating the improvement of film crystallinity, in agreement with the XRD data aforementioned. As the degree of crystal perfection improves with decreasing Si fraction,

that the Ge-Ge peak shifts to its bulk value is expected. In contrast, the intensity of the Si-Ge peak decreases and the peak position moves towards low wavenumbers as a consequence of the number of Si-Ge bond decreasing while the weak Si-Si peak decays and becomes insignificant. Figure 5.8 shows the peak locations of the Ge-Ge and Si-Ge bands by Gaussian curve fitting as a function of Si fraction. The fitting of the Si-Si band was not reliable due to its low intensity and is thus not considered. It can be seen that the peak locations shift almost linearly with decreasing Si fraction except those with  $x = 0.246$ . The apparent deviation of peak locations of the  $\text{Si}_{0.246}\text{Ge}_{0.754}\text{:H}$  is attributed to the much lower degree of crystallinity as concluded by XRD data.

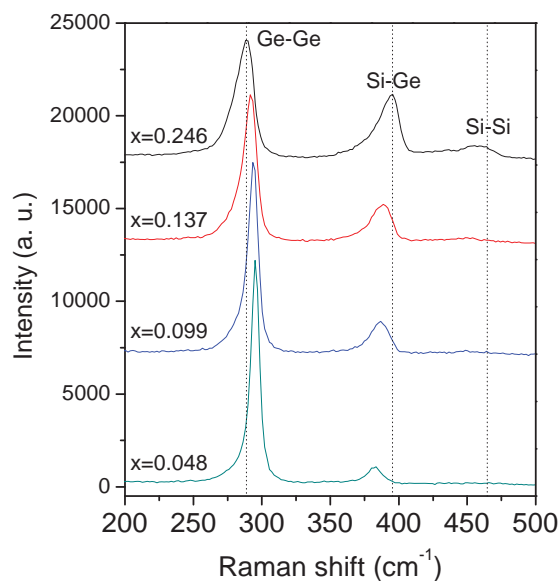


**Figure 5.7:** Raman spectra of the  $\text{Si}_x\text{Ge}_{1-x}\text{:H}$  films with various Si fraction  $x \leq 0.246$  sputter-deposited at  $500^\circ\text{C}$ .

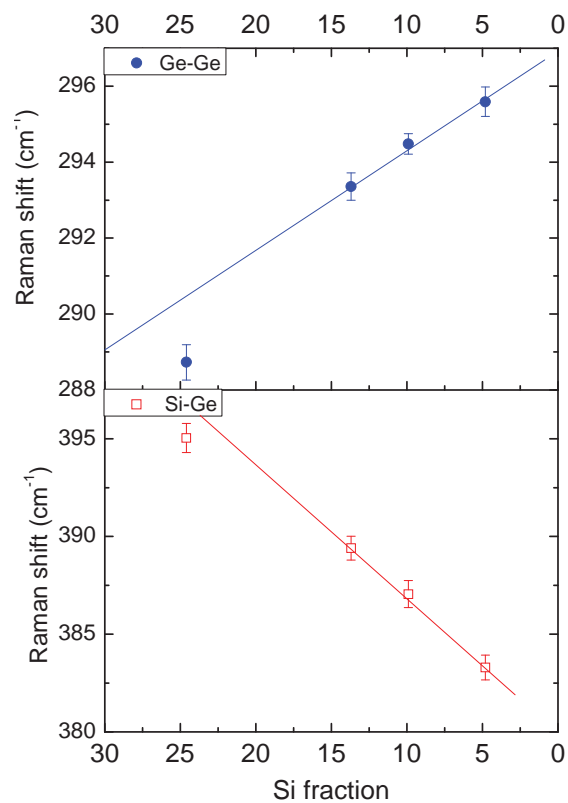


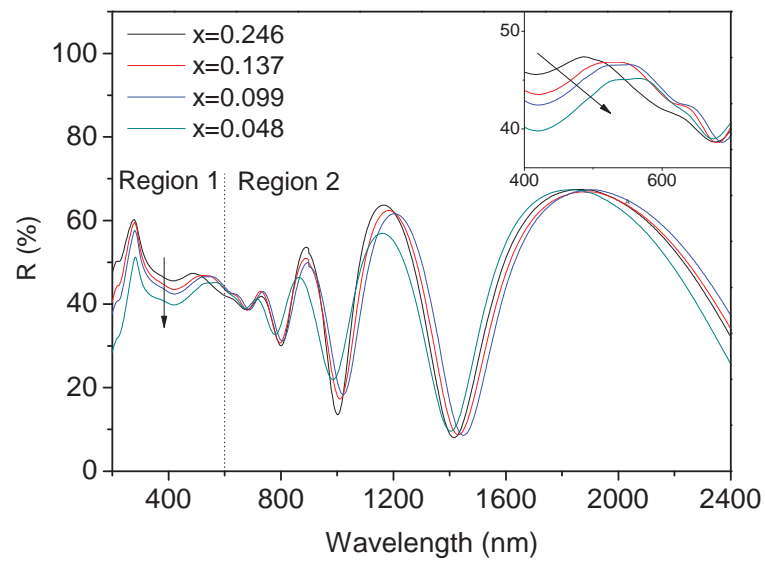
**Figure 5.8:** The peak locations of the Ge-Ge and Si-Ge bands by Gaussian curve fitting as a function of Si fraction.

### 5.4.3 Optical properties

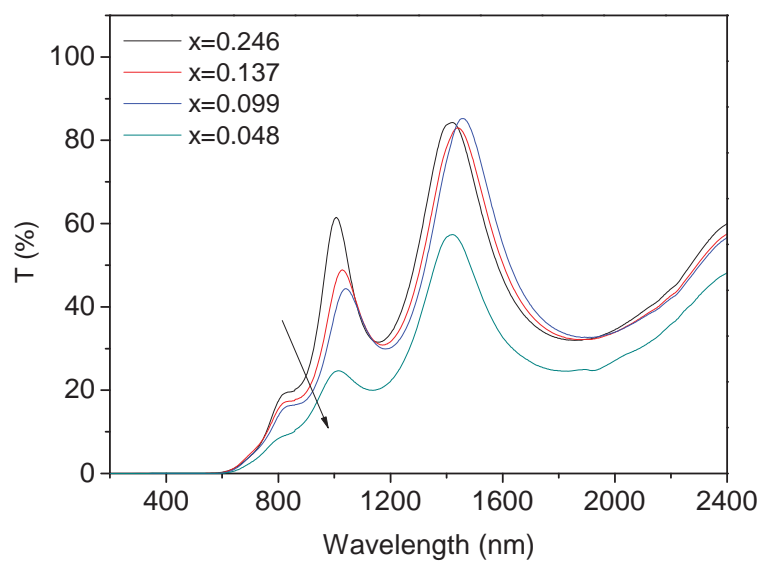
- **Reflectance and transmittance**

Figure 5.9 shows the dependence of the optical reflectance ( $R$ ) and transmittance ( $T$ ) of  $\text{Si}_x\text{Ge}_{1-x}:\text{H}$  films on the Si fraction. Arrows across the curves indicate the trend with decreasing Si fraction. For the reflectance spectra, the curves can be separated roughly into two regions of interest: wavelengths  $\lambda < \sim 600$  nm (region 1, i.e. ultraviolet-visible (UV-VIS) region) and  $\lambda > \sim 600$  nm (region 2). In region 2, the curves exhibit interference fringes, indicating incomplete absorption. With decreasing wavelength the envelopes bounding interference extrema decay with the onset of stronger absorption. In region 1,

reflection spectra are strongly dependent on the near-surface crystallinity (Aberle 2006). The decreasing Si fraction leads to apparent reflectance reduction in this region (see Figure 5.9(a)). This is not interpreted as a reduction in crystal quality, but is attributed to a graded effective refractive index because of the monotonically increasing sub-wavelength scale of surface roughness, up to ~6 nm, as revealed by the author's AFM measurements earlier. It is noted that the inset in Figure 5.9(a) shows pronounced peaks shifting from ~480 to ~550 nm. This peak corresponds to the "indirect transition (E1)" of SiGe:H material. Since "E1" of Si locates at ~367 nm (Aberle 2006) while that of Ge locates at ~558 nm (Yu and Cardona 2003), it is reasonable to expect that with decreasing Si fraction the "E1" peak shifts towards that of Ge. The transmittance in the range between ~900 to 600 nm reduces with decreasing Si fraction as shown in Figure 5.9(b) although the degree of crystallinity of the films increases. This trend, opposite to that found earlier for the pure sputtered Ge films evolving from amorphous to polycrystalline phase by the author (Tsao et al. 2010c), suggests the Si content dominates the influence on the transmittance over the film crystallinity due to the considerably higher absorption coefficient of Ge compared to Si (Sze and Ng 2007). This decrease of transmittance and the increase of absorption in the reflectance spectra appear to be a consequence of increasing the number of Ge-Ge bonds in the SiGe:H films.



(a)



(b)

**Figure 5.9:** The reflectance ( $R$ ) and the transmittance ( $T$ ) spectra of  $\text{Si}_x\text{Ge}_{1-x}:\text{H}$  films sputtered with various Si fraction: (a)  $R$  and (b)  $T$ . Arrows across the curves indicate the decreasing Si fraction.

- **Band gap**

To examine the effect of varying Si fraction on the optical band gaps of the SiGe:H films, the Tauc method is employed. Equations (5.3) and (5.4) (Demichelis et al. 1987; Song et al. 2008b) below were used to calculate the SiGe:H absorption coefficient  $\alpha$  deduced from the  $R$  and  $T$ :

$$T = (1 - R)\exp(-\alpha t), \quad (5.3)$$

$$\alpha = \frac{1}{t} \ln\left(\frac{1 - R}{T}\right), \quad (5.4)$$

where  $t$  is the thickness of the film. Equation (5.4) uses  $T$  to account for absorption and  $R$  to correct for uncoupled light. It should be noted that Equation (5.4) is only valid where  $T$  is nonzero, disabling this equation from use at wavelength  $< \sim 600$  nm in our case.

The optical band gap energy ( $E_g$ ) was then determined by Tauc's equation (Pilione et al. 1987; Song et al. 2008b), given as

$$(\alpha h\nu)^{\frac{1}{n}} = B(h\nu - E_g), \quad (5.5)$$

where  $h\nu$  is the photon energy,  $B$  is the edge width parameter dependent on structural disorder of films, and the exponent  $n$  depends on the type of transition. For an indirect-allowed transition,  $n = 2$  (Banerjee and Chattopadhyay 2005), which was chosen for our SiGe:H films as Si and Ge are both known as indirect semiconductors. Although equation (5.5) was originally developed and is most suitable for extracting the band gap for amorphous materials, it has been used to determine the band gap of nano-crystalline materials (Banerjee and Chattopadhyay 2005; Song et al. 2008b) and poly-Ge films (Tripathi et al. 2006). Here it was used to roughly estimate the band gap shift of our SiGe:H films.

Figure 5.10 shows a Tauc plot of  $(ah\nu)^{1/2}$  versus photon energy  $h\nu$  of SiGe:H films sputtered with various Si fraction based on the  $\alpha$  values obtained from  $R$  &  $T$ . The linear portion in the range of 1.4-1.7 eV was extrapolated to yield the optical band gap  $E_g$  at  $(ah\nu)^{1/2} = 0$ . It is noted that the linear portions are very limited, except for that of the  $\text{Si}_{0.246}\text{Ge}_{0.754}$  film, likely because in addition to varied Si and Ge content, SiGe:H material with higher degree of crystallinity can be described as composing different homogenous components- intragrain, grain boundary and other regions where dangling bonds occur. As demonstrated in the figure, there is a general trend for the band gaps to decrease with decreasing Si fraction. The estimated band gap of the  $\text{Si}_{0.246}\text{Ge}_{0.754}$ :H film is  $\sim 1.07$  eV, while that of the  $\text{Si}_{0.048}\text{Ge}_{0.952}$  film is  $\sim 0.78$  eV, shifting towards that of crystalline Ge. The estimated band gaps of the films are apparently higher than expected. This is because the band gaps are not only influenced by the Si and Ge composition but, in our case, also affected by the degree of crystallinity and the level of hydrogen incorporation. It is noted that although hydrogen incorporation may widen the band gaps, the author expects the band gap widening by hydrogen content of the films would be minor. As deposited at  $T_s = 500^\circ\text{C}$ , the infrared absorption peaks, indicating the residual hydrogen in the films, will be very weak according to the author's experience (Tsao et al. 2010a). As mentioned, the above method is limited to wavelengths where  $T > 0$  (see Figure 5.9(b)). To explore outside this range, other approaches, such as spectroscopic ellipsometry, would be required.

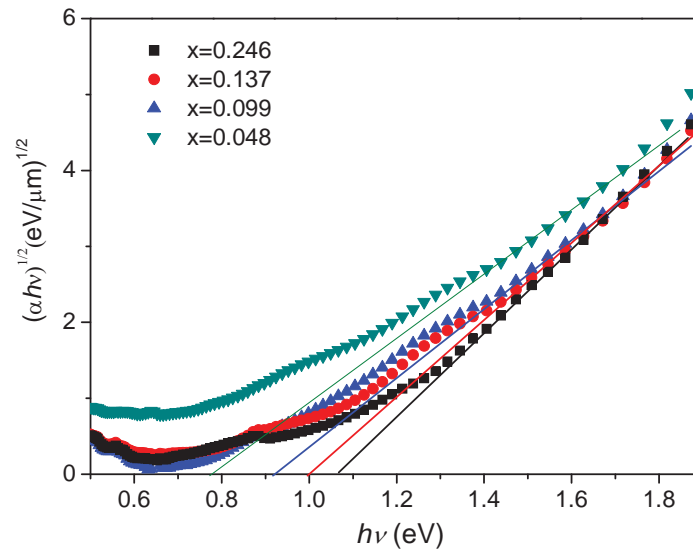


**Figure 5.10:** A Tauc plot of  $(\alpha h\nu)^{1/2}$  versus photon energy  $h\nu$  of  $\text{Si}_x\text{Ge}_{1-x}:\text{H}$  films sputtered with various Si fraction based on the  $\alpha$  values obtained from  $R$  &  $T$ .

#### 5.4.4 Electrical properties

It is interesting to verify the influence of varying Si fraction on the conduction type of SiGe:H films. This is because Si films may exhibit unintentionally-doped n-type conductivity associated with oxygen incorporation (Platz and Wagner 1998), whereas vacuum-deposited poly-Ge invariably exhibit strong p-type, associated with crystallographic defects (Sundaram and Garside 1984). As identified by the hot-probe technique, all the SiGe:H films in this work exhibit p-type conductivity, suggesting that for our highly Ge-rich SiGe:H films, the conduction type is mainly dominated by Ge.

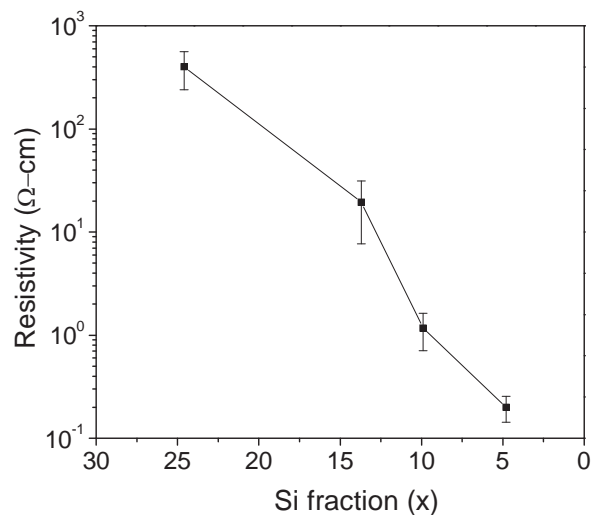


**Figure 5.11:** The resistivity of the unintentionally-doped  $\text{Si}_x\text{Ge}_{1-x}:\text{H}$  films as a function of Si fraction.

Also interesting is the influence of varying Si fraction on the resistivity of the films. Figure 5.11 shows the variation of the resistivity of the films as a function of Si fraction. It can be seen that with decreasing Si fraction from  $x=0.246$  to  $0.048$ , the resistivity dramatically decreases more than 3 orders of magnitude. The high sensitivity of the resistivity to the Si fraction can be attributed to two factors. Firstly, Ge is a higher bulk-mobility material compared with Si. Secondly, the larger grain size of the films with decreasing Si fraction, as revealed by XRD data, may further lead to a significantly lower resistivity. As mentioned, poly-Ge films may exhibit strong p-type conductivity. It is not surprising that the resistivity value decreases towards that of poly-Ge. To further explore other electrical properties including mobility and carrier concentration of the films, additional Hall measurements would be necessary.

## 5.5 Summary

Ge-rich poly-SiGe:H films have been fabricated by *in situ* sputter-deposition in an Ar and

hydrogen mixture. The influence of the Si fraction on the surface morphology, structural, optical, and electrical properties of the films was investigated. Firstly, with the decrease of Si fraction  $x$  from 0.246 to 0.048, the RMS roughness increases monotonically from 2.87 to 6.01 nm. The increase of roughness values is associated with the increasing crystallinity level of the films concluded by XRD and Raman measurements. Secondly, with decreasing  $x$  from 0.246 to 0.048, the grain size increases from ~52 nm to ~132 nm. Thirdly, the influence of the decreasing Si fraction in terms of optical properties is multifold, including: (i) UV-VIS reflectance reduction and a shift of “E1” peak towards that of Ge; (ii) transmittance reduction in the range between ~900 to 600 nm; (iii) narrowed band gap of the films from ~1.07 eV for the  $\text{Si}_{0.246}\text{Ge}_{0.754}\text{:H}$  film to ~0.78 eV for the  $\text{Si}_{0.048}\text{Ge}_{0.952}\text{:H}$  film. Fourthly, the decreasing Si fraction results in a dramatic decrease of the resistivity of the films, not only attributed to the higher Ge content but also to the higher degree of crystallinity of the films. A paper arising from this chapter has been published in Applied Surface Science (Tsao et al. 2011b).

## CHAPTER

# 6

## Hetero-epitaxial Growth of Thin Relaxed Ge Layers on Si Substrates

---

- *Overview*
- *Literature review*
- *Experiment*
- *Results and discussion*
- *Summary*

### 6.1 Overview

This chapter further extends the research scope into the hetero-epitaxial growth of thin relaxed Ge layers on Si substrates by using RF magnetron sputtering. The growth of crystalline Ge layers on Si substrates has attracted great interest because of the variety of potential applications, such as in high speed photodetectors and solar cells. For the latter application, the crystal Ge layers may act as crystal Ge virtual substrates to replace relatively expensive Ge wafers, on which GaAs layers are epitaxially grown. However, the epitaxially grown Ge layer would be strained when its thickness is less than a critical

thickness, below which the epitaxial Ge layer normally adapts its lattice constant to that of the underlying Si substrate. In order to work as Ge virtual substrates, the grown Ge layers have to be beyond the critical thickness for plastic strain relaxation, resulting in inevitable threading dislocations forming at the Ge/Si interface, owing to the 4.2% lattice mismatch between Ge and Si materials. In this chapter, the growth of the hetero-epitaxial Ge films on Si substrates by using RF magnetron sputtering will be investigated followed by the formation of hetero-junctions. A literature review will be firstly given in Section 6.2. The experimental details for growing the hetero-epitaxial Ge layers on Si and fabricating the hetero-junctions will be provided in Section 6.3. Subsequently, the results and discussion will be presented in Section 6.4. Finally, in Section 6.5, a summary concludes the work.

## **6.2 Literature review**

To obtain crystal Ge layers on Si with low threading dislocation density, molecular beam epitaxy (MBE) and ultrahigh vacuum chemical vapor deposition (UHV-CVD) are conventionally employed. Recently, low-energy plasma-enhanced chemical vapor deposition (LEPECVD) (Kaenel 2007) has been used as an additional approach for growing Ge layers on Si. Various growth techniques (Brasen et al. 1993; Currie et al. 1998; Fitzgerald 2000; Li et al. 1998) effective in reducing threading dislocation density have been developed.

One of these growth techniques is the use of a graded  $\text{Si}_{1-x}\text{Ge}_x$  buffer region. As Si is miscible with Ge over the whole content range between  $x=0$  and 1, the Ge content can be gradually increased from  $x=0$  to a certain value to lessen dislocation interaction, and thus

lead to lower threading dislocation densities (Brasen et al. 1993). The preferably compositional grading of Ge concentration is 10% per 1 $\mu$ m to ensure low threading dislocation densities (Li et al. 1998). However, the requirement of such an extra SiGe graded buffer layer of up to 10  $\mu$ m thickness, if the Ge content varies from 0% to 100%, raises the fabrication cost because of the generally low deposition rate used in MBE or UHV-CVD. In addition, an intermediate chemical mechanical polishing (CMP) step may be needed to improve the surface quality and lower the threading dislocation density (Currie et al. 1998; Fitzgerald 2000), leading to an extra cost.

An improved growth technique is the use of two or more thin (0.5-0.8  $\mu$ m) SiGe intermediate layers prior to the growth of Ge in a UHV-CVD system (Chang et al. 2007; Luo et al. 2003; Yang et al. 2004). In this method, the upwards propagating dislocations from the first layer can be bent and terminated effectively by the formed strained interfaces between the intermediate layers. A major advantage of this technique over the previous approach using the Si<sub>1-x</sub>Ge<sub>x</sub> graded buffer layer is that the total epitaxial thickness can be reduced to below 3  $\mu$ m, and thus lower the fabrication cost.

Another technique is the cyclic thermal anneal between 700-900°C of Ge directly epitaxially grown on Si substrates deposited in a two-step UHV-CVD system, which has been shown to effectively reduce the threading dislocation density in the epitaxial layer (Luan and Kimerling 2003; Luan et al. 1999; Wada et al. 2004). This technique avoids the need of the SiGe buffer layer.

Flatness of the hetero-epitaxial Ge is also desirable, in addition to low threading dislocation density. To obtain a Ge layer with low surface roughness value, a surfactant is commonly used to suppress island formation during growth (Sakai and Tatsumi 1994). Three-dimensional islanding following layer-by-layer growth, known as

Stranski-Krastanow growth, is a typical mode of Ge growth on Si, associated with the 4.2% lattice mismatch between Ge and the underlying Si (Eaglesham and Cerullo 1990; Sakai and Tatsumi 1994). The use of various elements, Sb (Copel et al. 1989), As (Copel and Tromp 1991), Te (Higuchi and Nakanishi 1991), Bi (Sakamoto et al. 1993), and H (Kahng et al. 1998; Sakai and Tatsumi 1994) as surfactants has been extensively studied for Ge growth on Si substrates. It is well accepted that the suppression of island formation by a surfactant may result in a layer-by-layer growth mode throughout growth.

Despite the high quality of crystal Ge films obtained, the aforementioned MBE and CVD based methods are too expensive to be applied in producing low-cost solar cells, of which the energy conversion efficiency and fabrication cost are most critical. To reduce the fabrication cost, sputtering, an environment friendly, economical, and simple deposition technique, is one of the possible solutions. Sputtering avoids the requirement for a UHV system. Also avoided is the use of expensive and extremely toxic germane, the precursor of Ge. In addition, a sputter system itself is well known to be relatively cheap in contrast with MBE and CVD systems. By sputtering, a high quality epitaxial Si film may be obtained at low temperature (Yuji and Sung 2005).

Similarly, it is possible to grow thin relaxed single crystalline Ge heteroepitaxial layers on Si substrates by sputtering. Although a very recent work reported that high quality polycrystalline Ge films on Si (100) substrate were obtained by DC-pulsed magnetron sputtering (Pietralunga et al. 2009), it has been known that by sputter deposition, single crystal semiconductor could be grown under suitable deposition condition, for example, by controlled use of low energy particle bombardment (Greene and Eltoukhy 1981). An early report (Aleksandrov et al. 1974) has demonstrated the heteroepitaxial growth of Ge on (111) Si substrates using a DC triode sputter system at a base pressure of  $10^{-7}$  Torr.

However, the processes involved an extra sputtering of Si from a separate Si target, followed by a heating process at 1300°C for 10-20 minutes to reduce unsaturated hydrocarbons. Another example is that Bajor et al. demonstrated the growth of high quality crystal Ge on (100) Si substrate by RF diode sputtering at 470°C at a base pressure of  $\sim 10^{-7}$  Torr (Bajor et al. 1982). By this RF diode sputter deposition, a  $\sim 200$  nm thick compositional graded junction at the lattice mismatched interface between the Ge layer and Si substrate was provided by low-energy ion bombardment of the substrate and of the growing film during deposition. This compositionally mixed interface and enhanced diffusion due to ion bombardment led to an annihilation of inclined misfit dislocations in the graded region (Bajor et al. 1982). The results discussed above imply the possibility of growing relaxed single crystalline Ge heteroepitaxial layers with a thickness greater than  $\sim 200$  nm on Si substrates by sputtering.

For sputter-deposition, Si surface contamination may influence the crystalline quality of Ge films grown, as for the cases of both evaporation and chemical vapor deposition (Bajor et al. 1982). High level oxygen can incorporate into sputter-deposited films, just from the residual gas in the vacuum chamber (Jelenkovic et al. 2000). The oxygen can reduce adatom mobilities and hence impact the structural properties of the films (Thornton 1986). Hydrogen has been known to prevent adsorption of contaminants by saturating surface dangling bonds and hydrogen ions may play an important role in controlling the morphology of semiconductor surfaces (Horn et al. 1991). Therefore, an adequate employment of hydrogen in a sputter-deposition may further improve the quality of the grown layers. This chapter investigates fabricating hetero-epitaxial growth of thin relaxed Ge layers on Si substrates by using RF magnetron sputtering and briefly explores the performance of boron-doped p-type Ge/n-type Si hetero-junctions.

### 6.3 Experiment

**Table 6.1:** Summary of the details of wet chemical treatment procedure

Purpose	Process	description
Organic residues removal	Piranha	<ul style="list-style-type: none"> <li>● Prepare a mixture of H<sub>2</sub>SO<sub>4</sub>(96%):H<sub>2</sub>O<sub>2</sub>(30%)=1:1 (Volume)</li> <li>● Soak wafer for 15 minutes in the solution and then rinse the wafer for 5 min in DI water.</li> </ul>
Organic contamination removal	RCA1	<ul style="list-style-type: none"> <li>● Heat a mixture of H<sub>2</sub>O:H<sub>2</sub>O<sub>2</sub>(30%):NH<sub>4</sub>OH(27%) =5:1:1 (Volume) to 75°C</li> <li>● The solution is ready for use when it bubbles vigorously.</li> <li>● Soak wafer for 10 minutes in the solution and then rinse the wafer for 5 min in DI water.</li> </ul>
Ionic and metallic contamination removal	RCA 2	<ul style="list-style-type: none"> <li>● Heat a mixture of H<sub>2</sub>O:H<sub>2</sub>O<sub>2</sub>(30%):HCl(37%) =5:1:1 (Volume) to 75°C</li> <li>● The solution is ready for use when it bubbles vigorously</li> <li>● Soak wafer for 10 minutes in the solution and then rinse the wafer for 5 min DI water.</li> </ul>
Oxide removal	HF dip	<ul style="list-style-type: none"> <li>● Dip the wafer for 10 s in 5 % HF solution, then rinse for 15-30 seconds in DI water.</li> </ul>

An AJA ATC2200 RF magnetron sputtering system equipped with a substrate holder heated by a quartz halogen lamp heater was used for hetero-epitaxial growth of Ge layers. The base pressure of the sputter-deposition chamber was less than  $6.5 \times 10^{-7}$  Torr. Si substrates were cleaned by a standard wet chemical treatment procedure, consisting of Piranha, RCA1 and RCA2, HF dip, DI water rinse for 15-30 seconds in turn. Table 6.1

summarizes the details of wet chemical treatment procedure. After the cleaning procedure, the Si substrate was immediately loaded into a load lock chamber. The substrate was then transferred into the sputter-deposition chamber when the vacuum of the load lock reached a pressure of less than  $4 \times 10^{-6}$  mBar, reducing the air potentially introduced into the chamber as much as possible. The substrate temperature in the sputter-deposition chamber was increased to approximately 500°C. The substrate was baked out at 500°C in hydrogen atmosphere (1.2 mTorr) for 15 minutes. After the pre-deposition processes, 3 series of experiments have been conducted.

### **6.3.1 The growth of hetero-epitaxial Ge films on Si**

300nm thick Ge layers were deposited onto Si (100) substrates by sputtering a 2" intrinsic Ge target (99.999% purity) in a mixture of Ar (15 sccm) and H<sub>2</sub> (10sccm) with a process pressure of 1.5mTorr at 500°C and 400°C, respectively. A 70 nm thick SiO<sub>2</sub> cap layer was then deposited on the epitaxial Ge layer at 200°C in an Ar atmosphere of 1.5 mTorr. The deposition of the cap layer was intended to prevent Ge loss during the potential post thermal annealing process. The Ge deposition rate was monitored by a crystal deposition monitor. Substrates were rotated at 30 revolutions per minute during deposition to ensure the uniformity of the films. The temperature calibration data were supplied by the manufacturer of the sputter system and measured with a Si wafer as described in Chapter 1. After the sputter-deposition, the sample was unloaded when substrate temperature naturally cools down to about 80°C to minimize the rate of formation of tensile strain due to the larger linear thermal expansion coefficient of Ge ( $5.8 \times 10^{-6} \text{ K}^{-1}$ ) compared to that of

Si ( $2.6 \times 10^{-6} \text{ K}^{-1}$ ). Except for TEM measurements, the  $\text{SiO}_2$  cap layers of the samples were removed by HF dip prior to the subsequent characterizations.

The surface morphology of the epitaxially grown Ge films was analysed by optical microscopy and AFM. The AFM measurements were performed using the tapping mode (Digital Instruments 3000). The scan area was  $2 \mu\text{m} \times 2 \mu\text{m}$  while the scan rate was 0.37 Hz. The structural properties of the films were examined by TEM and XRD measurements. XTEM (JEOL-3000F) was operated at 300 kV. XRD measurements were performed (PANalytical's X'Pert Pro materials research diffraction system) at a voltage of 45 kV and a current of 40 mA, using Cu  $K\alpha$  radiation ( $\lambda = 1.54 \text{ \AA}$ ). Electron backscattered diffraction (EBSD) measurements were used to further confirm the finding, that epi-Ge on (100) Si wafer substrate is single crystal. As measurements were conducted on the top surface of the epi-layer, sample preparation was minimal, requiring only to cleave a  $\sim 4.6$  by 10 mm section and to mount on a 70 tilt stub with a double sided conductive carbon tape. The EBSD measurements were carried out in a JEOL JSM7001F at a beam-energy of 10 keV.

### **6.3.2 The fabrication of Ge/ Si hetero-junctions**

As the success of heavily p-type doping of poly-Ge:H films on glass by co-sputtering Ge and boron has been demonstrated in Chapter 4, it is interesting to investigate fabricating p-type doped Ge/n-type Si hetero-junctions.  $0.3 \mu\text{m}$  heavily boron-doped Ge films were deposited on (100) Si wafer substrates by co-sputtering Ge and boron in Ar (or in a mixture of Ar and  $\text{H}_2$ ) at substrate temperatures, 370 and  $400^\circ\text{C}$ . The Ar flow was kept at 15 sccm with the addition of  $\text{H}_2$  at 10 sccm. The amount of incorporated B was controlled

by fixing the input power ( $P_B$ ) for sputtering a 2 inch B target at 55 W. Please note this amount of B had resulted in heavily p-type doping of poly-Ge:H films as reported in Chapter 4. During deposition the pressure in the chamber was kept at 1.5 mTorr. The resistivity of the Si substrates is 1-10  $\Omega$ -cm (i.e.  $4.83 \times 10^{15}$ - $4.41 \times 10^{14}$   $\text{cm}^{-3}$  doping) with a thickness of 500  $\mu\text{m}$ . The structural properties of the films were examined by XRD measurements, the details of which are the same as given earlier. The open circuit voltage ( $V_{OC}$ ) of the fabricated hetero-junctions were measured by a fully computer-controlled solar cell I-V tester, named "DarkStar" (Bowden 1995), under 1-sun illumination.

## **6.4 Results and discussion**

### **6.4.1 The hetero-epitaxial Ge films on Si**

- **Surface morphology**

Optical microscopy was used to examine the surface morphology of the epitaxially grown Ge films. Visible surface scattering of the sample deposited at 500°C is observed, similar to that observed from the hydrogenated Ge films sputtered on double polished Si wafer prepared for IR absorption measurements, as reported in Chapter 3. The surface scattering is attributed to the effect of the molecular hydrogen, owing to the surface desorption of hydrogen atoms into internal voids. With decreasing substrate temperature to 400°C, no more surface scattering is observed. Figure 6.1 compares the optical microscope images of the samples deposited at 400°C and 500°C. The images indicate a decrease of substrate temperature can effectively avoid surface scattering. Therefore, the following discussion will focus on the samples deposited at 400°C.

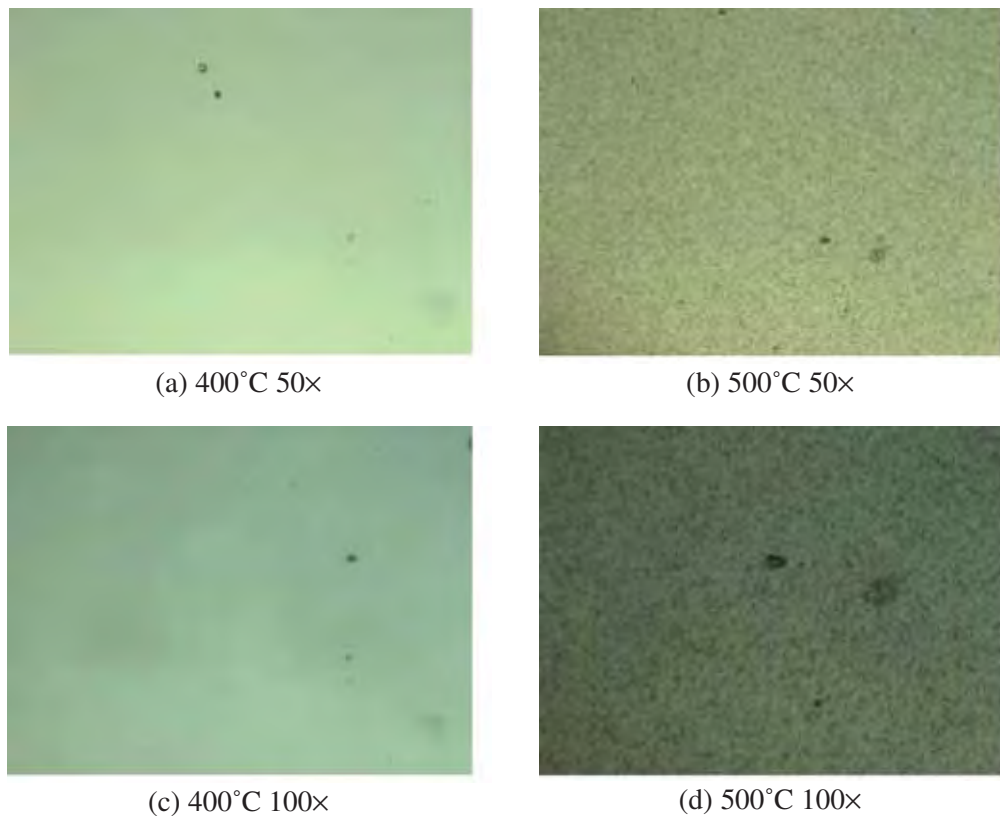


**Figure 6.1:** Optical microscopy images of epitaxially grown Ge films on (100) Si substrate sputtered in a mixture of Ar and H<sub>2</sub>.

The surface morphology of the epitaxial Ge layer deposited at 400°C was also analyzed by AFM. Figure 6.2 shows typical (a) 3 D and (b) 2 D AFM images (2  $\mu\text{m}$   $\times$  2  $\mu\text{m}$ ) of an epitaxial Ge layer on Si (100) sputter-deposited by the present method, respectively. The RMS roughness value of the Ge layer surface is 0.564 nm. The low level of surface roughness indicates the Stranski-Krastanow growth of the epitaxial Ge layer is highly suppressed by this method. The resultant RMS roughness value is lower than those (about 1nm) obtained by Luan et al. (Luan and Kimerling 2003) and Kaenel (Kaenel 2007) , respectively.

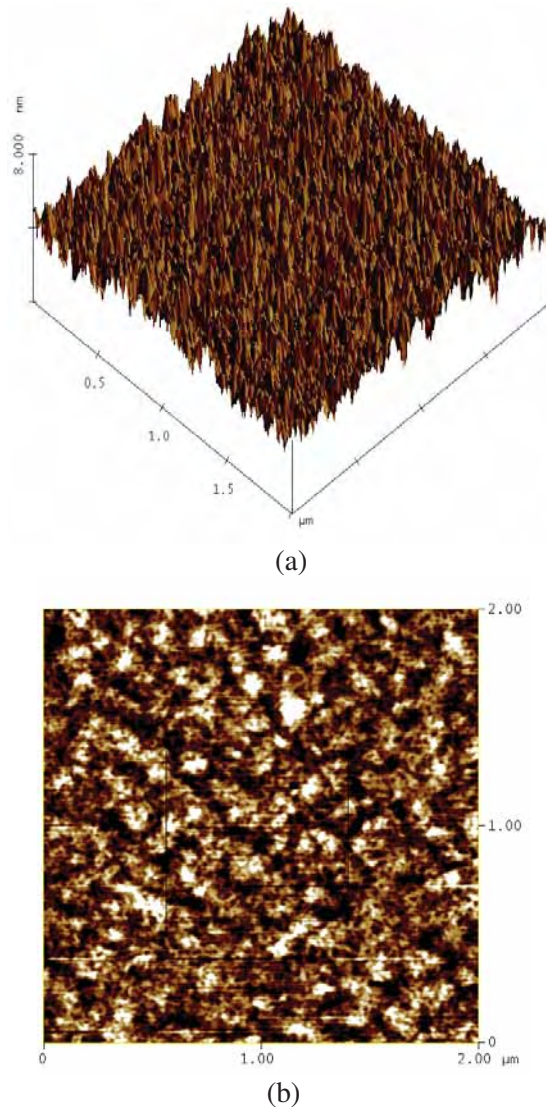
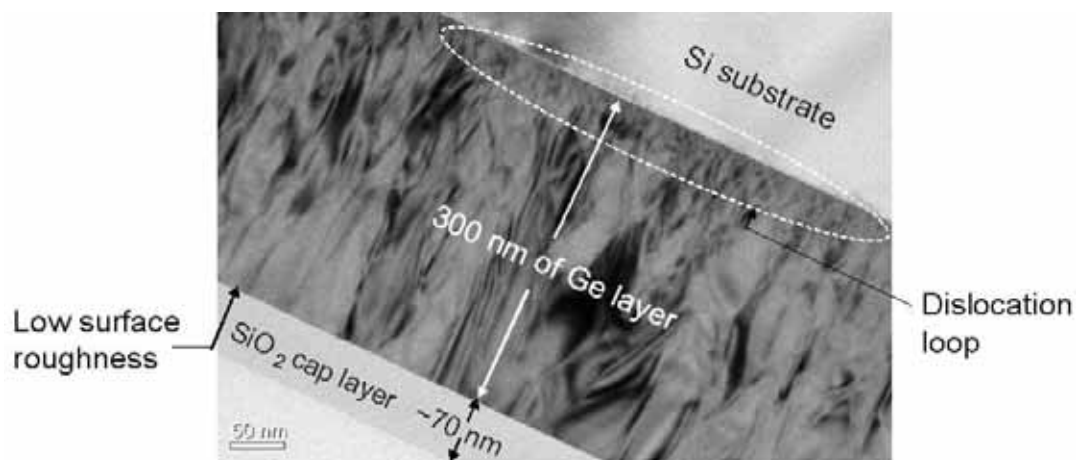


**Figure 6.2:** Typical atomic force microscope (AFM) images ( $2\ \mu\text{m}\times 2\ \mu\text{m}$ ) of an epitaxial Ge layer on Si (100) sputter-deposited at  $400^\circ\text{C}$  (a) 3 dimensional (D), (b) 2D. The root-mean-square (RMS) roughness value is 0.564 nm.

- **Structural properties**

The structural properties of the epitaxial Ge layer were firstly explored by XTEM measurements. Figure 6.3 (a) and (b) show the cross-sectional TEM micrographs of the sample having an about 300 nm thick Ge epitaxial layer, *in situ* capped by a  $\sim 70$  nm thick

SiO<sub>2</sub> layer. As shown in Figure 6.3 (a), a dislocation loop is generated and located near the interface due to the lattice mismatch. Also note the threading dislocation density is gradually reduced towards the Ge surface, very likely because of the annihilation of inclined misfit dislocations due to the compositionally mixed interface and enhanced diffusion due to ion bombardment during deposition. In addition, the surface roughness of the Ge epitaxial layer shown in Figure 6.3 (a) is quite low, in agreement with the AFM images shown in Figure 6.2. It is evident that the surface is much flatter than those obtained by Akbar *et al.* (Akbar *et al.* 1993). Figure 6.3 (b) shows the take-up of the lattice mismatch in a very narrow defected region near the interface with clear, but differently spaced and relaxed, lattice planes apparent in both Si and Ge materials away from the interface.



(a)

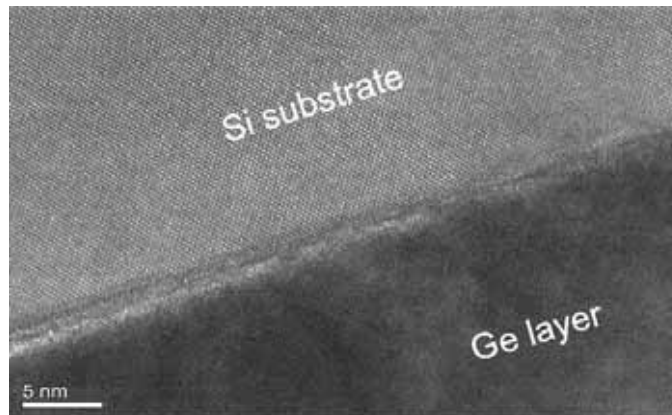


**Figure 6.3:** Cross-sectional high resolution transmission electron microscope (XTEM) micrographs of a typical sample, having a total thickness of about 300 nm of the Ge epitaxial layer, *in situ* capped by a ~70 nm thick SiO<sub>2</sub> layer. (a) A dislocation loop near the interface and gradually reduced threading dislocation density towards the Ge surface are visible. (b) The take-up of the lattice mismatch in a very narrow defected region near the interface with clear, but differently spaced and relaxed, lattice planes apparent in both Si and Ge materials away from the interface.

The structural properties of the epitaxial Ge layer were also examined by XRD measurements. Figure 6.4 shows the XRD pattern of the epitaxial Ge layer on Si (100) sputter-deposited at 400°C and a reference Ge (100) wafer measured in the range between 15° and 90° of 2θ degree. The absence of the (111), (220), (311), (331), (422) diffraction peaks at around 27°, 45°, 53°, 72°, and 83° but the presence of the (400) diffraction peak at around 66° indicates that the epitaxial Ge layer is likely single crystal. Note the epitaxial Ge layer has relaxed as the position of the (400) diffraction peak of the epitaxial Ge layer at around 66° is the same as that of the reference Ge wafer but is distinct from that of the underlying Si substrate.

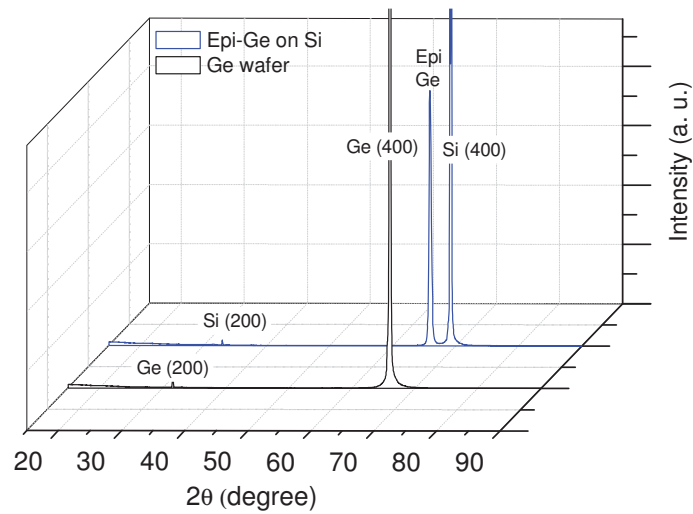
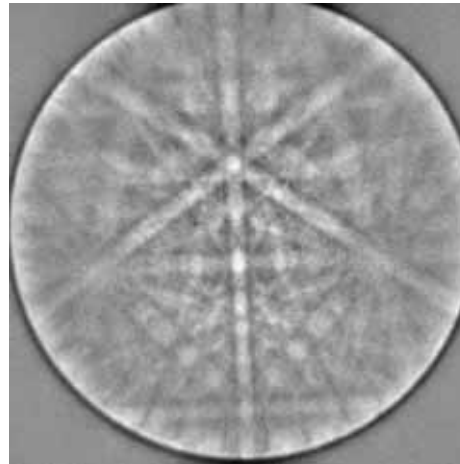
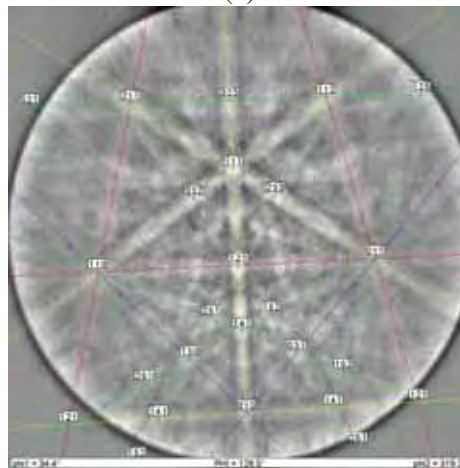


**Figure 6.4:** X-ray diffraction (XRD) pattern of an epitaxial Ge layer on Si (100) sputter-deposited at 400°C and a reference Ge (100) wafer.

To further confirm the crystallinity of the epitaxial Ge layer, EBSD measurements were carried out. Figure 6.5 shows (a) A typical EBSD pattern of the sample and (b) Miller indices of the EBSD pattern. Clear Kikuchi lines shown in Figure 6.5 (a) are evident in the pattern, indicating the epitaxial Ge layer is single crystalline. The Miller indices of the pattern shown in Figure 6.5 (b) is a sign that the epitaxial Ge layer is of [100] orientation. This result is in agreement with the XRD data.



(a)

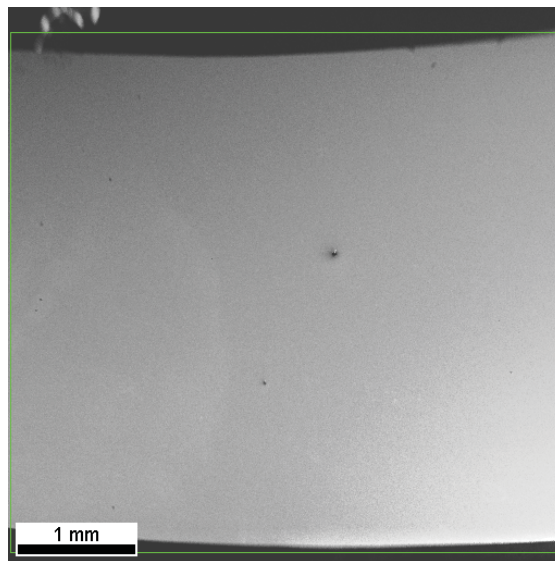


(b)

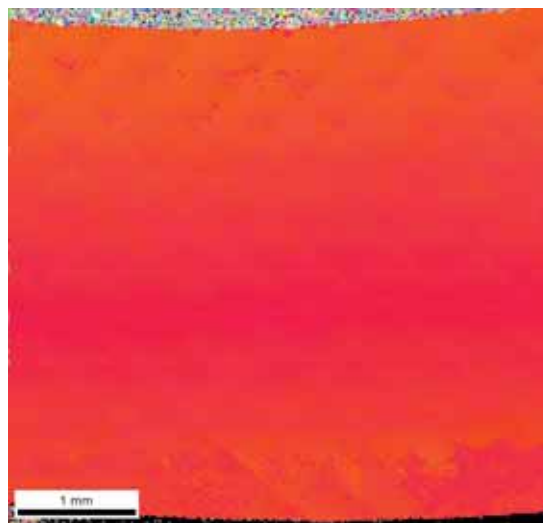
**Figure 6.5:** (a) A typical electron back-scattered diffraction (EBSD) pattern at the sample and (b) Miller indices of the EBSD pattern. The pattern indicates the epitaxial Ge layer is single crystal with (001) orientation.

Another technique, related to EBSD and widely used to identify the orientation of a thin film, is an inverse pole figure. Figure 6.6 shows: (a) An image of a 4.4 mm×4.6 mm area from the sample measured by SEM for reference. Note only the area confined by the green square is scanned; (b) Orientation distribution measured from 10 different locations (distance interval: 1mm) all over the sample, where all the 10 spots in green are located at

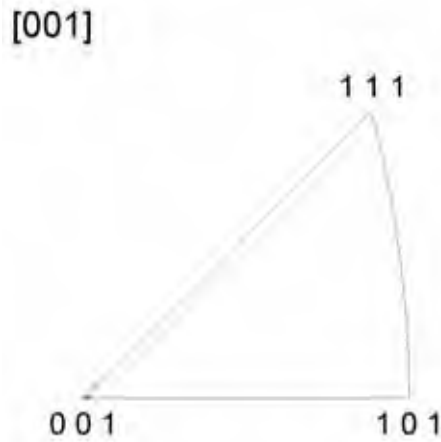
[001]; (c) A colour coded map of a 4.4 mm×4.6 mm measured area from the sample, indicating the Ge material within the measured area is all of [001] orientation according to the reference inverse pole figure of Ge [001] provided; (d) An inverse pole figure of Ge [001] is provided for reference. Note the colourful area at the top edge and the black area at the bottom edge are the areas out of the sample.



(a)



(b)



(c)

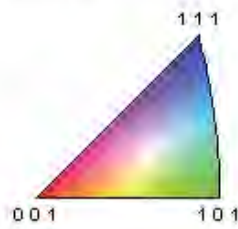
---

Gray Scale Map Type: <none>

---

Color Coded Map Type: Inverse Pole Figure [001]

Germanium




---

Boundaries: <none>

(d)

**Figure 6.6:** (a) An image of a 4.4 mm×4.6 mm area from the sample measured by SEM for reference. Note only the area confined by the green square is scanned. (b) A color coded map of a 4.4 mm×4.6 mm measured area from the sample. Note the colourful area at the top edge and the black area at the bottom edge are the areas outside of the sample. (c) Orientation distribution measured from 10 different locations (distance between each is 1 mm) all over the sample. All the spots in green are located at [001] (d) An inverse pole figure of Ge [001] is provided for reference.

## 6.4.2 The Ge/Si hetero-junctions

- **XRD measurements**

As a simple and readily available tool in Solid State and Elemental Analysis Unit of UNSW, XRD was again used to examine the structural property of the epitaxial Ge layer. Figure 6.7 shows the XRD spectra of the heavily boron-doped epitaxially grown Ge films on (100) Si substrate wafers prepared using various deposition conditions. The absence of the (111), (220), (311), (331), (422) diffraction peaks at around  $27^\circ$ ,  $45^\circ$ ,  $53^\circ$ ,  $72^\circ$ , and  $83^\circ$  but the presence of the (400) diffraction peaks at around  $66^\circ$  indicates that the epitaxial Ge layers have high quality. In contrast with those deposited in Ar, the layers deposited in the mixture of Ar and H<sub>2</sub> at 370 and 400°C exhibit weaker (400) diffraction peaks. This may be attributed to a reduction of energetic particle bombardment effects led by the inclusion of hydrogen during deposition, as documented in Chapter 3. The nearly vanishing (400) diffraction peak of the layer deposited in the mixture of Ar and H<sub>2</sub> at 370°C implies the total energy supplied from this low temperature and the energetic particle bombardment is insufficient to achieve a high quality single crystal Ge layer. In addition to the information in Section 6.4.1.1, a window of substrate temperature between 370°C and 500°C exists.

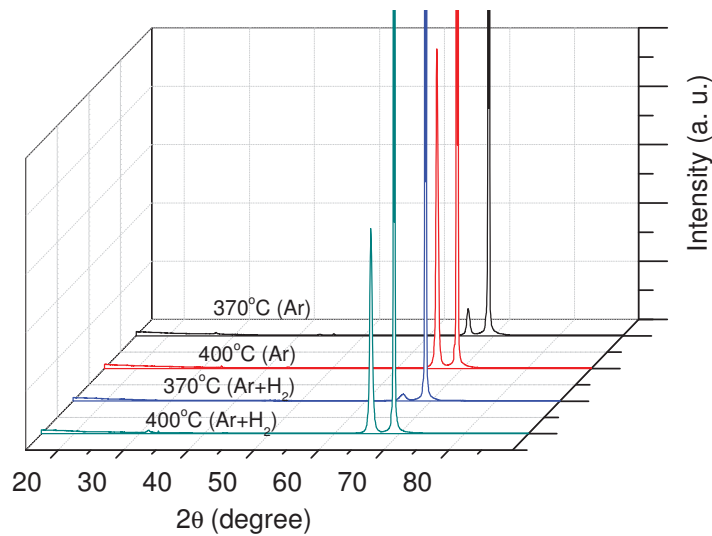


**Figure 6.7:** XRD spectra of the heavily boron-doped epitaxially grown Ge films on (100) Si substrate wafers prepared using various deposition conditions.

- **$V_{OC}$  measurements**

The performance, in terms of  $V_{OC}$ , of 4 hetero-junctions fabricated at 4 different conditions, i.e. at 370 and 400°C as well as in Ar and in a mixture of Ar and  $H_2$ , was measured by DarkStar under 1-sun illumination. Figure 6.8 shows the  $V_{OC}$  values of the epitaxially grown Ge films on Si substrate illuminated on the Ge as well as Si side. The structure of the hetero-junctions is illustrated in Figure 6.9, which is a natural mesa structure due the partial coverage of the substrate holder on the edges of the Si wafer substrates.

As shown in the figure, the general trends, that the Ge/Si heterojunctions generate higher  $V_{OC}$  when illuminated on Ge side, can be mainly attributed to the significantly shallower junction locations of 0.3  $\mu\text{m}$  in contrast with 500  $\mu\text{m}$  when illuminated on Si side. This is because the photo flux within a solar cell material falls off exponentially with increasing

distance from the illuminated surface. In other words, the spatially uniform photogeneration  $G(x)$  is strongly peaked at the illuminated surface (Green 1982).

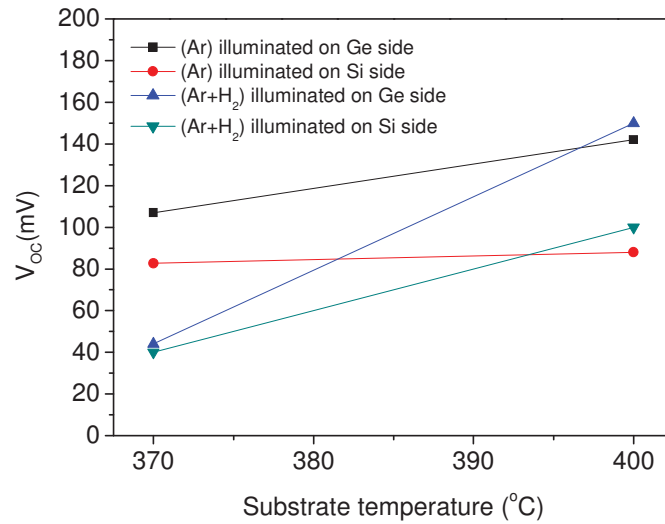


**Figure 6.8:**  $V_{oc}$  of the epitaxially grown Ge films on Si substrate sputtered at various conditions illuminated on the Ge as well as the Si side.

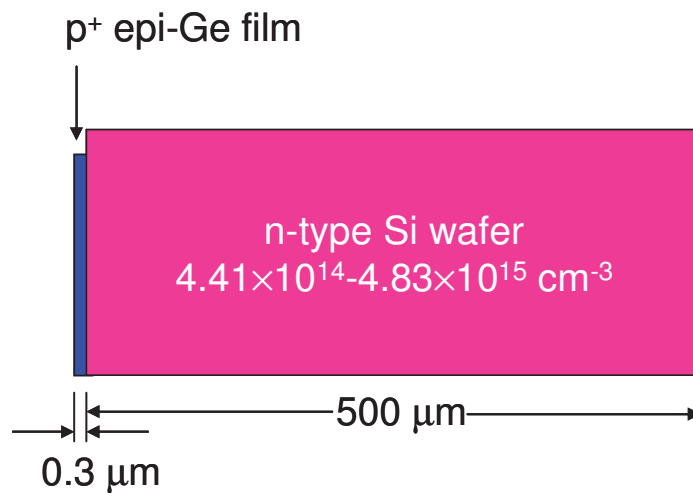


**Figure 6.9:** Hetero-junction structure, which is a natural mesa structure due the partial coverage of the substrate holder on the edges of the Si wafer substrates: 0.3  $\mu\text{m}$  heavily boron-doped epitaxially grown Ge on 500  $\mu\text{m}$  Si wafer substrate. Note: the thickness of the 0.3  $\mu\text{m}$  Ge layer is exaggerated.

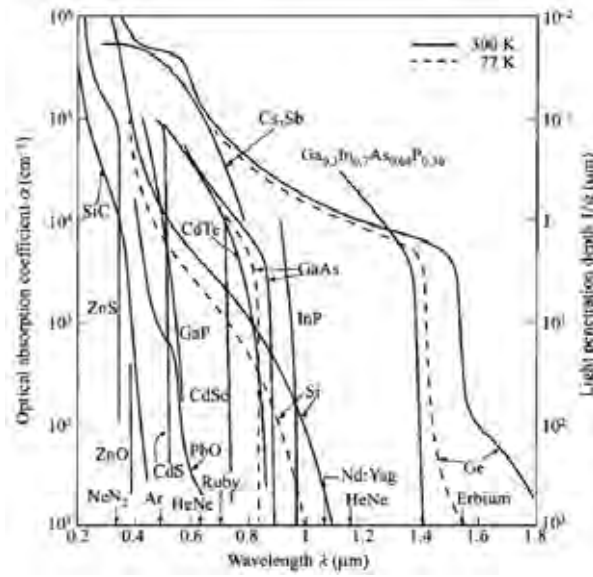


**Figure 6.10:** Optical absorption coefficients for various photo-detector materials (Sze and Ng 2007).

The shallower junction will result in a higher collection probability of the light-generated minority carriers,  $f_c(x)$ , which decreases exponentially with increasing distance of the point of generation away from the edge of the junction-depletion region (Green 1982), according to the equations as follows:

$$J_L = q \int_0^\infty G(x) f_c(x) dx \tag{6.1}$$

$$V_{oc} = \frac{kT}{q} \ln \left( \frac{J_L}{J_o} + 1 \right) \tag{6.2}$$

The shallower junction will hence result in a higher light-generated current  $J_L$ . As a result, the  $V_{oc}$  is higher when the hetero-junctions are illuminated on the Ge side. It should be noted that although Ge has a much narrower band gap and has a stronger optical absorption coefficient than Si (see Figure 6.10), the thickness of the Ge layer is only 0.3  $\mu\text{m}$  insufficient to absorb light with wavelength  $>0.8 \mu\text{m}$ .

For the films deposited at 370°C, the  $V_{OC}$  of the sample deposited in a mixture of Ar and  $H_2$  is lower than that deposited in Ar regardless of the illuminated side, mainly attributed to the poor crystallinity of the sample as revealed by XRD measurements earlier. Interestingly, in contrast, with an increase of substrate temperature to 400°C, the  $V_{OC}$  of the sample deposited in a mixture of Ar and  $H_2$  is higher than that deposited in Ar regardless of the illuminated side. It is noted that for those deposited at 400°C, the sample deposited in Ar exhibits a stronger (400) diffraction peak as concluded by XRD data. Although the reason for this apparent contradiction is not clear yet, it is speculated that the hydrogen might benefit the reduction of dislocation density at the interface between the Ge layer and its underlying Si substrate, leading to lower dark saturation current and thus higher  $V_{OC}$ . To support this point, further systematically experimental studies and various characterizations would be required.

It is worth mentioning another interesting finding from the experiments on hetero-junctions: the successful formation of low resistance  $p^+Ge/n^+$  Si tunnel junctions. By fabricating 0.3  $\mu m$  heavily boron-doped Ge layers on  $n^+/n/n^+$  Si (100) instead of the n Si (100) substrates by co-sputtering Ge and boron in a mixture of Ar and  $H_2$  at 400°C,  $p^+Ge/n^+$  Si tunnel junctions may form successfully. The  $n^+/n/n^+$  Si (100) substrates were prepared by thermal diffusion of phosphorus into the front and back surfaces of the 500  $\mu m$  thick Si (100) wafers followed by a HF dip. The sheet resistance of the  $n^+$  layer was  $\sim 10 \Omega/\square$ . 0 mV of  $V_{OC}$  obtained from the sample under 1-sun illumination while ohmic contact ( $0\Omega$  between the Ge layer and the Si substrate measured from the mesa structure regardless of polarity) are the evidence of the successful formation of a  $p^+Ge/n^+$  Si tunnel junction. This experiment has been carried out for 3 times to ensure the repeatability of the experiments. The fabrication process of the  $p^+Ge/n^+$  Si tunnel junctions is simple but

would be useful when a contact layer is needed to electrically connect two sub-cells of tandem cells.

## 6.5 Summary

This chapter provides a novel method, capable of producing thin relaxed single crystal Ge layers on Si with low fabrication cost, making the resultant Ge layer work as a virtual substrate for III-V material growth for possible solar cell application. For producing solar cells, which are large area devices generating green power, fabrication cost and low environment impact are critical, in addition to device performance.

RF magnetron sputtering is known as an economical (non-UHV), environment friendly, and simple deposition technique. In the present work, the required base pressure is less than  $6.5 \times 10^{-7}$  Torr, much higher than those required in aforementioned MBE or CVD based techniques, resulting in a lower fabrication cost. In addition, in contrast with CVD based techniques, involving costly and extremely toxic germane gas, a sputtering technique uses Ge target instead of germane gas, not only economical but also more environment friendly. Finally, the capital expenditure of a RF magnetron sputter system itself will be lower than MBE or CVD based systems.

It has been demonstrated that by optimizing the deposition parameters, a 300 nm high quality epitaxial Ge thin layer, possibly containing a compositional graded junction at the lattice mismatched interface between the Ge layer and Si substrate and thus having low threading dislocation density as well as low surface roughness at the fully relaxed layer surface, may be *in situ* obtained at 400°C at 1.5 mTorr in a mixture of argon and hydrogen. This novel technique is apparently a different approach from earlier work and avoids the

need of (1) a several  $\mu\text{m}$  thick SiGe graded buffer region, (2) an intermediate CMP step, and (3) any additional thermal annealing processes. Table 6.2 lists representative patent literature. Also demonstrated are the initial results from Ge/Si hetero-junctions. A patent application arising from this chapter has been submitted. Additionally, a grant application in the form of an Australia Research Council Linkage Project Titled “Supercharged Silicon Wafer Tandem Solar Cells Using Virtual Germanium Substrates” has been submitted on 19 November 2010 to further investigate the potential of this approach.

**Table 6.2:** Representative patent literature about hetero-epitaxial growth of Ge on Si

Title	Patent	Deposition method	Remark	Year
1.Heteroepitaxy of germanium silicon on silicon utilizing alloying control	US 4,357,183	RF Sputtering	A Ge or SiGe amorphous film is sputter-deposited on a Si wafer followed by RTA. $T_{\text{anneal}} = \sim 1090^\circ\text{C}$	1982
2.Method for epitaxially growing $\text{Ge}_x\text{Si}_{1-x}$ layers on Si utilizing Molecular Beam Epitaxy	US 4,529,455	MBE	Initial Pressure $< 2 \times 10^{-8}$ Torr $T_s = 550^\circ\text{C}$ ( $x > 0.5$ ) $T_s = 650^\circ\text{C}$ ( $0 \leq x \leq 0.5$ )	1985
3.Formation of epitaxial si-ge heterostructures by solid phase epitaxy	US 4,975,387	E-beam evaporator		1990
4.Method for making low defect density semiconductor heterostructure and devices made thereby	US 5,221,413	MBE or CVD	MBE: Pressure $< 10^{-9}$ Torr $T_s = 900^\circ\text{C}$ CVD: Pressure $< 10^{-7}$ Torr $T_s = 900^\circ\text{C}$	1993
5.Heteroepitaxial growth of germanium on silicon by UHV/CVD	US 5,259,918	UHV/CVD	Pressure $< 10^{-9}$ Torr $T_s = 300\text{-}375^\circ\text{C}$	1993
6.Low temperature ion-beam assisted deposition methods for realizing SiGe/Si heterostructure	US 5,633,194	Ion-beam assisted deposition	Pressure $< 2 \times 10^{-4}$ Torr $T_s > 280^\circ\text{C}$	1997
7.Process for obtaining a layer of single-crystal germanium or silicon on a substrate of single-crystal silicon or germanium, respectively	US 6,117,750	CVD	$T_s = 450\text{-}800^\circ\text{C}$	2000
8.Cyclic thermal anneal for dislocation reduction (Ge pi-grown on Si substrate)	US 6,635,110 B1	Two step UHV/CVD	1st step $T_s = 350^\circ\text{C}$ 2nd step $T_s = 600^\circ\text{C}$ Cyclic thermal annealing between $700$ and $900^\circ\text{C}$	2003

			Surface roughness=2 nm rms	
9. Abrupt pn junction diode formed using chemical vapor deposition processing	US 6,661,075 B2	PECVD	Epi-grow Si, Ge, SiGe, SiGeC at $T_s < 650^\circ\text{C}$	2003
10. Ge photodetectors	US 6,812,495 B2	UHV/CVD	$T_s = 700^\circ\text{C}$ Cyclic thermal annealing (10 cycles between 700 and 900°C)	2004
11. Nanoheteroepitaxy of Ge on Si as a foundation for group III-V and II-VI integration	US 2006/007 3681A1	UHV/MBE	Forming an interface layer on a portion of a substrate.	2006
12. Growth of GaAs epitaxial layers on Si substrate by using a novel GeSi buffer layer	US 7,259,084 B2	UHV/CVD		2007
13. Method for producing virtual Ge substrate for III/V-integration on Si(001) (mis-oriented $6^\circ$ towards $\langle 110 \rangle$ direction)	US 2007/023 1488A1	Low Energy PECVD	Deposition rate=5 nm/s Surface roughness=1 nm rms	2007
14. Epitaxial semiconductor deposition methods and structures (Ge or SiGe epi-grown on Si wafer)	US 2010/000 6024A1	Epsilon 3000 Single-Wafer Epitaxial Reactor (CVD)	Bake in hydrogen at $T=900^\circ\text{C}$ for 2 min. Deposition $T_s=350^\circ\text{C}$ Deposition rate=0.5- 5 nm/min Surface roughness=0.28 nm rms	2010
Present work		RF sputtering	Base pressure= $6.5 \times 10^{-7}$ Torr $T_s=400^\circ\text{C}$ (in Ar+H <sub>2</sub> ) Deposition rate=5 nm/min Surface roughness=0.564 nm rms	2010

# CHAPTER

# 7

## Conclusions, Original Contributions and Future Work

---

- *Conclusions*
- *Original Contributions*
- *Future Work*

### 7.1 Conclusions

The aim of this thesis was to develop high quality poly-Ge:H thin films as well as Ge-rich poly-SiGe:H alloys on glass, and hetero-epitaxially grown relaxed crystalline Ge layers on Si wafers for application in low cost monolithic tandem solar cells. The findings results from this study are summarized below.

#### 7.1.1 Poly-Ge and poly-Ge:H thin-films on glass by RF sputtering

The thesis firstly focused on the optimisation of high quality poly-Ge thin films. The structural, optical, and electrical properties of Ge thin films prepared by RF magnetron sputtering on glass substrates under various fabrication conditions were investigated.

Poly-Ge films *in situ* grown by sputter-deposition were found to have superior properties over those by *ex situ* SPC annealing. The influence of the  $T_s$  and  $T_{spc}$  on the structural properties of the films was investigated by Raman, XRD and UV-VIS reflectance measurements. The results from these characterization techniques all indicate the transition temperature from amorphous to polycrystalline is between 255°C and 280°C for *in situ* grown poly-Ge films, whereas the transition temperature is between 400°C and 500°C for films produced by SPC for a 20h annealing time. With increasing  $T_s$  and  $T_{spc}$ , the film structural properties characterized by Raman, XRD and UV-VIS reflectance spectra have the following features: (i) Raman FWHM decreases; (ii) XRD (111) peak becomes more pronounced; (iii) characteristic peaks of UV-VIS reflectance spectra become more similar to that of bulk crystalline Ge; and (iv) the RMS roughness of the films measured by AFM increases with increasing  $T_s$ . These results show improved crystalline properties with increasing  $T_s$  and  $T_{spc}$ . Compared to SPC films annealed at 600°C, *in situ* grown Ge films as deposited at a temperature of 450°C have better crystalline quality. The poor results for the SPC samples could stem from the defects and oxygen within the underdense films sputter-deposited at low temperature.

*In situ* hydrogenation further improved the quality of the sputter-deposited poly-Ge films. Revealed by Raman and XRD measurements, the inclusion of hydrogen leads to an increase of substrate temperature required to achieve crystalline Ge prepared by RF magnetron sputtering, which can be explained by the resultant reduction of energetic

particle bombardment effects. Despite the higher onset crystallization temperature required, the introduction of hydrogen reduces the tensile strain. Moreover, it leads to higher degree of crystalline perfection of the poly-Ge:H film sputter-deposited at 450°C compared to its non-hydrogenated counterpart. In addition, it also results in a different surface morphology.

The hydrogenation also altered the optical properties of the Ge films, which were correlated to the structural properties of the films caused by the change of substrate temperature. The hydrogen incorporated in the films leads to broadened band gaps of the films sputtered at different  $T_s$ . The wider band gaps of Ge:H films compared to those of Ge films may result from the substitution of Ge-Ge bonding and anti-bonding states by Ge:H states in the valence and conduction bands. As  $T_s$  increases, the difference in  $E_g$  due to the presence or absence of hydrogen becomes less pronounced. This may be because, with increasing  $T_s$ , the amount of hydrogen bonded in the films reduces. As a result, the largest increase level of band gap occurs in the films sputtered at 255° C and then descends with increasing  $T_s$ .

The dependence of the electrical properties of the Ge films on the structural properties was demonstrated as well. As the substrate temperature increased from 255 to 400°C, both Ge and Ge:H films first showed n-type conductivity with progressively increasing room-temperature dark resistivity that peaks about the type switch. Upon attaining p-type character the resistivity decreased rapidly with further increase in  $T_s$ . Accompanying these trends, the film grain orientation evolved from predominantly (220) to (111). The n-type conduction of Ge films deposited at low  $T_s$  may be attributed to incorporated impurities such as oxygen. Oxygen arising from plasma-dissociated water vapor is

generally the main culprit of unintentional n-type doping of sputter-deposited Ge films. At the onset crystallization temperatures, both the Ge and Ge:H films undergo step increases in resistivity, while remaining n-type. This resistivity increase might be due to the formation of isolated p-type crystalline grains which act to reduce the volume of the continuous n-type a-Ge network. The transition temperature marks the threshold where the crystalline grains form a percolating network, thus rendering the film p-type. The resistivity change of the sputtered films is strongly dependent on their degree of crystallinity attributed to the percolation effects of the crystalline grains. The n-type films exhibit extremely low mobility associated with the amorphous conduction pathway while the p-type films exhibit high mobility as the film material quality improves.

### **7.1.2 Controlled doping of poly-Ge:H thin-films on glass by RF sputtering**

The thesis subsequently demonstrated the potential of the *in situ* sputtered-deposited poly-Ge:H thin films for the applications in bottom cells by p-type doping with boron and n-type doping of phosphorus. Novel but low cost doping approaches have been developed. The effectiveness of the developed doping approaches was verified by characterizing the structural and electrical properties of doped Ge:H thin films.

P-type doped Ge:H films were prepared by *in situ* doping by co-sputtering Ge with B in argon and hydrogen plasma at 500°C. The dramatic drop of the resistivity of the films, caused by the addition of B, is evidence of successful activation of B dopant. The post annealing processes alter the structural and electrical properties of the films. The RTA at 550°C for 120s favors the structural properties of the films, and hence results in an

improvement of film mobility. In contrast, the higher temperature but lower duration RTA at 600°C for 60s enhances the activation of B dopants, especially in the heavily doped case, where a carrier concentration of  $1.21 \times 10^{20}$  atoms/cm<sup>3</sup> was obtained. The process temperature, far below the required diffusion temperature of B in Ge, makes the formation of shallow abrupt junctions possible. On the other hand, an approach for phosphorus *ex situ* doping of poly-Ge:H has been developed. Initial results indicate that n-type doping of sputter-deposited poly-Ge:H films was successful with this approach.

### 7.1.3 Ge-rich Poly-SiGe:H thin-films on glass by RF sputtering

Ge-rich poly-SiGe:H films have been fabricated by *in situ* sputtering-deposition in an Ar and hydrogen mixture. The influence of the Si fraction on the surface morphology, structural, optical, and electrical properties of the films was investigated. Firstly, with the decrease of Si fraction  $x$  from 0.246 to 0.048, the RMS roughness increases monotonically from 2.87 to 6.01 nm. The increase of roughness values is associated with the increasing crystallinity level of the films concluded by XRD and Raman measurements. Secondly, with decreasing  $x$  from 0.246 to 0.048, the grain size increases from ~52 nm to ~132 nm. Thirdly, the influence of the decreasing Si fraction in terms of optical properties is multifold, including: (i) apparent UV-VIS reflectance reduction and a shift of “E1” peak towards that of Ge; (ii) apparent transmittance reduction in the range between ~900 to 600 nm; (iii) narrowed band gap of the films from ~1.07 eV of the Si<sub>0.246</sub>Ge<sub>0.754</sub>:H film to ~0.78 eV of the Si<sub>0.048</sub>Ge<sub>0.952</sub>:H film. Fourthly, the decreasing Si fraction results in a dramatic decrease of the resistivity of the films, not only attributed to the higher Ge content but also to the higher degree of crystallinity of the films.

## 7.1.4 Hetero-epitaxial Growth of Thin Relaxed Ge Layers on Si Substrates

A novel method, capable of producing thin relaxed single crystal Ge layers on Si with low fabrication cost, has been developed. Thin relaxed Ge layers on Si substrates were hetero-epitaxially grown by using RF magnetron sputtering, known as an economical (non-UHV), environment friendly, and simple deposition technique. By optimizing the deposition parameters, a 300 nm high quality epitaxial Ge thin layer, possibly containing a compositional graded junction at the lattice mismatched interface between the Ge layer and Si substrate and thus having low threading dislocation density at the fully relaxed layer surface, was *in situ* obtained at 400°C at 1.5 mTorr in a mixture of argon and hydrogen. Compared with conventional approaches, which are generally MBE or UHV CVD based, this method avoids the need of: (1) a several  $\mu\text{m}$  thick SiGe graded buffer region; (2) an intermediate CMP step; and (3) any additional thermal annealing processes. The initial results of Ge/Si hetero-junctions and the successful formation of low resistance  $\text{p}^+\text{Ge}/\text{n}^+\text{Si}$  tunnel junctions by co-sputtering Ge with boron demonstrate the potential of this technology in PV applications.

## 7.2 Original Contributions

Several original contributions arising from this thesis are listed as follows:

### 7.2.1 Poly-Ge and poly-Ge:H thin-films on glass by RF sputtering

- Demonstration that the *in situ* grown poly-Ge films at 450 °C by RF sputtering exhibit significantly better crystalline quality than those RF sputter-deposited amorphous followed by solid-phase crystallization at 600 °C for 20 hours. Also demonstrated is that the crystalline quality can be further improved by *in situ* hydrogenation although the inclusion of hydrogen leads to an increase of substrate temperature required to achieve crystalline Ge layers owing to a resultant reduction of energetic particle bombardment effects.
- Demonstration *via* Raman, XRD and UV-VIS reflectance investigations that the substrate temperature  $T_s$  influences the crystalline properties of the *in situ* sputter-deposited Ge and Ge:H films.
- Demonstration the optical properties and electrical properties of the *in situ* sputter-deposited Ge and Ge:H films depend on the structural properties, owing to the influence of the substrate temperature  $T_s$ . The resistivity change of sputtered Ge films is strongly dependent on their degree of crystallinity attributed to the fact that n-type carriers likely caused by incorporated oxygen were compensated by p-type carriers likely associated with crystallographic defects.

### 7.2.2 Controlled doping of poly-Ge:H thin-films on glass by RF sputtering

- Development of a novel but low cost approach for heavily p-type doping of hydrogenated poly-Ge thin films by co-sputtering Ge with boron.
- Development of a novel but low cost approach for n-type doping of hydrogenated poly-Ge thin films by thermal diffusion of phosphorus by a post annealing process.

### 7.2.3 Ge-rich Poly-SiGe:H thin-films on glass by RF sputtering

- Demonstration *via* the investigation of the influence of the Si fraction on the surface morphology, structural, optical, and electrical properties that Ge-rich Poly-SiGe:H films prepared by RF sputtering may be suitable for use in solar cell applications.

### 7.2.4 Hetero-epitaxial growth of thin relaxed Ge layers on Si substrates

- Development of a novel method for producing thin relaxed single crystal Ge layers on Si with low fabrication cost by RF sputtering, making the resultant Ge layer work as a virtual substrate for III-V material growth for possible solar cell applications.
- Demonstration of the feasibility of a tunnelling junction formed by RF sputter-depositing heavily boron doped thin single crystal Ge layers on n<sup>+</sup>n Si wafers.

## 7.3 Future Work

The potential of RF sputter-deposited poly-Ge:H thin films as well as Ge-rich poly-SiGe:H alloys on glass, and hetero-epitaxially grown Ge layers on Si wafers for photovoltaic applications has been demonstrated in this thesis. Nevertheless, as more resources become available in the near future, such as PH<sub>3</sub> gas and cluster chambers for the RF sputter system, other work as listed below should be further investigated.

### 7.3.1 Controlled doping of poly-Ge:H thin-films on glass by RF sputtering

- Development of a novel but potentially low cost approach for *in situ* n-type doping of hydrogenated polycrystalline germanium thin films by sputter-depositing Ge in a mixture of Ar and PH<sub>3</sub> gas.
- Development of a novel p<sup>+</sup>n poly-Ge:H thin film solar cell on glass by the developed *in situ* p-type and n-type doping approaches .

### 7.3.2 Ge-rich Poly-SiGe:H thin-films on glass by RF sputtering

- Experimental study of an approach for heavily p-type doping of Ge-rich poly-SiGe:H thin films by co-sputtering Ge and Si with boron.
- Experimental study of an approach for *in situ* n-type doping of Ge-rich Poly-SiGe:H thin films by sputter-depositing Ge in a mixture of Ar and PH<sub>3</sub> gas.

### 7.3.3 Hetero-epitaxial growth of thin relaxed Ge layers on Si substrates

The study of hetero-epitaxial growth of thin relaxed Ge layers on Si substrates has resulted in a patent application being submitted. Based on this innovative technology, a 5-year ARC linkage project, titled “Supercharged Silicon Wafer Tandem Solar Cells Using Virtual Germanium Substrates” has been submitted on 19th November 2010. The project aims to exploit this technology by the development of a new generation of silicon

wafer cell technology, with the performance of the silicon cell “supercharged” by the deposition from the chemical phase or by physical vapour deposition of one or more thin layers of high performance III-V cells on its surface.

---

---

## Publications Arising from this Thesis

---

### A. Papers in refereed scientific and technical journals

- [1] **C.-Y. Tsao**, J. W. Weber, P. Campbell, P. I. Widenborg, D. Song, and M. A. Green, *Low-temperature growth of polycrystalline Ge thin film on glass by in situ deposition and ex situ solid-phase crystallization for photovoltaic applications*, Applied Surface Science, Vol. 255, pp. 7028-7035, 2009.
- [2] **C.-Y. Tsao**, J. W. Weber, P. Campbell, G. Conibeer, D. Song, and M. A. Green, *In situ low temperature growth of poly-crystalline germanium thin film on glass by RF magnetron sputtering*, Solar Energy Materials & Solar Cells, Vol. 94, pp. 1501-1505, 2010.
- [3] **C.-Y. Tsao**, P. Campbell, D. Song, and M. A. Green, *Influence of hydrogen on structural and optical properties of low temperature polycrystalline Ge films deposited by RF magnetron sputtering*, Journal of Crystal Growth, Vol. 312, pp. 2647-2655, 2010.
- [4] **C.-Y. Tsao**, J. Wong, J. Huang, P. Campbell, D. Song, and M. A. Green, *Structural dependence of electrical properties of Ge films prepared by RF magnetron sputtering*, Applied Physics A, Vol. 102, No. 3, pp. 689-694, 2011.
- [5] **C.-Y. Tsao**, J. Huang, X. Hao, P. Campbell, and M. A. Green, *Heavily boron-doped hydrogenated polycrystalline Ge thin films prepared by co-sputtering*, Electrochemical and Solid-State Letters, Vol. 13, pp. H354-H356, 2010.
- [6] **C.-Y. Tsao**, Z. Liu, X. Hao, and M. A. Green, *In situ growth of Ge-rich poly-SiGe:H thin films on glass by RF magnetron sputtering for photovoltaic applications*, Applied Surface Science, Vol. 257, pp. 4354-4359, 2011.
- [7] **C.-Y. Tsao**, J. Huang, X. Hao, P. Campbell, and M. A. Green, *Formation of heavily boron-doped hydrogenated polycrystalline germanium thin films by co-sputtering for developing  $p^+$  emitters of bottom cells*, Solar Energy Materials

& Solar Cells, Vol. 95, pp. 981-985, 2011.

## B. Papers presented at international conferences

- [8] **C-Y. Tsao**, J. W. Weber, P. Campbell, P. I. Widenborg, S. Varlamov, G. Conibeer, D. Song, and M. A. Green, *In-situ low temperature growth of poly-crystalline germanium thin films on glass by RF-sputtering*, Proceedings of the 18th Photovoltaic Solar Energy Conference, Kolkata, India, 19-21, January, 2009.
- [9] **C-Y. Tsao**, J. Wong, P. Campbell, G. Conibeer, D. Song, and M. A. Green, *Structural and electrical properties of hydrogenated polycrystalline germanium thin films prepared by RF magnetron sputtering for thin film photovoltaics*, in Proceeding of 24th EU PVSEC Conference, Hamburg, Germany, 21-25, September, 2009.
- [10] Y. Tao, S. Varlamov, **C-Y. Tsao**, Z. Ouyang, *Comparative solid-phase crystallisation of Si thin-films on glass deposited by Electron-Beam Evaporation and Plasma-Enhanced CVD*, in Proceeding of 24th EU PVSEC Conference, Hamburg, Germany, 21-25, September, 2009.
- [11] Z. Liu, **C-Y. Tsao**, X. Hao, and M. A. Green, *Influence of hydrogen on properties of germanium-rich poly-SiGe films deposited by RF magnetron sputtering*, in Proceeding of the 48th Annual Conference of the Australian Solar Energy Society (AuSES), Canberra, Australia, 1-3, December, 2010.

## C. Patent application

- [12] **C-Y. Tsao**, X. Hao, and M. A. Green, *A method of forming a germanium layer on a silicon substrate and a photovoltaic device including a germanium layer*, submitted in December, 2010.

---

---

## LIST OF SYMBOLS AND ACRONYMS

---

### A. PHYSICAL PROPERTIES

$\lambda$	Wavelength of light
$\tau_n (\tau_p)$	Effective excess electron (hole) lifetime
$\mu$	Electron mobility
$\sigma$	Electrical conductivity
$\rho$	Resistivity
$\rho_s$	Sheet resistance of the film
$h\nu$	photon energy
$h, \hbar$	Planck constant, $\hbar = h / 2\pi$
$\nu$	Frequency
$\varepsilon_{th}$	biaxial strain of magnitude
$\theta$	The angle satisfying Bragg's law
$\theta_{hkl}$	Angle of incidence onto Miller indices ( $hkl$ ) planes
$\alpha$	Absorption coefficient of film as a function of wavelength
$d_{hkl}$	Interplanar spacing
$A$	The cross-sectional area of diode
$B$	The edge width parameter dependent on structural disorder of films
$D_e(D_h)$	The diffusivity of electron (hole)
$d_{hkl}$	d-space of crystal between Miller indices ( $hkl$ ) planes
$E_g$	Bandgap energy

$f_c(x)$	Collection probability of light-generated minority carrier
$G(x)$	Photogeneration as a function of distance
$g$	Grain size
$I_{hkl}$	Measured X-ray diffraction peak intensity of $(hkl)$ planes for sample
$I_L$	Photogenerated current of a solar cell
$I_{Ohkl}$	Measured X-ray diffraction peak intensity of $(hkl)$ planes for standard powder sample
$IR, NIR$	Infrared, near infrared
$I_S$	Saturation current of a $p-n$ junction solar cell
$k$	Boltzmann's constant/ extinction coefficient
$N_C$	The effective density of states in conduction band
$N_V$	The effective density of states in valence band
$n$	Refractive index
$O_{hkl}$	Orientation factor
$q$	Electron charge
$R$	Resistance/Optical reflection
$T$	Absolute temperature/Optical transmission
$T_m$	The melting point in degree K of material
$t$	thickness of film
$TO$	transverse optical
$V_{oc}$	Open-circuit voltage of a solar cell
$UV-VIS$	Ultraviolet Visible

## **B. MEASUREMENT AND MODELLING TECHNIQUES**

$AFM$	Atomic force microscopy
$EBSD$	Electron backscattered diffraction
$EMA$	Separate effective medium approximation

---

<i>FWHM</i>	Full width at half maximum
<i>HRTEM</i>	High-resolution transmission electron microscopy
<i>SE</i>	Spectroscopic ellipsometry
<i>SEM</i>	Scanning electron microscopy
<i>SIMS</i>	Secondary ion mass spectroscopy
<i>SZM</i>	Structure-zone model
<i>TEM</i>	Transmission electron microscopy
<i>UATR</i>	Universal attenuated total reflection
<i>XPS</i>	X-ray photoelectron spectroscopy
<i>XRD</i>	X-ray diffraction
<i>XTEM</i>	Cross-sectional transmission electron microscopy

### **C. MATERIALS AND DEVICES**

<i>μc-Ge</i>	Microcrystalline germanium
<i>Ar</i>	Argon
<i>a-Ge</i>	Amorphous germanium
<i>B</i>	Boron
<i>c-Ge</i>	Single crystalline germanium
<i>CIGS</i>	Copper-indium-gallium-diselenide
<i>CMOS</i>	Complementary-metal-oxide semiconductor
<i>CSG</i>	Crystalline silicon on glass
<i>FZ-Si</i>	Single crystal silicon grown by the float-zone technique
<i>GeO<sub>2</sub></i>	germanium oxide
<i>HF</i>	Hydrofluoric acid
<i>nc-Ge</i>	Nanocrystalline germanium
<i>MOSFET</i>	metal-oxide-semiconductor field effect transistors

---

<i>P</i>	Phosphorus
<i>poly-Ge</i>	Polycrystalline germanium
<i>poly-Ge:H</i>	Hydrogenated polycrystalline germanium
<i>SiGe</i>	SiGe alloy
<i>SiGe:H</i>	Hydrogenated SiGe alloy
<i>μc-Ge</i>	Microcrystalline germanium

#### **D. PROCESS TECHNIQUES AND PARAMETERS**

<i>CMP</i>	Chemical mechanical polishing
<i>CVD</i>	Chemical-vapour deposition
<i>FTD</i>	Furnace thermal diffusion
<i>LEPECVD</i>	Low-energy plasma-enhanced chemical vapor deposition
<i>MBE</i>	Molecular beam epitaxy
<i>MOCVD</i>	Metal-organic chemical vapour deposition
<i>PECVD</i>	Plasma-enhanced chemical vapor deposition
<i>PVD</i>	Physical vapor deposition
<i>P<sub>B</sub></i>	Level of RF power applied to boron target
<i>RCA</i>	Silicon cleaning sequence developed by Radio Corporation of America (RCA), USA
<i>RF</i>	Radio frequency
<i>RT</i>	Room temperature
<i>RTA</i>	Rapid thermal anneal
<i>SOD</i>	Spin-on-dopant
<i>SPC</i>	Solid-phase crystallization
<i>T<sub>s</sub></i>	Substrate temperature
<i>T<sub>spc</sub></i>	Temperature of solid-phase crystallization

---

<i>UHV</i>	Ultrahigh vacuum
<i>UHV-CVD</i>	Ultrahigh vacuum chemical vapor deposition

**E. OTHERS**

<i>2D</i>	Two-dimensional
<i>3D</i>	Three-dimensional
<i>DC</i>	Direct current
<i>DI</i>	Deionised
<i>DarkStar</i>	A name of a solar cell <i>I-V</i> tester at UNSW
<i>PV</i>	Photovoltaic(s)
<i>RMS</i>	Root mean square
<i>UNSW</i>	University of New South Wales

---

---

## References

---

- Aberle, A. G. (2006a) Fabrication and characterisation of crystalline silicon thin-film materials for solar cells, *Thin Solid Films*, **511-512**, 26-34.
- Aberle, A. G. (2006b) Progress with polycrystalline silicon thin-film solar cells on glass at UNSW, *J. Cryst. Growth*, **267(2)**, 386-390.
- Aberle, A. G., and Inns, D. (2004) Sheet resistance profiling and p-n junction localisation in poly-Si thin-film solar cells by wet-chemical etching, In: *Technical Digest. 14th International Photovoltaic Science and Engineering Conference*, Bangkok Thailand, 26-30 January 2004, pp.747-748.
- Ahrenkiel, R. K., Ahrenkiel, S. P., and Al-Jassim, M. M. (1997) Electronic and mechanical properties of Ge films grown on glass substrates, in: *Conf. Record of the 26th IEEE Photovoltaic Specialists Conference*. Anaheim, CA, USA, 30 September-3 October, pp. 527-529.
- Akbar, S., Chu, J. O., and Cunningham, B. (1993) Heteroepitaxial growth of germanium on silicon by UHV/CVD, US Patent 5,259,918.
- Aleksandrov, L. N., Lovyagin, R. N., Pchelyakov, O. P., and Stenin, S. I. (1974) Heteroepitaxy of germanium thin films on silicon by ion sputtering, *J. Cryst. Growth*, **24-25**, 298-301.
- Amutha, R., Subbarayan, A., and Sathyamoorthy, R. (2006) Influence of substrate temperature on microcrystalline structure and optical properties of ZnTe thin films, *Cryst. Res. Technol.*, **41(12)**, 1174-1179.
- Aspnes, D. E., and Studna, A. A. (1983) Dielectric functions and optical parameters of Si, Ge, GaP, GaAs, GaSb, InP, InAs, and InSb from 1.5 to 6.0 eV, *Phys. Rev. B*, **27(2)**, 985-1009.

- Bajor, G., Cadien, K. C., Ray, M. A., and Greene, J. E. (1982) Growth of high quality epitaxial Ge films on (100) Si by sputter deposition, *Appl. Phys. Lett.*, **40**(8), 696-698.
- Banerjee, A. N., and Chattopadhyay, K. K. (2005) Size-dependent optical properties of sputter-deposited nanocrystalline p-type transparent CuAlO<sub>2</sub> thin films, *J. Appl. Phys.*, **97**, 084308/1-8.
- Banerjee, P. K., Pereira, J. M. T., Hanidu, G. A., and Mitra, S. S. (1988) Doping of RF-sputtered a-SiGe:H alloys, *J. Non-Cryst. Solids*, **104**, 190-194.
- Beensh-Marchwicka, G. M., Mielcarek, W., and Prociow, E. (2001) Evaluation of pulse magnetron sputtered Ge films doped with antimony for sensors application, *Sens. Actuators B*, **76**, 361-365.
- Bidwell, L. R. (1970) The boron-germanium system, *J. of the Less-Common Met.*, **20**, 19-27.
- Bowden, S. (1995) DarkStar - A solar cell data acquisition and characterisation station-User manual, Centre for Photovoltaic Engineering, University of NSW, Sydney Australia.
- Brasen, D., Fitzgerald, E. A., Green, M. L., and Xie, Y.-H. (1993) Method for making low defect density semiconductor heterostructure and devices made thereby, US Patent 5,221,413.
- Cannon, D. D., Liu, J., Danielson, D. T., Jongthammanurak, S., Enuha, U. U., Wada, K., Michel, J., and Kimerling, L. C. (2007) Germanium-rich silicon-germanium films epitaxially grown by ultrahigh vacuum chemical-vapor deposition directly on silicon substrates, *Appl. Phys. Lett.*, **91**, 252111-252113.
- Chambouleyron, I. (1993) Hydrogenated amorphous germanium and its alloys, *J. Phys.: Condens. Matter*, **5**, A73-A80.
- Chambouleyron, I., Fajardo, F., and Zanatta, A. R. (2001) Aluminium-induced crystallization of hydrogenated amorphous germanium thin films, *Appl. Phys. Lett.*, **79**(20), 3233-3235.
- Chambouleyron, I., and Zanatta, A. R. (1998) Nitrogen in germanium, *J. Appl. Phys.*, **84**(1), 1-30.

- Chang, E. Y., Luo, G., Yang, H., and Chang, C. Y. (2007) Growth of GaAs epitaxial layers on Si substrate by using a novel GeSi buffer layer, US Patent 7,259,084 B2.
- Choi, W. K., Teh, L. K., Bera, L. K., and Chim, W. K. (2002) Microstructural characterization of rf sputtered polycrystalline silicon germanium films, *J. Appl. Phys.*, **91**(1), 444-450.
- Chopra, K. L., and Bahi, S. K. (1970) Structural, electrical, and optical properties of amorphous germanium films, *Phys. Rev. B*, **1**(6), 2545-2556.
- Chopra, K. L., and Randhawa, H. S. (1977) The Kinetics of transformation in amorphous germanium alloy films, *Thin Solid Films*, **47**, 203-210.
- Chroneos, A. (2009) Effect of germanium substrate loss and nitrogen on dopant diffusion in germanium, *J. Appl. Phys.*, **105**, 056101/1-3.
- Chui, C. O., Gopalakrishnan, K., Griffin, P. B., Plummer, J. D., and Saraswat, K. C. (2003) Activation and diffusion studies of ion-implanted p and n dopants in germanium, *Appl. Phys. Lett.*, **83**(16), 3275-3277.
- Claeys, C., and Simoen, E. (2007) Germanium-based technologies: from materials to devices, ed. Elsevier, Amsterdam, Boston, Heidelberg, London, New York, Oxford, Paris, San Diego, San Francisco, Singapore, Sydney, Tokyo.
- Clark, A. H. (1967) Electrical and optical properties of amorphous germanium, *Phys. Rev.*, **154**(3), 750-757.
- Comedi, D., F. Dondeo, I. Chambouleyron, Peng, Z. L., and Mascher, P. (2000) Compact hydrogenated amorphous germanium films by ion-beam sputtering deposition, *J. Non-Cryst. Solids*, **266-269**, 713-716.
- Copel, M., Reuter, M. C., Kaxiras, E., and Tromp, R. M. (1989) Surfactants in epitaxial growth, *Phys. Rev. Lett.*, **63**(6), 632-635.
- Copel, M., and Tromp, R. M. (1991) Are bare surfaces detrimental in epitaxial-growth?, *Appl. Phys. Lett.*, **58**(23), 2648-2650.
- Currie, M. T., Samavedam, S. B., Langdo, T. A., Leitz, C. W., and Fitzgerald, E. A. (1998) Controlling threading dislocation densities in Ge on Si using graded SiGe

- layers and chemical-mechanical polishing, *Appl. Phys. Lett.*, **72(14)**, 1718-1720.
- Dalba, G., Fornasini, P., Grisenti, R., Rocca, F., Chambouleyron, I., and Graeff, C. F. O. (1997) Local order in hydrogenated amorphous germanium thin films studied by extended x-ray absorption fine-structure spectroscopy, *J. Phys.: Condens. Matter*, **9**, 5875-5888.
- Demichelis, F., Kaniadakis, G., Tagliaferro, A., and Tresso, E. (1987) New approach to optical analysis of absorbing thin solid films, *Appl. Opt.*, **26(9)**, 1737-1740.
- Despotou, E., Gammal, A. E., Fontaine, B., Montoro, D. F., Latour, M., Lenoir, S., Masson, G., Philbin, P., and Buggenhout, P. V. (May 2010) Global market outlook for photovoltaics until 2014, European Photovoltaic Industry Association, [http://www.epia.org/fileadmin/EPIA\\_docs/public/Global\\_Market\\_Outlook\\_for\\_Photovoltaics\\_until\\_2014.pdf](http://www.epia.org/fileadmin/EPIA_docs/public/Global_Market_Outlook_for_Photovoltaics_until_2014.pdf), [accessed on 10 December 2010].
- Donovan, T. M., Ashely, E. J., and Bennett, H. E. (1963) Effect of Surface Damage on the Reflectance of Germanium, *J. Opt. Soc. Am.*, **53(12)**, 1403-1409.
- Drevillon, B., and Godet, C. (1988) In situ investigation of the microcrystalline germanium nucleation and growth processes, *J. Appl. Phys.*, **64(1)**, 145-151.
- Drusedau, T., and B, S. (1994). Optimization of process parameters for the deposition of improved a-Ge:H by dc magnetron sputtering, *J. Appl. Phys.*, **75 (6)**, 2864-2874.
- Duffy, M. T., Corboy, J. F., Cullen, G. W., Smith, R. T., and Soltis, R. A. (1982). Measurement of the near-surface crystallinity of silicon on sapphire by UV reflectance, *J. Cryst. Growth*, **58**, 10-18.
- E. A. Stern, C. E. B., B. von Roedern and J. Azoulay. (1983) Incipient amorphous-to-crystalline transition in Ge, *Phys. Rev. B*, **27**, 6557 - 6560.
- Eaglesham, D. J., and Cerullo, M. (1990) Dislocation-free Stranski-Krastanow growth of Ge on Si(100), *Phys. Rev. Lett.*, **64(16)**, 1943-1946.
- Evangelisti, F., Garozzo, M., and Conte, G. (1982) Structure of vapor-deposited Ge films as a function of substrate temperature, *J. Appl. Phys.*, **53(11)**, 7390-7396.

- Fitzgerald, E. A. (2000) Controlling threading dislocation densities in Ge on Si using graded GeSi layers and planarization, US Patent 6,107,653.
- Fortner, J., Yu, R. Q., and Lannin, J. S. (1990) Near-surface Raman scattering in germanium clusters and ultrathin amorphous films, *Phys. Rev. B*, **42**, 7610.
- Freeman, E. C., and Paul, W. (1979) Optical constants of rf sputtered hydrogenated amorphous Si, *Phys. Rev. B*, **20**(2), 716-728.
- Gerbi, J. E., and Abelson, J. R. (2007) Low temperature magnetron sputter deposition of polycrystalline silicon thin films using high flux ion bombardment *J. Appl. Phys.*, **101**, 063508-063512.
- Gerbi, J. E., Voyles, P. M., Treacy, M. M. J., Gibson, J. M., and Abelson, J. R. (2003) Increasing medium-range order in amorphous silicon with low-energy ion bombardment, *Appl. Phys. Lett.*, **82**(21), 3665-3667.
- Giangregorio, M. M., Losurdo, M., Ambrico, M., Capezzuto, P., Brunob, G., and Tapfer, L. (2006) Dielectric function and electric properties of germanium thin films prepared by gold mediated crystallization, *J. Appl. Phys.*, **99**, 063511.
- Godet, C., and Cabarrocas, P. R. i. (1992) Hydrogen profiling by elastic recoil detection in microcrystalline germanium thin films, *J. Vac. Sci. Technol. A*, **10**(6), 3517-3521.
- Gombert, A., Glaubitt, W., Rose, K., Dreibholz, J., Bläsi, B., Heinzl, A., Sporn, D., Döll, W., and Wittwer, V. (1999) Subwavelength-structured antireflective surfaces on glass, *Thin Solid Films*, **351**, 73-78.
- Goshima, K., Toyoda, H., Kojima, T., Nishitani, M., Kitagawa, M., Yamazoe, H., and Sugai, H. (1999) Lower temperature deposition of polycrystalline silicon films from a modified inductively coupled silane plasma, *Jpn. J. Appl. Phys.*, **38**(6A), 3655-3659.
- Graeff, C. F. O., and Chambouleyron, I. (1994) Structural and optoelectronic properties of Ge-rich hydrogenated amorphous silicon-germanium alloys, *J. Appl. Phys.*, **76**(4), 2473-2478.
- Grant, P. M., and Paul, W. (1966) Optical Properties of Thin Germanium Films in the Wavelength Range 2000-6000 Å, *J. Appl. Phys.*, **37**(8), 3110-3120.

- Green, M. A. (1982). *Solar Cells: Operating Principles, Technology and System Applications*, Prentice-Hall, Englewood Cliffs, NJ.
- Greene, J. E., and Eltoukhy, A. H. (1981) Semiconductor crystal growth by sputter deposition, *Surf. Interface Anal.*, **3(1)**, 34-54.
- Griguceviciene, A., Leinartas, K., Juskenas, R., and Juzeliunas, E. (2004) Voltammetric and structural characterization of sputter deposited Al–Mg films, *J. Electroanal. Chem.*, **565**, 203-209.
- Haller, E. E. (2006) Germanium: from its discovery to SiGe devices, *Mater. Sci. Semicond. Process.*, **9**, 408-422.
- Harbeke, G., and Jostrzebski, L. (1990) Assessment of the surface quality of SIMOX wafers by UV Reflectance, *J. Electrochem. Soc.*, **137(2)**, 696-699.
- Hasegawa, S., Watanabe, S., T Inokuma, and Kurata, Y. (1995) Structure and grain boundary defects of recrystallized silicon films prepared from amorphous silicon deposited using disilane, *J. Appl. Phys.*, **77(5)**, 1938-1947.
- Heide, J. v., Posthuma, N. E., Flamand, G., Geens, W., and Poortmans, J. (2009). Cost-efficient thermophotovoltaic cells based on germanium substrates, *Sol. Energy Mater. Solar Cells*, **93**, 1810-1816.
- Higuchi, S., and Nakanishi, Y. (1991) The growth of Ge on a Te/Si(100) surface-surface catalytic epitaxy, *Surface Science*, **254(1-3)**, L465-L468.
- Hilfiker, J. N. (2009) Spectroscopic ellipsometry measurements of amorphous, nanocrystalline, microcrystalline, and polycrystalline germanium thin films, *J. A. Woollam Co., Inc.*
- Horn, K. M., Tsao, J. Y., Chason, E., Brice, D. K., and Picraux, S. T. (1991) Hydrogen ion beam smoothing of Ge(001), *J. Appl. Phys.*, **69(1)**, 243-249.
- Hoshi, D., Nakamura, I., and Isomura, M Poly-crystalline Ge thin films prepared by RF sputtering method for thermo photo voltaic application, *Mater. Res. Soc. Symp. Proc.* **862**, 207-212.
- Hutin, L., Koffel, S. p., Royer, C. L., Clavelier, L., Pascal Scheiblin, Mazzocchi, V., and Deleonibus, S. (2008) Activation level in boron-doped thin

- germanium-on-insulator (GeOI): Extraction method and impact of mobility, *Mater. Sci. Semicond. Process.*, **11**, 267-270.
- Inoue, N., and Yasuoka, Y. (1988a) An antenna-coupled warm carrier device using polycrystalline Ge films, *Jpn. J. Appl. Phys.*, **27(8)**, 1437-1439.
- Inoue, N., and Yasuoka, Y. (1988b) Comparison of the properties of Ge thin films grown by plasma-assisted deposition with conventional vacuum evaporation, *Appl. Surf. Sci.*, **33**, 632-639.
- Ioannou, N., Skarlatos, D., Tsamis, C., Krontira, C. A., Georga, S. N., Christofi, A., and McPail, D. S. (2008) Germanium substrate loss during low temperature annealing and its influence on  $\text{P}^{3-}$ -ion-implanted phosphorous dose loss, *Appl. Phys. Lett.*, **93**, 101910/1-3.
- Jelenkovic, E. V., Tonga, K. Y., Cheung, W. Y., Wilson, I. H., Wong, S. P., and Poon, M. C. (2000) Low temperature doping of poly-SiGe films with boron by co-sputtering, *Thin Solid Films*, **368**, 55-60.
- Jelenkovic, E. V., Tong, K. Y., Sun, Z., Mak, C. L., and Cheung, W. Y. (1997) Properties of crystallized  $\text{Si}_{1-x}\text{Ge}_x$  thin films deposited by sputtering, *J. Vac. Sci. Technol. A*, **15(6)**, 2836-2841.
- Jishiashvili, D., Shiolashvili, Z., Gobronidze, V., and Nakhutsrishvili, I. (2002) A study of solid phase reactions at the Ge- $\text{GeO}_2$  interface, in: *Proceedings of 8th International Symposium on Advanced Packaging Materials*, Stone Mountain, GA, USA 3-6 March 2002, 112 - 115.
- Johnson, R. S., Niimi, H., and Lucovsky, G. (2000) New approach for the fabrication of device-quality GeO/ $\text{GeO}_2$ / $\text{SiO}_2$  interfaces using low temperature remote plasma processing, *J. Vac. Sci. Technol. A*, **18(4)**, 1230-1233.
- Joubert, P., Loisel, B., Chouan, Y., and Haji, L. (1987) The effect of low pressure on the structure of LPCVD polycrystalline silicon films, *J. Electrochem. Soc.*, **134(10)**, 2541-2544.
- J. Tauc, Grigorovici, R., and Vancu, A. (1966) Optical properties and electronic Structure of amorphous germanium, *Phys. Stat. Sol.*, **15**, 627-637.

- Jun, S.-I., Racka, P. D., McKnight, T. E., Melechko, A. V., and Simpson, M. L. (2006) Low-temperature solid-phase crystallization of amorphous silicon thin films deposited by rf magnetron sputtering with substrate bias, *Appl. Phys. Lett.*, **89**, 022104-1-3.
- Jun, S.-I., Rack, P., McKnight, T. E., Melechko, A. V., and Simpson, M. L. (2005). Direct-current substrate bias effects on amorphous silicon sputter-deposited films for thin film transistor fabrication, *Appl. Phys. Lett.*, **87**, 132108/1-3.
- K. Teh, L., Choi, W. K., Bera, L. K., and Chim, W. K. (2001) Structural characterisation of polycrystalline SiGe thin film, *Solid-State Electron*, **45**, 1963-1966.
- Kaenel, H. V. (2007) Method for producing virtual Ge substrates for III/V-integration on Si (001), US Patent 2007/0231488 A1.
- Kahng, S.-J., Ha, Y. H., Park, J.-Y., Kim, S., Moon, D. W., and Kuk, Y. (1998). Hydrogen-surfactant mediated growth of Ge on Si(001), *Phys. Rev. Lett.*, **80(22)**, 4931-4934.
- Keevers, M. J., Turner, A., Schubert, U., Basore, P. A., and M. A. Green Remarkably effective hydrogenation of crystalline silicon on glass modules, in: *Proceedings 20th European Photovoltaic Solar Energy Conference*, Barcelona, Spain, 6–10 June 2005, pp.1305–1308.
- Kelly, P. J., and Arnell, R. D. (2000) Magnetron sputtering: a review of recent developments and applications, *Vacuum*, **56**, 159-172.
- King, R. R., Law, D. C., Edmondson, K. M., Fetzer, C. M., Kinsey, G. S., Yoon, H., Sherif, R. A., and Karam, N. H. (2007) 40% efficient metamorphic GaInP/GaInAs/Ge multijunction solar cells, *Appl. Phys. Lett.*, **90**, 183516.
- King, T.-J., and Saraswat, K. C. (1994) Deposition and properties of low-pressure chemical-vapor deposited polycrystalline silicon-germanium films, *J. Electrochem. Soc.*, **141(8)**, 2235-2241.
- Kobayashi, H., Inoue, N., Uchida, T., and Yasuoka, Y. (1997) Electrical properties of evaporated polycrystalline Ge thin-films, *Thin Solid Films*, **300**, 138-143.

- Koike, M., Kamata, Y., Ino, T., Hagishima, D., Tatsumura, K., Koyama, M., and Nishiyama, A. (2008) Diffusion and activation of n-type dopants in germanium, *J. Appl. Phys.*, **104**(2), 023523/1-5.
- Koschier, L. M., Wenham, S. R., and Green, M. A. (1999) Modeling and Optimization of Thin-Film Devices with Si<sub>1-x</sub>Ge<sub>x</sub> Alloys, *IEEE Trans. Electron Devices*, **46**(10), 2111-2115.
- Kumru, M. (1991) A comparison of the optical, IR, electron spin resonance and conductivity properties of a-Ge<sub>1-x</sub>C<sub>x</sub>:H with a-Ge:H and a-Ge thin films prepared by R.F. sputtering, *Thin Solid Films*, **198**, 75-84.
- Kuo, C.-C. (2008) Characterization of polycrystalline Ge thin films fabricated by short-pulse XeF excimer laser crystallization, *J. Russ. Laser Res.*, **29**(2), 167-175.
- Li, J. H., Springholz, G., Stangl, J., Seyringer, H., Holy, V., Schäffler, F., and Bauer, G. (1998) Strain relaxation and surface morphology of compositionally graded Si/Si<sub>1-x</sub>Ge<sub>x</sub> buffers, *J. Vac. Sci. Technol. B*, **16**(3), 1610-1615.
- Lin, H.-C., Chang, H.-Y., Jung, T.-G., Wang, P. J., Deng, R.-C., and Lin, J. (1994) Effect of boron doping on the structural properties of polycrystalline silicon films grown at reduced pressures, *J. Appl. Phys.*, **76**(3), 1572-1577.
- Isai, M., Beerens, J., and N.Cheekea, J. D. (1991) Inversion of conduction type in thin InSb films prepared on glass substrates, *J. Appl. Phys.*, **69**(10), 7130-7133.
- Luan, H.-C., and Kimerling, L. C. (2003) Cyclic thermal anneal for dislocation reduction, US Patent 6,635,110 B1.
- Luan, H.-C., Lim, D. R., Lee, K. K., Chen, K. M., Sandland, J. G., Wada, K., and Kimerling, L. C. (1999) High-quality Ge epilayers on Si with low threading-dislocation densities, *Appl. Phys. Lett.*, **75**(19), 2909-2911.
- Luo, G., Yang, T. H., Chang, E. Y., Chang, C. Y., and Chao, K. A. (2003) Growth of high-quality Ge epitaxial layers on Si (100), *Jpn. J. Appl. Phys.*, **42**(2), L517-L519.

- Makino, T., and Nakamura, H. (1981) Resistivity changes of heavily-boron-doped CVD-prepared polycrystalline silicon caused by thermal annealing, *Solid-State Electron.*, **24**, 49-55.
- Maruyama, E., Haku, H., Tanaka, M., Kiyama, S., and Tsuda, S. (1997) Preparation of Poly-Ge Considering its Application to a-Si/Poly-Ge Multilayer Structure by a Low-Temperature Solid Phase Crystallization Method, *Jpn. J. Appl. Phys.*, **36**, 262-266.
- Matsui, T., Muhida, R., Kawamura, T., and Toyama, T. (2002) Microstructural dependence of electron and hole transport in low-temperature-grown polycrystalline-silicon thin-film solar cells, *Appl. Phys. Lett.*, **81(25)**, 4751-4753.
- Mauk, M. G., Balliet, J. R., and Feyock, B. W. (2003) Large-grain (>1-mm),recrystallized germanium films on alumina,fused silica,oxide-coat ed silicon substrates for III–V solar cell applications, *J. Cryst. Growth*, **250**, 50-56.
- Meng, Z., Jin, Z., Gururaj, B. A., Chu, P., Kwok, H. S., and Wong, M. (1997). Germanium thin film formation by low-pressure chemical vapor deposition, *J. Electrochem. Soc.*, **144(4)**, 1423-1429.
- Mittemeijer, E. J., and Scardi, P. (2004) *Diffraction Analysis of the Microstructure of Materials*, ed., Springer-Verlag, Berlin Heidelberg New York.
- Mittemeijer, E. J., and Welzel, U. (2008) The “state of the art” of the diffraction analysis of crystallite size and lattice strain, *Zeitschrift fur Kristallographie*, **223(9)**, 552-560.
- Movchan, B. A., and Demchishin, A. V. (1969) Study of the structure and properties of thick vacuum condensates of nickel, titanium, tungsten, alluminium oxide and zirconium dioxide, *Phys. Metals Metallogr.*, **28(4)**, 83-90.
- Mulato, M., Chambouleyron, I., and Torriani, I. L. (1996) Hydrogen bonding and void microstructure of a-Ge:H films, *J. Appl. Phys.*, **79(8)**, 4453-4455.

- Mulato, M., Toet, D., Aichmayr, G., Santos, P. V., and Chambouleyron, I. (1997) Laser crystallization and structuring of amorphous germanium, *Appl. Phys. Lett.*, **70(26)**, 3570-3572.
- Myers, A. M., Doyle, J. R., Feng, G. J., Maley, N., RUZIC, D. L., and ABELSON, J. R. (1991) Energetic particle fluxes in magnetron sputter deposition of a-Si:H, *J. Non-Cryst. Solids*, **137-138**, 783-786.
- Nagashima, T., Okumura, K., Muratal, K., and Yamaguchi, M. (2003) A germanium back-contact type cell for thermophotovoltaic applications, in: *Proceedings of 3rd World Conference on Photovoltaic Energy Conversion*, Osaka, Japan, 11 – 18 May 2003, pp.200-203.
- Nakamura, I., Ajiki, T., Abe, H., Hoshi, D., and Isomura, M. (2006) Formation of polycrystalline SiGe thin films by the RF magnetron sputtering method with Ar-H<sub>2</sub> mixture gases, *Vacuum*, **80**, 712-715.
- Narita, T., Naruse, K., Suzuki, I., Ogawa, S., Iida, T., Yoshida, N., Itoh, T., and Nonomura, S. (2008) Deposition of microcrystalline Ge films using hot-wire technique without toxic gases, *J. Non-Cryst. Solids*, **354**, 2214-2217.
- Okamoto, Y., Makihara, K., Higashi, S., and Miyazaki, S. (2005) Formation of microcrystalline germanium ( $\mu\text{c-Ge:H}$ ) films from inductively coupled plasma CVD, *Appl. Surf. Sci.*, **244**, 12-15.
- Olivares, J., Martin, P., Rodriguez, A., Sangrador, J., Jimenez, J., and Rodriguez, T. (2000) Raman spectroscopy study of amorphous SiGe films deposited by low pressure chemical vapor deposition and polycrystalline SiGe films obtained by solid-phase crystallization, *Thin Solid Films*, **358**, 56-61.
- Ouyang, L. H., Rode, D. L., Zulkifli, T., Abraham-Shrauner, B., Lewis, N., and Freeman, M. R. (2002) Hydrogenated amorphous and microcrystalline GaAs films prepared by radio-frequency magnetron sputtering, *J. Appl. Phys.*, **91(5)**, 3459-3467.
- Paul, W., Levis, A. J., Connell, C. A. N., and Moustakas, T. D. (1976) Doping, Schottky barrier and p-n junction formation in amorphous germanium and silicon by rf sputtering, *Solid State Comm.*, **20**, 969-972.

- Peng, Z. L., Comedi, D., Dondeo, F., Chambouleyron, I., Simpson, P. J., and Mascher, P. (1999) Investigation of ion-bombardment effects on the formation of voids during deposition of a-Ge : H, *Physica B*, **273-274**, 579-583.
- Petrov, I., Barna, P. B., Hultman, L., and Greene, J. E. (2003) Microstructural evolution during film growth, *J. Vac. Sci. Technol. A*, **21(5)**, S117-S128.
- Pietralunga, S. M., Fere, M., Lanata, M., Piccinin, D., Radnoczi, G., Misjak, F., Lamperti, A., Martinelli, M., and M.Ossi, P. (2009) Heteroepitaxial sputtered Ge on Si (100): Nanostructure and interface morphology, *A Letters Journal Exploring The Frontiers of Physics*, **88**, 28005/1-6.
- Pilione, L. J., Vedam, K., Yehoda, J. E., and Messier, R. (1987) Thickness dependence of optical gap and void fraction for sputtered amorphous germanium, *Phys. Rev. B*, **35(17)**, 9368-9371.
- Platz, R., and Wagner, S. (1998) Intrinsic microcrystalline silicon by plasma-enhanced chemical vapor deposition from dichlorosilane, *Appl. Phys. Lett.*, **73**, 1236-1238.
- Posthuma, N. E., Heide, J. v. d., Flamand, G., and Poortmans, J. (2007) Emitter formation and control realization by diffusion for germanium photovoltaic devices, *IEEE Trans. Electron Devices*, **54(5)**, 1210-1215.
- Poulsen, P. R., Wang, M., Xu, J., Li, W., Chen, K., Wang, G., and Feng, D. (1998) Role of hydrogen surface coverage during anodic plasma deposition of hydrogenated nanocrystalline germanium, *J. Appl. Phys.*, **84(6)**, 3386-3391.
- R. W. Collins, H. W., J. M. Cavese and J. Gonzalez-Hernandez. (1985) Optical properties of dense thin-film Si and Ge prepared by ion-beam sputtering, *J. Appl. Phys.*, **58**, 954-957.
- Rath, J. K. (2003) Low temperature polycrystalline silicon: a review on deposition, physical properties and solar cell applications, *Sol. Energy Mater. Solar Cells*, **76**, 431-487.
- Rudder, R. A., Cook, J. W., Jr, and Lucovsky, G. (1983) High photoconductivity in magnetron sputtered amorphous hydrogenated germanium films, *Appl. Phys. Lett.*, **43(9)**, 871-873.

- Saito, N., Nakaaki, I., Yamaguchi, T., Yoshioka, S., and Nakamura, S. (1995) Influence of deposition conditions on the properties of a-GeC:H and a-Ge:H films prepared by r.f. magnetron sputtering, *Thin Solid Films*, **269**, 69-74.
- Sakai, A., and Tatsumi, T. (1994) Ge growth on Si using atomic hydrogen as a surfactant, *Appl. Phys. Lett.*, **64(1)**, 52-54.
- Sakamoto, K., Kyoya, K., Miki, K., Matsuhata, H., and Sakamoto, T. (1993) Which surfactant shall we choose for the heteroepitaxy of Ge/Si(001) questionable – Bi as a surfactant with small self-incorporation, *Jpn. J. Appl. Phys.*, **32(2A)**, L204-L206.
- Sakamoto, N., Hirakawa, K., and Ikoma, T. (1995) Conduction-type conversion in Si-doped (311) A GaAs grown by molecular beam epitaxy, *Appl. Phys. Lett.*, **67(10)**, 1444-1446.
- Satta, A., Simoen, E., Clarysse, T., Janssens, T., Benedetti, A., B. De Jaeger, Meuris, M., and Vandervorst, W. (2005a). Diffusion, activation, and recrystallization of boron implanted in preamorphized and crystalline germanium, *Appl. Phys. Lett.*, **87**, 172109/1-3.
- Satta, A., Simoen, E., Duffy, R., Janssens, T., Clarysse, T., Benedetti, A., Meuris, M., and Vandervorst, W. (2005b) Diffusion, activation, and regrowth behavior of high dose P implants in Ge, *Appl. Phys. Lett.*, **88**, 162118/1-3.
- Scheller, L. P., Weizman, M., Nickel, N. H., and Yan, B. (2009) Electrical transport in laser-crystallized polycrystalline silicon-germanium thin-films, *Appl. Phys. Lett.*, **95(6)**, 062101/1-3.
- Schott Inc. (2009) Product Properties, <http://www.us.schott.com/hometech/english/products/borofloat/attribute/thermic/index.html>, [accessed on 24 January 2009].
- Schröder, B., Annen, A., Drüsedau, T., Freistedt, H., Deák, P., and Oechsner, H. (1993) Influence of oxygen incorporation on the properties of magnetron sputtered hydrogenated amorphous germanium films, *Appl. Phys. Lett.*, **62(16)**, 1961-1963.

- Shao, M., Fischer, A., Grecu, D., Jayamaha, U., Bykov, E., Contreras-Puente, G., Bohn, R. G., and Compaan, A. D. (1996) Radio-frequency-magnetron-sputtered CdS/CdTe solar cells on soda-lime glass, *Appl. Phys. Lett.*, **69**(20), 3045-3047.
- Simoen, E., Satta, A., Amore, A. D., Janssens, T., Clarysse, T., K. Martens, Jaeger, B. D., Benedetti, A., Hofliijk, I., Brijs, B., Meuris, M., and Vandervorst, W. (2006). Ion-implantation issues in the formation of shallow junctions in germanium, *Mater. Sci. Semicond. Process.*, **9**, 634-639.
- Simoen, E., and Vanhellefont, J. (2009) On the diffusion and activation of ion-implanted n-type dopants in germanium, *J. Appl. Phys.*, **106**, 103516/1-4.
- Song, D., Cho, E.-C., Cho, Y.-H., Conibeer, G., Huang, Y., Huang, S., and Green, M. A. (2008a) Evolution of Si (and SiC) nanocrystal precipitation in SiC matrix, *Thin Solid Films*, **516**, 3824-3830.
- Song, D., Cho, E.-C., Conibeer, G., Cho, Y.-H., Huang, Y., Haung, S., Flynn, C., and Green, M. A. (2007) Fabrication and characterization of Si nanocrystals in SiC matrix produced by magnetron cosputtering, *J. Vac. Sci. Technol. B*, **25**(4), 1327-1335.
- Song, D., Cho, E.-C., Conibeer, G., Flynn, C., Huang, Y., and Green, M. A. (2008b) Structural, electrical and photovoltaic characterization of Si nanocrystals embedded SiC matrix and Si nanocrystals /c-Si heterojunction devices, *Sol. Energy Mater. Solar Cells*, **92**, 474-481.
- Song, D., Inns, D., Straub, A., Terry, M. L., Campbell, P., and Aberle, A. G. (2006) Solid phase crystallized polycrystalline thin-films on glass from evaporated silicon for photovoltaic applications, *Thin Solid Films*, **513**, 356-363.
- Srivastava, G. P., Tripathi, K. N., and Sehgal, N. K. (1986) Effect of laser irradiation on the electrical properties of amorphous germanium films, *J. Mater. Sci.*, **21**, 2972-2976.
- Sundaram, K. B., and Garside, B. K. (1984) Controlled Doping of rf Sputtered Germanium Films, *Appl. Phys. A*, **34**, 117-121.
- Sze, S. M. (1986). *Semiconductor devices: physics and technology* John Wiley & Sons Inc; International Ed edition

- Sze, S. M., and Ng, K. K. (2007) *Physics of Semiconductor Devices*, John Wiley & Sons, New York.
- Taishi, T., Ohno, Y., and Yonenaga, I. (2010) Equilibrium segregation coefficient and solid solubility of B in Czochralski Ge crystal growth, *Thin Solid Films*, **518**, 2409-2412.
- Thompson, C. V. (1998) Grain growth in Polycrystalline thin films of semiconductors, *Interface Sci.*, **6**, 85-93.
- Thompson, C. V. (2000) Structure evolution during processing of polycrystalline films, *Annu. Rev. Mater. Sci.*, **30**, 159-190.
- Thornton, J. A. (1974) Influence of apparatus geometry and deposition conditions on the structure and topography of thick sputtered coatings, *J. Vac. Sci. Technol.*, **11(4)**, 666-670.
- Thornton, J. A. (1986) The microstructure of sputter-deposited coatings, *J. Vac. Sci. Technol. A*, **4(6)**, 3059-3065.
- Tompkins, H. G., and McGahan, W. A. (1999) *Spectroscopic ellipsometry and reflectometry*, John Wiley & Sons, Inc., New York
- Tripathi, S., Brajpuriya, R., Mukharjee, C., and Chaudhari, S. M. (2006) Determination of band gap in polycrystalline Si/Ge thin film multilayers, *J. Mater. Res.*, **21(3)**, 623-631.
- Tsao, C.-Y., Campbell, P., Song, D., and Green, M. A. (2010a) Influence of hydrogen on structural and optical properties of low temperature polycrystalline Ge films deposited by RF magnetron sputtering, *J. Cryst. Growth*, **312**, 2647-2655.
- Tsao, C.-Y., Huang, J., Hao, X., Campbell, P., and Green, M. A. (2010b) Heavily boron-doped hydrogenated polycrystalline Ge thin films prepared by co-sputtering, *Electrochem. Solid-St.*, **13(10)**, H354-H356.
- Tsao, C.-Y., Huang, J., Hao, X., Campbell, P., and Green, M. A. (2011a) Formation of heavily boron-doped hydrogenated polycrystalline germanium thin films by co-sputtering for developing p<sup>+</sup> emitters of bottom cells, *Sol. Energy Mater. Solar Cells*, **95**, 981-985.

- Tsao, C.-Y., Liu, Z., Hao, X., and Green, M. A. (2011b) *In situ* growth of Ge-rich poly-SiGe:H thin films on glass by RF magnetron sputtering for photovoltaic applications, *Appl. Surf. Sci.*, **257**, 4354-4359.
- Tsao, C.-Y., Weber, J. W., Campbell, P., Conibeer, G., Song, D., and Green, M. A. (2010c) In situ low temperature growth of poly-crystalline germanium thin film on glass by RF magnetron sputtering, *Sol. Energy Mater. Solar Cells*, **94**, 1501-1505.
- Tsao, C.-Y., Weber, J. W., Campbell, P., Widenborg, P. I., Song, D., and Green, M. A. (2009) Low-temperature growth of polycrystalline Ge thin film on glass by in situ deposition and ex situ solid-phase crystallization for photovoltaic applications, *Appl. Surf. Sci.*, **255**, 7028-7035.
- Tsao, C.-Y., Wong, J., Huang, J., Campbell, P., Song, D., and Green, M. A. (2011c) Structural dependence of electrical properties of Ge films prepared by RF magnetron sputtering, *Appl. Phys. A*, **102**, 689-694.
- Uppal, S., Willoughby, A. F. W., Bonar, J. M., Cowern, N. E. B., Grasby, T., Morris, R. J. H., and Dowsett, M. G. (2004) Diffusion of boron in germanium at 800–900°C, *J. Appl. Phys.*, **96(3)**, 1376-1380.
- Uppal, S., Willoughby, A. F. W., Bonar, J. M., Evans, A. G. R., Cowern, N. E. B., Morris, R., and Dowsett, M. G. (2001) Diffusion of ion-implanted boron in germanium, *J. Appl. Phys.*, **90(8)**, 4293-4295.
- Wada, K., Kimerling, L. C., Ishikawa, Y., Cannon, D. D., and Liu, J. (2004) Ge photodetectors, US Patent 6,812,495 B2.
- Wakaki, M., Iwase, M., Show, Y., Koyama, K., Sato, S., Nozaki, S., and Morisaki, H. (1996) Raman spectroscopy of germanium films deposited with cluster-beam technique, *Physica B*, **219&220**, 535-537.
- Weber, J., and Alonso, M. I. (1989) Near-band-gap photoluminescence of Si-Ge alloys, *Phys. Rev. B*, **40**, 5683-5693.
- Widenborg, P. I., and Aberle, A. G. (2007) Hydrogen-induced dopant neutralisation in p-type AIC poly-Si seed layers functioning as buried emitters in ALICE thin-film solar cells on glass, *J. Cryst. Growth*, **306**, 177-186.

- Yang, T. H., Luo, G. L., Chang, E. Y., Hsieh, Y. C., and Chang, C. Y. (2004). Interface-blocking mechanism for reduction of threading dislocations in SiGe and Ge epitaxial layers on Si(100) substrates, *J. Vac. Sci. Technol. B*, **22(5)**.
- Yu, P. Y., and Cardona, M. (2003) Fundamentals of Semiconductors, Springer-Verlag Berlin Heidelberg New York.
- Yuji, T., and Sung, Y. M. (2005) Electrical properties of an epitaxial Si film prepared by RF magnetron plasma at low temperature, *Thin Solid Films*, **475**, 348-353.
- Zanzig, L., Beyer, W., and Wagner, H. (1995) High quality hydrogenated amorphous germanium prepared by the hot wire technique, *Appl. Phys. Lett.*, **67(11)**, 1567-1569.
- Zanzucchi, P. J., and Frenchu, W. R. (1981) Optical reflectance: a sensitive nondestructive method for detecting surface damage in crystalline GaAs and other semiconductors, *Appl. Opt.*, **20(4)**, 643-646.